Alma Mater Studiorum – Università di Bologna

DOTTORATO DI RICERCA IN

INGEGNERIA CIVILE, CHIMICA, AMBIENTALE E DEI MATERIALI

Ciclo XXX

Settore Concorsuale: 08/A2

Settore Scientifico Disciplinare: Ingegneria e Sicurezza degli Scavi ING-IND/28

Rock Mass Fracture Detection and Modelling Using GPR for Evaluation and Production Optimization of Ornamental Stone Deposits

Presentata da: Mohamed Elkarmoty

Coordinatore Dottorato

Prof. Luca Vittuari

Supervisore

Prof. Stefano Bonduà

Co-Supervisore

Prof. Roberto Bruno

Esame finale anno 2018

A thesis submitted to

University of Bologna

School of Engineering and Architecture

Department of Civil, Chemical, Environmental and Materials Engineering

In partial fulfillment of the requirements for the award of the degree of

Doctor of Philosophy

Ph.D. Cycle: 30th

Scientific Sector: Excavation Engineering and Safety ING-IND/28

Rock Mass Fracture Detection and Modelling Using GPR for Evaluation and Production Optimization of Ornamental Stone Deposits

Mohamed Elkarmoty

Ph.D. coordinator

Prof. Luca Vittuari

Supervisor

Prof. Stefano Bonduà

Co-supervisor

Prof. Roberto Bruno

May 2018

To my dear parents and the memory of my grandmother.

To Professor Mohamed Elwageeh who suggested to me this Ph.D. research topic in 2014.

Acknowledgments

First and foremost, I would like to express my sincere gratitude to my Ph.D. supervisors, Prof. Stefano Bonduà and Prof. Roberto Bruno, for the continuous support during my Ph.D. study, for their patience, motivation, and immense knowledge.

A special word of thanks goes to the EU-METALIC II—ERASMUS MUNDUS program that funded my Ph.D. scholarship for 34 months. I am grateful to the Italian Ministry of Foreign Affairs and International Cooperation for funding my research for further 6 months to continue and improve the Ph.D. research topic.

Many thanks to IDS GeoRadar s.r.l., the Italian company that supported my research through providing the GPR instrument for several field tests. I should not forget to thank Dr. Paolo Papeschi and Dr. Fabio Giannino (IDS GeoRadar s.r.l.) for their trust, cooperation, and usual availability.

This work would not come out without the cooperation with two Italian quarrying companies: La Borghigiana s.r.l. and Augelli Marmi that allowed performing the GPR tests in their quarries. Special thanks for Mr. Stefano Cangioli (La Borghigiana s.r.l.), Mr. Michele Augelli and Mr. Michele Di Carlo (Augelli Marmi) for their availability, useful information, and generous hospitality.

A thank you to Prof. Giuseppe Raspa (Sapienza Università di Roma) and to Prof. Claudio Margottini (Scientific and Technological Attaché, Embassy of Italy in Egypt) for reading and evaluating my Ph.D. thesis before the final submission. I would like also to thank the professors (Prof. F. Tinti, Prof. D. Boldini, and Prof. V. Bortolotti) and my lovely colleagues (C. Cormio, S. Kasmaeeyazdi, S. Focaccia, F. Peddis, and A. Bandini) of the geo-resources research group at University of Bologna for their support, the fruitful technical discussions, and the nice time we shared together during my Ph.D.

Table of Contents

List of Figures

List of Tables

Abstract

The thesis presents new solutions for the fractures problem in ornamental stone quarries which entails economic and material loses. The thesis aimed at developing methodologies and providing solutions for evaluation and production optimization of ornamental stone deposits. Ground Penetrating Radar (GPR) was selected, among several methods, as a fracture detection tool for this research. A combination of the use of a low frequency GPR antenna and laboratory rock tests for evaluation of an ornamental stone deposit showed encouraging results. Based on GPR survey, particularly high frequency antennas, a 3D deterministic fracture modeling approach was developed and implemented in several case studies of block and bench scales. A fracture index was proposed for deposit evaluation based on fracture detections from GPR survey. Additionally, an in-situ GPR test allowed formulating a propagation velocity model for 3D mapping of the dielectric constant of the medium, within macro and micro scale of the rock mass of a bench in a sandstone quarry. This finding is significant for future improvement of the deterministic accuracy level of the developed fracture modeling approach and, generally, for the GPR applications in rock mass. Regarding quarrying optimization, two 3D algorithms, based on fracture modeling or mapping, were developed for production and/or revenue optimization of cutting slabs from blocks and cutting blocks from benches. The algorithms were coded in two software packages named SlabCutOpt and BlockCutOpt. SlabCutOpt was applied to a case study of a limestone block through testing 37 different commercial-sizes of slabs, investigating the optimization results in terms of recovery ratio (a geo-environmental direction) and revenue (an economic direction). BlockCutOpt was applied to two case studies (quarries) with different site characteristics. The results showed that optimum cutting direction of blocks can vertically and horizontally vary, giving geometric information about the cutting grid of blocks that optimizes the production.

CHAPTER 1

Overview

1.1. Statement of the problem

Natural stones, dimension stones, and ornamental stones are terms referring to stones extracted from quarries and used for construction and decorative functions with marketable shapes of blocks, slabs, and tiles. Carvalho et al., 2008, identified the differences between the uses of these terms and justified why the term "ornamental stone" is the most appropriate denomination for this sector: it signifies not only the commercial purpose but also the end-use of this raw material. Therefore, the author of this Ph.D. thesis preferred using the term ''ornamental stones'' in the whole thesis. Examples of ornamental stones rock type can be: granite, marble, limestone, and sandstone.

Historically, ornamental stones have been used as a kind of documentation for old civilizations. The ancient Egyptians, Greek and Roman empires used ornamental stones in building their long-life monuments and structures which still exist till now. This ensures that ornamental stones are the most life-long material for construction works (Abu Hanieh et al., 2014).

According to (Montani, 2003), only a third of the exploited raw material reaches the global market as a finished product, while the remaining two thirds are waste, considering the worldwide average in the excavation of ornamental stones. Commercially, ornamental stones are considered as main economic resources for many countries overall the world (Montani, 2008). Therefore, and since ornamental stones are natural non-renewable resources, ornamental stones need to be quarried sustainably for environmental and economic reasons.

One of the main reasons for the waste production, in the quarrying industry, lays in the natural rock discontinuities (simply referred as fractures) which occur in different geologic forms, classes and sizes as given in details in (Gillespie et al., 2011). Natural fractures form irregular natural blocks bounded within the fracture surfaces. The size of the extracted blocks is governed by the volume of the natural blocks, or in other words, the spacing of the fracture families. Therefore, fractures status characterization is necessary not only for the waste minimization during quarrying but also for the pre-quarrying evaluation which is a part of the objectives of this thesis.

A leading factor giving a profitable value to the ornamental stones is the block size, since small sizes of the extracted blocks limit the dimensions required for processing the stone pieces, and

consequently a narrow range of applications will be available. The block size is a function of the weight and both of them are important for the safety issues of transporting, handling, and processing of blocks (Mosch et al., 2011). Standard dimensions range of commercial block sizes is between 2.0 m x 1.0 m x 0.5 m and 3.0 m x 2.0 m x 1.0 m (United Nations, 1976); however, slight changes in the commercial dimensions have been noticed in the recent years due to economic reasons and technological advancements. Optimization matters here come up: What is the optimum cutting direction for a certain size of block that optimizes the production? What is the optimum commercial block size that maximizes the production/ revenue and minimizes the waste? In this thesis, answers for these research questions are considered as further objectives.

Fractures and hidden defects cause waste not only within the cutting of blocks from benches of quarries but also within the cutting of slabs and tiles from ornamental stone blocks. Similarly to blocks which are marketable in several commercial sizes, the slabs and tiles are cut with several sizes according to the using purpose. Most commonly, quarrymen follow traditional naked-eye observation to physically evaluate the block and prefer to cut the slabs with the maximum dimensions which have the highest price. Actually, the naked-eye evaluation entails errors since no information about the hidden part of the body can be obtained in this way. Moreover, cutting a large size of slab from blocks may not provide the maximum revenue/ recovery: this is a further optimization research point of this thesis.

To reach the research objectives, the author selected Ground Penetrating Radar (GPR) as a non-destructive fracture detection method for both the quarry and the block scales. A survey on the fracture detection methods and basics of GPR are presented in Chapter 2.

1.2. Structure of the research

The structure of the PhD research was performed mainly through two modules: Module A and Module B (Figure 1). Module A considered fracture detection and modeling using GPR. Module B considered quarrying production optimization. Module A consists of three contributions presented in three chapters whereas Module B contains two contributions presented in two chapters. Each chapter contains its specific technical literature review.

Regarding Module A, it contains (i) Chapter 3: providing a combination of the use of low frequency GPR antenna and laboratory rock tests to evaluate an ornamental stone deposit; (ii) Chapter 4: developing a new three-dimensional deterministic fracture modeling approach,

based on GPR survey, which led to developing an evaluation based fracture index for the surveyed stone body; (iii) Chapter 5: developing an innovative three-dimensional modeling methodology to map the dielectric constant variability in a rock mass which is significant, in particular, for future development of the developed fracture modeling approach and, in general, for the GPR applications in rock masses.

Chapter 4 is the direct link between Module A and Module B. Module B contains: (i) Chapter 6: developing an innovative 3D block scale production optimization algorithm, coded in the C++ programming language, to find the optimum size for cutting slabs from an ornamental stone block; (ii) Chapter 7: developing a new 3D quarry scale production optimization algorithm, coded in C++ programming language, to find the optimum cutting direction of blocks from benches of ornamental stone quarries.

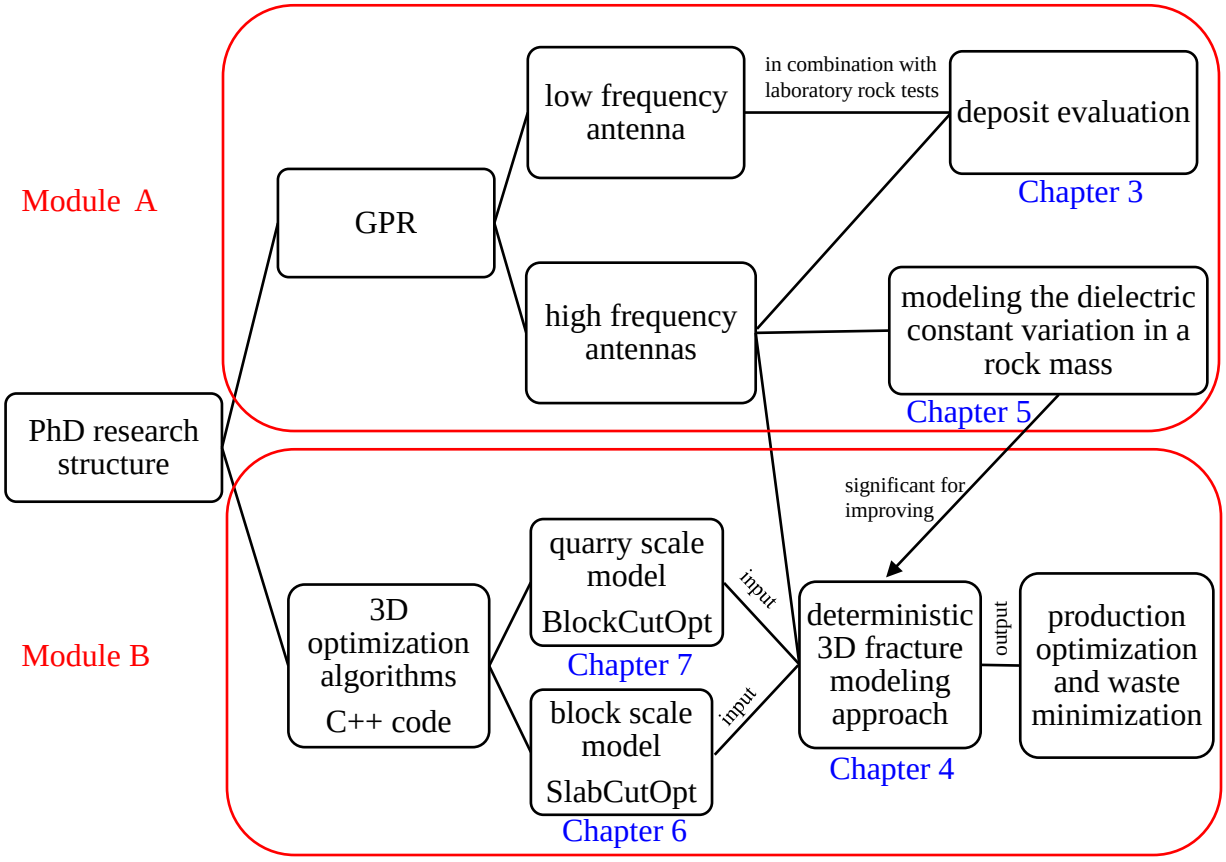

Figure 1: Graphical scheme of the PhD research structure.

CHAPTER 2

Fracture Detection and GPR

2.1. Fracture detection methods

Geo-engineering applications require an accurate characterization of the rock mass discontinuities in order to carry out safe and feasible surface or underground geo-engineering projects. Discontinuities are mostly described as fractures, however there are various definitions for fractures. Some definitions are mechanical whilst others are descriptive. Fractures are used as a collective term representing discontinuities features in rock mass such as joints, faults, bedding planes, and fissures (Martinez-Torres, 2002). The classical characterization of rock mass fractures is based on the observation of outcropping fracture traces in rock faces. The detection of discontinuities spatial intensity (amount and spacing) and the modeling of their geometric features (extension, shape and orientation) of the entire rock mass is a challenging research.

The detection methods of fractures, for different geo-engineering applications, are the topic of a number of publications. They can be mainly classified in destructive and non-destructive methods. With reference to destructive methods, it is worth mentioning methods based on boring the rock mass such as drill core analysis, borehole tele-viewer and well logs (e.g. Annavarapu et al., 2012; Dezayes et al., 2000; Gao et al., 2016; Lau et al., 1987; Zazoun, 2013). These methods are time consuming and expensive. However, they are used as data source for the stochastic modeling of fractures, for huge projects (such as petroleum reservoir characterization) and not when boring the rock mass may be considered a partial deposit destruction (for example, in applications to ornamental stone quarrying production). Non-destructive methods can be divided into contact and non-contact methods. Non-contact non-destructive surveying methods (laser scanning, photogrammetric and optical methods) (e.g. Assali et al., 2014; Deliormanli et al., 2014; Fisher et al., 2014; Lai et al., 2014; Vasuki et al., 2014) have currently wide applications, such as landslides and slope stability analysis, particularly when the surveying area is not accessible and the surveyed rock face is not flat. These methods can survey wide surfaces of rock faces, and often stochastic modeling of fractures is applied to the measured data. Contact geophysical non-destructive methods (Ground Penetrating Radar GPR, seismic tomography and resistivity profiling methods) (e.g. Dérobert and Abraham, 2000; Mineo et al., 2015; Seol et al., 2001; Theune et al., 2006; Walton

et al., 2015; Zajc et al., 2014; Zimmer and Sitar, 2015; Zou and Wu, 2001) are also used in various applications to detect fractures. A traditional method of contact non-destructive methods is the manual survey by compass (e.g. International Society For Rock Mechanics (ISRM), 1978; Priest and Hudson, 1981; Stavropoulou, 2014). It is used to characterize out-cropping fracture traces and is trusted for results comparison and validation of other methods (e.g. Assali et al., 2014; Fisher et al., 2014; Park and West, 2002). A survey of the methods of fracture detection was summarized in Figure 2.

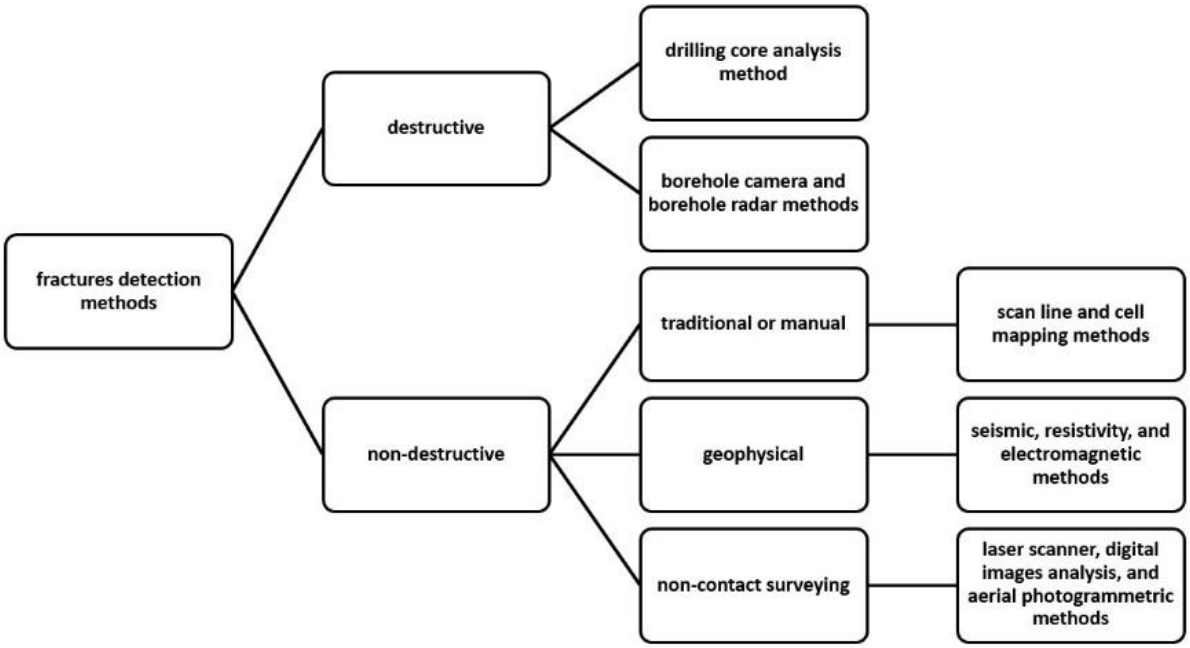

Figure 2: A classification survey of the methods of fracture detection.

Since ornamental stones are non-renewable resources of considerable economic value, a non-destructive fracture detection tool is recommended. The author selected GPR, among several fracture detection methods, as a geophysical electromagnetic data acquisition tool, for fracture detection. GPR has been widely used to detect fractures in quarries (e.g. Dérobert and Abraham, 2000; Forte and Pipan, 2007; Grandjean and Gourry, 1996; Kadioglu, 2008; Markovaara-Koivisto et al., 2014) of different rock type (Table 1) for several targets.

Table 1: A sample of studies used GPR to detect fractures in quarries of different rock type.

publications	rock type of quarry
(Seol et al., 2001)	marble quarry
(Grandjean and Gourry, 1996)	marble quarry
(Luodes et al., 2015)	granite quarry
(Luodes et al., 2000)	gneiss quarry
(Luodes and Sutinen, 2011)	granite quarry
(Rey et al., 2015)	marble quarry
(Lualdi and Zanzi, 2004)	limestone quarry
(Koster and Kruse, 2016)	marble quarry
(Grasmueck et al., 2004)	limestone quarry
(Yi et al., 2004)	granite quarry

2.2. Principles of GPR

A brief theoretical background of GPR is herein presented. GPR is based on the transmission of electromagnetic wave pulses (frequency ranging from 10.0 MHz to 2.6 GHz) in the material being surveyed and the receiver gains the reflected energy from discontinuities where there is a change in the dielectric properties (Annan, 2003). Low frequency antennas provide a large penetration depth but with limited resolution whilst high frequency antennas provide a more detailed subsurface image but with limited depth of pentration.

The electromagnetic waves spherically travels through a medium whose penetration depends mainly on the dielectric constant (or sometimes named relative permittivity) of the medium. The relation between the dielectric constant of a medium (ε_r) and the signal propagation velocity in the medium (v) is simply defined by Eq. (1) (Reynolds, 2011), where c is the electromagnetic velocity in free space (299,792,458 m/s). The time for transmitting the signal and its return back after reflection is known as double reflective time of the signal (t), which is later converted to a vertical depth (d) in the radargram by Eq. (2).

$$\sqrt{\varepsilon_r} = c / v \tag{1}$$

$$v = 2d/t \tag{2}$$

The resolution of a GPR system is the ability to distinguish between two reflections induced by anomalies or discontinuities which are close together within the medium. Sensitivity is the ability of the GPR system to detect small discontinuities and it is controlled by the signal-to-noise ratio. The signal-to-noise ratio is a measure of how well the reflected signal from a discontinuity can be deduced from the other background reflections (Annan, 2001). The

strength of amplitude reflection from discontinuity is controlled by a number of factors (Anthony, 2008): (i) the frequency, bandwidth and efficiency of the antenna, hence sensitivity generally increases with high frequency antennas, (ii) the inherent noise within the medium, and (iii) the reflectivity of the discontinuity which depends on the contrast between its electromagnetic properties and those of the medium, its size, shape, orientation and location with regard to the incident energy (Rhazi et al., 2004). Further theoretical basis of GPR and signal processing can be found in (Daniels, 2004; Reynolds, 2011; Yelfm, 2007).

CHAPTER 3

Deposit Evaluation Using Low Frequency GPR Antenna

3.1 Introduction and review

Evaluation of ornamental stone deposits is a decision making tool not only for quarrying, but also for classifying deposit quality. The aesthetical appearance of ornamental stones and the commercial size of ornamental stone blocks are very significant marketing factors (Ashmole and Motloung, 2008). Rock mass fractures hamper the cutting of commercially viable ornamental stone blocks. Fractures are also the main cause of production waste. For this reason, fracture status evaluation is a critical assessment factor during the exploration stage.

In this chapter, investigation of the use of a low frequency GPR antenna to detect critical (large aperture) fractures inside a discontinuous heterogeneous rock mass in a sandstone quarry is presented. Low frequency GPR antennas can be used for exploring the site geology, such as fractures, and detecting deep buried large objects (Annan, 2003; Davis and Annan, 1989). In a characterization of sandstone (White et al., 2004) and granitic rock (Mysaiah et al., 2011), a 100.0 MHz GPR antenna was used, achieving a penetration depth of about 16.0 m. Low GPR antenna frequencies of 50.0 and 100.0 MHz were used by (Jeannin et al., 2006; Theune et al., 2006) to detect the main discontinuities, in limestone, reaching to a penetration depths of about 20.0-30.0 m and 30.0-40.0 m respectively. The same rock type (limestone) is the predominant material in these two studies; however, the penetration depth is variable even with the same GPR antenna frequency. The main reasons of the penetration depth variability are the variable status of homogeneity, discontinuity, and saturation inside the rock mass that attenuate the signal and consequently decrease the penetration depth of the signal. The objective of using low frequency antenna is to obtain a subsurface image as deep as possible, since penetration depth is inversely proportional to wave frequency.

Selective extraction from an ornamental stone deposit first requires preliminary deposit classification into quality categories based on effective mechanical and physical properties (Abdollahisharif J. and Bakhtavar E., 2009; Sohrabian and Ozcelik, 2012). Since physico-mechanical properties, such as uniaxial compressive strength, porosity, etc., have a role in imposing restrictions on the uses of the ornamental stones products, laboratory rock tests were performed on representative samples from the deposit in the quarry bench under study. A promising combination of the GPR results and the laboratory tests results are then presented

to evaluate the deposit on the micro and macro scales. The macro scale was investigated with GPR to detect critical fractures in the whole surveyed volume of the bench while the micro scale was investigated by means of physico-mechanical laboratory tests on representing samples from the bench.

3.2. Case study site: a bench in a sandstone quarry

The quarry of the case study is located in Tosco-Emilian Apennines, near the village of Firenzuola, Metropolitan city of Florence, Italy. The sandstone of this region is characterized by a grey color, with fine grains compacted structure. There are various uses for this kind of stone; it has always been considered ideal for renovation work, prestigious interior and exterior residential work, commercial buildings with a minimalist style or large modern architectural works. In addition, this stone has been used in furnishings and outdoor works, landscaping, museums, sculptures and artistic restoration work (La Borghigiana Srl website, 2017). The sandstones of Firenzuola are clastic sedimentary rocks and belong to Marnoso-arenacea formation (marl and sandstone) (Figure 3). The sandstones extracted at Firenzuola are also known as “Pietra Serena di Firenzuola”; this name is well-known in the historical heritage of Italy since many monuments were made of this stone, especially in Tuscany Region (Bargossi et al., 2004). The mining area of “Pietra Serena di Firenzuola” is highlighted by a black rectangular in Figure 3b. The strata of this formation are steeply dipped. So that, the quarrying process is going on dip with the deposition in order to quarry large blocks, causing steep surfaces of benches in the quarries (Coli et al., 2012).

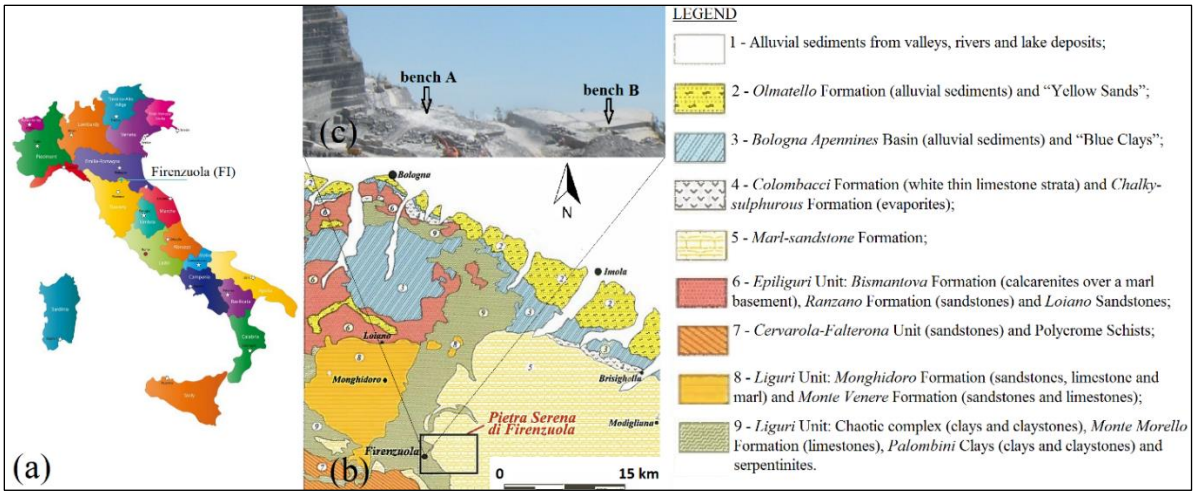

Figure 3: (a) The location of Firenzuola city in Italy, modified from (http://www.italythisway.com/regions/map-of-italy.php). (b) Lithologic map of the eastern portion of Tosco-Emilian Apennines. The legend was translated to English by the authors, modified from (Bargossi et al., 2008). (c) A panoramic view of the quarry with referring to the locations of the two benches under studying.

In this quarry, two benches were considered for the PhD research. In this Chapter, *bench A* is considered whilst the work in *bench B* will be presented in Chapters 4 and 5. The out-cropping strata of the bench under study belongs to the referred geologic formation. Stratification runs parallel to the bench surface (Figure 4a). Sandstones are characterized by several colors due to differences in their mineralogical composition, which in turn gives rise to differing physical and mechanical properties (Mubiayi, 2013). The out-cropping strata in the bench face in question were divided into two lithologic parts. The first was a yellow-to-yellowish gray sandstone series of strata. Under this was a gray sandstone stratum.

The bench was characterized by large aperture sub-vertical fractures (about 2.0 cm) (Figure 4b). Some large-aperture outcropping fractures were clearly seen to extend through all outcropping strata in the bench face, while other fractures stopped at the top surface of the gray sandstone stratum, as shown in Figure 5. This observation is limited to the large aperture fractures visible to the naked eye in the outcropping gray sandstone strata from Figure 5.

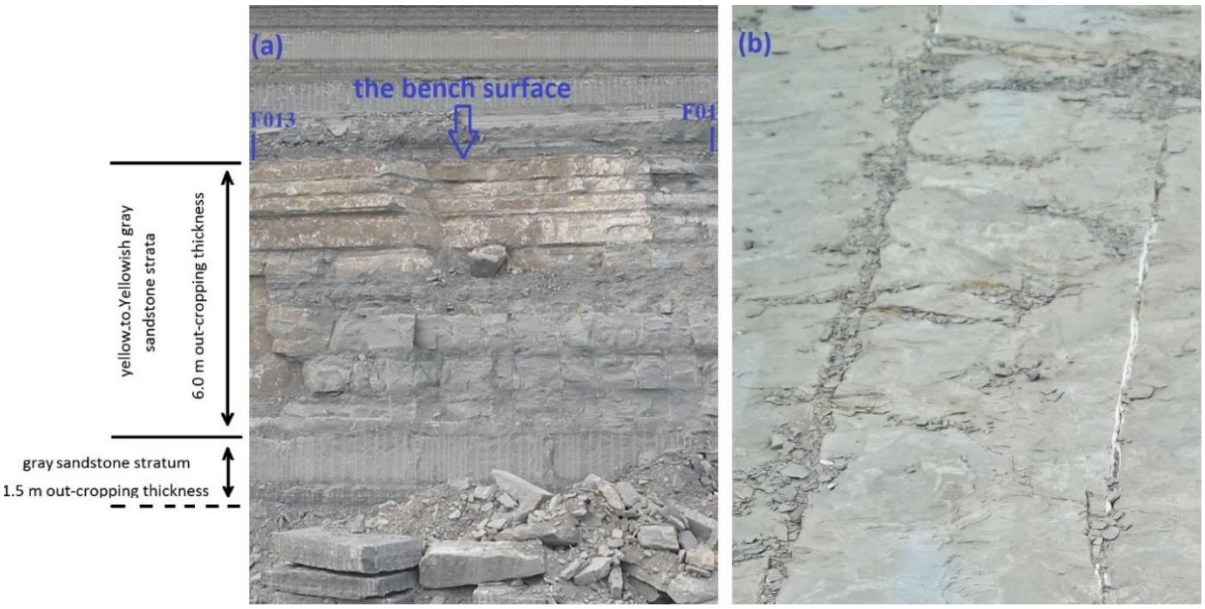

Figure 4: (a) Front view of the bench face, F01 and F013 are the first and last GPR survey lines in the X direction (see Figure7). (b) Some out-cropping fractures in the bench surface.

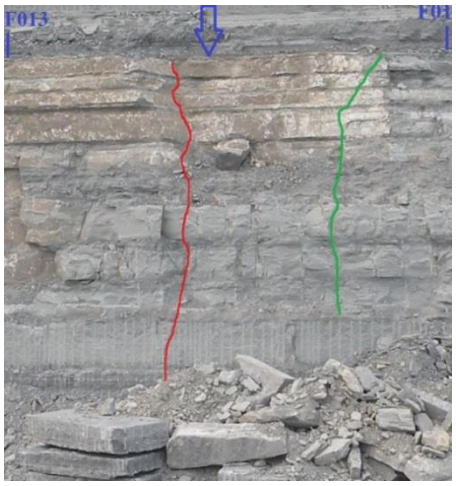

Figure 5: Tracing of a fracture surface extending through all the outcropping strata of the bench face (red) and a fracture surface stopping at the top surface of the gray sandstone stratum (green).

3.3. Method and results

3.3.1. GPR survey

The GPR survey aimed (i) to detect large aperture fractures at the greatest depth possible, (ii) explore fracture surface orientation and shape, and (iii) check the correlation between the out-cropping fractures on the bench face and the interior volume of the rock mass. The bench surface was surveyed by a GPR unit of a 70.0 MHz monostatic antenna, manufactured by Geophysical Survey Systems Inc. (GSSI) (Figure 6). The antenna was adapted to a cart and

linked to GSSI-SIR 3000 system. The GPR survey was carried out at a selected area in the bench surface exhibiting behavior typical for the stratigraphic and geo-structure features of whole the bench.

Figure 6: The used 70.0 MHz GPR unit, adapted to a cart by the author.

Planning of the survey lines over the bench surface is shown in Figure 7. The survey was carried out on an intensive GPR grid with a spacing of (1.0 m x 1.0 m) in order to condensate/ enhance the interpolation of reflections in the 3D GPR model. The survey grid was 12.0 m x 7.0 m, leading to 21 survey lines. The survey grid was designed 8.0 m from the bench face in order to investigate the fractures in the interior rock mass of the bench. It should be noted that the rock mass was wet in the time of GPR surveying since it had rained in the previous days. Accordingly, the fractures apertures were filled with water allowing stronger reflections in the radargrams. Standard signal processing functions were applied to the GPR data using the signal processing software package RADAN^{TM} (GSSI). The processing functions and parameters employed are listed in Table 2.

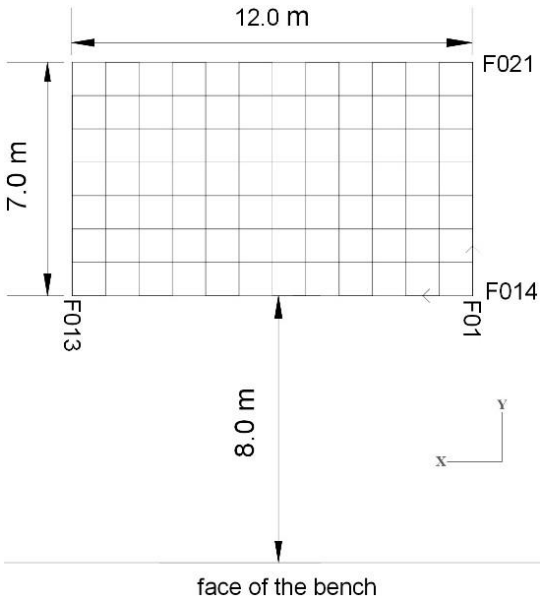

Figure 7: Design of the GPR survey grid.

Table 2: GPR processing functions used with RADAN™ software package.

time zero	3.91 ns
low pass filter	140.0 MHz
high pass filter	15.0 MHz
range gain	linear
migration	constant velocity migration of 111.0 μm/s
deconvolution	operator length: 31, predication lag: 5, prewhitening: 10%
display gain	6

3.3.1.1. Results

After standard signal processing, the 21 two-dimensional radargrams were interpolated by RADAN™, then, a 3D GPR model (Figure 8) and cross-sectional GPR slices (Figure 9) were built. The 3D GPR model shows the vertical reflections of large aperture fractures extending up to the maximum penetration depth of 14.0 m, revealing how the fractures extended into the bench body. The interior body of the rock mass presented predominantly the same behavior as the outcropping sub-vertical fractures. The cross-sectional GPR slices shows that the volumetric depth region, between about 5.0 to 10.0 m, was characterized by discontinuous reflections of fractures, however there were few detected continuous reflections, highlighted by black rectangles as shown in Figures 9b and 9d.

The GPR results evidenced that the majority of fracture reflections were discontinuous in a particular volumetric region between about 5.0 m to 10.0 m depth. At the bench face (Figure 4), a gray sandstone stratum cropped out at a depth of 6.0 m below the bench surface which

preliminary indicated that the gray sandstone strata was characterized by the lowest intensity of fracture reflections as compared to the whole rock body.

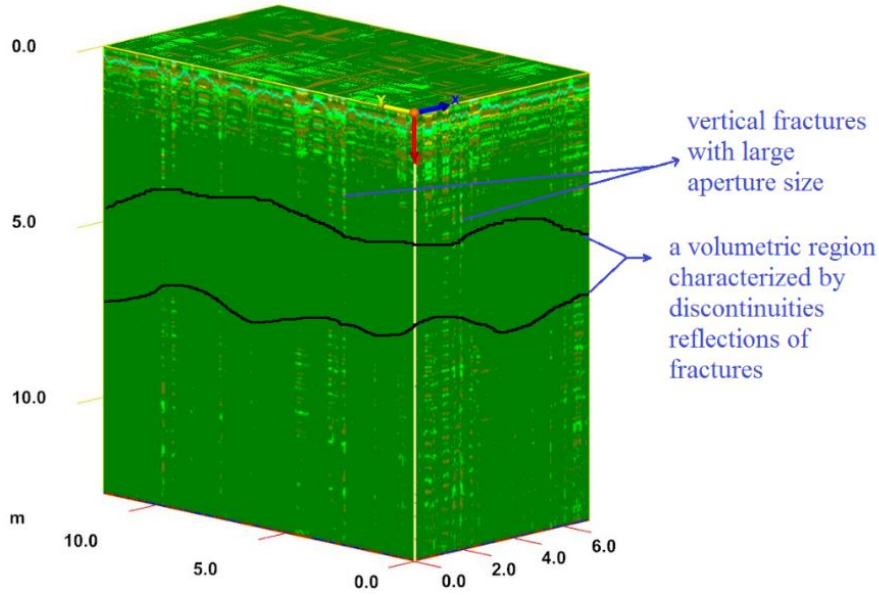

Figure 8: The 3D GPR model with indications of some vertical fractures and the volumetric region of discontinuous reflections of fractures.

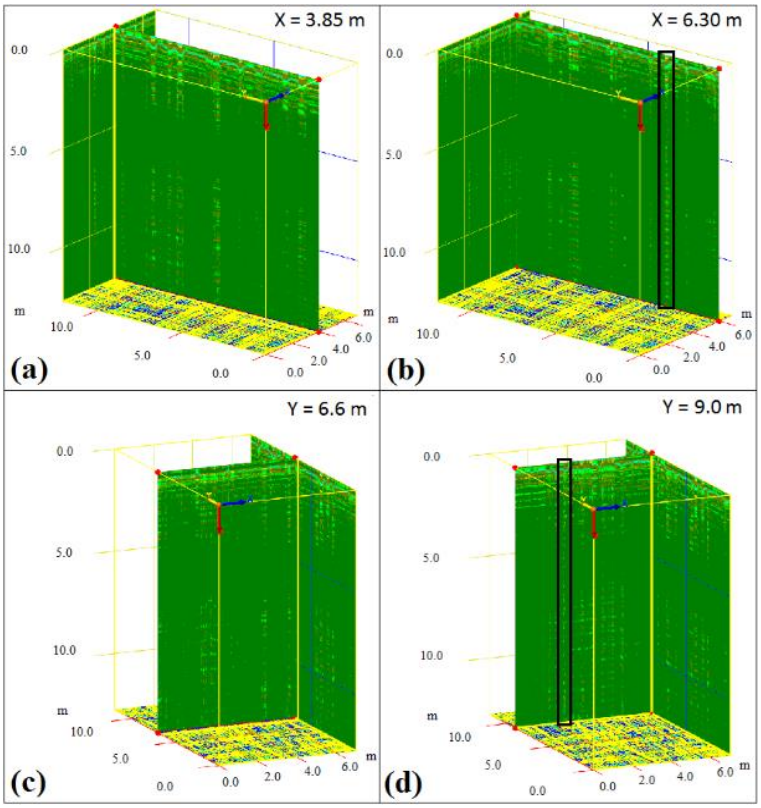

Figure 9: Cross-sectional GPR slices, in x and y directions, from the 3D GPR model.

Moreover, a transparent 3D GPR data visualization allowed for better understanding of the fractures status inside the whole rock mass body. The 3D transparent GPR model also confirmed the interpretation of the lowest amount of fractures reflections in the three-dimensional volumetric region between about 5.0 m and 10.0 m (Figure 10). By investigating the GPR models, it could be observed also that the rock mass in this bench was characterized by nearly two perpendicular sets of large aperture fractures, one set was perpendicular to the bench face and the other was parallel to the bench face.

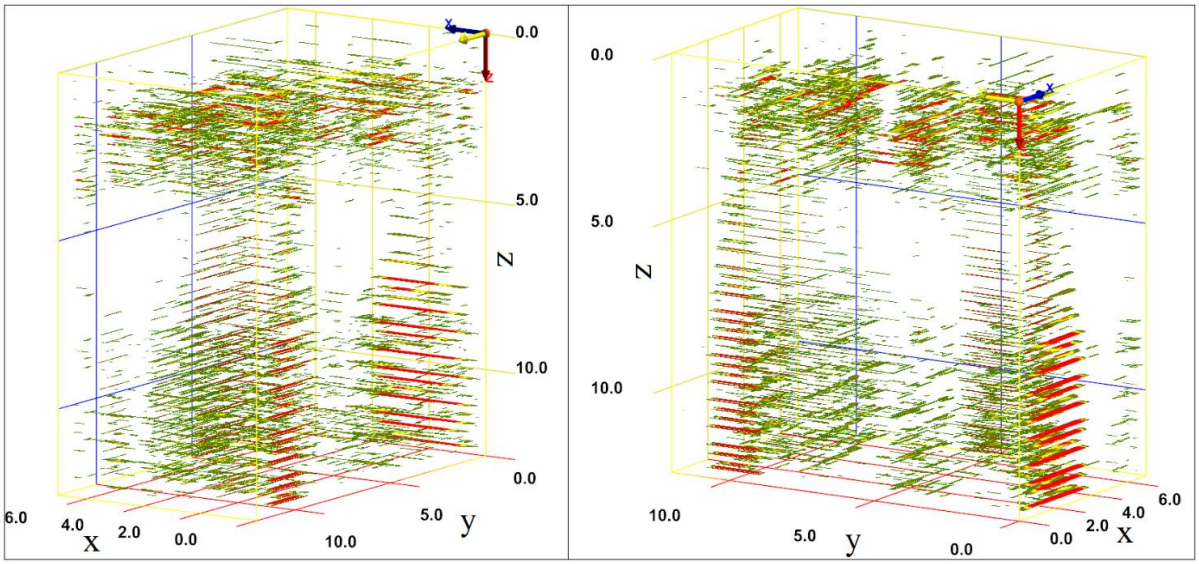

Figure 10: The 3D transparent GPR model visualized from two different orientations.

The waviness height of a fracture aperture can change with the variable stresses which a rock mass is subjected (Marji et al., 2012; Rutqvist, 2015). Moreover, Gudmundsson et al., 2009, demonstrated that the variation of stiffness in the path of a fracture surface causes variation in aperture. A stratum with highly resistant mechanical properties may not fracture or in the event of fracture, these may be so narrow as to be undetectable by low antenna resolution. In accordance with the above-mentioned interpretation of the discontinuous reflections of fractures, it was posited that the relatively higher mechanical properties of the gray sandstone stratum could be the reason why the gray sandstone stratum did not present with large aperture fractures. This interpretation was investigated by applying uniaxial compressive strength and deformation tests to samples collected from the bench strata (see Section 3.3.2). The results of the laboratory rock tests did not only serve the evaluation of the rock material as an ornamental stone deposit but also as a validation for the GPR interpretations as well.

3.3.2. Laboratory rock tests

The laboratory tests (Figure 11) were carried out on representative samples collected from the out-cropping strata on the bench face, following the methods suggested by the International Society of Rock Mechanics ISRM (International Society for Rock Mechanics (ISRM), 2007). The samples were divided into two main groups according to their lithologic nature. Group (G) were samples collected from the gray sandstone stratum, whilst group (Y) were samples collected from the yellow-to-yellowish gray sandstone strata. The samples were prepared as cylindrical specimens of 38 mm diameter and 76 mm height.

Density (ρ) and porosity (n) were measured by saturation and buoyancy techniques. The water absorption by weight (W) was also calculated. The p-wave velocity (v_p), in dry conditions, was measured with an ultrasonic instrument (a pulse generator of EPOCH1000 and 1.0 MHz transducers).

Uniaxial compressive strength (σ_c) was measured, under natural conditions, with a 500 KN load cell and an accuracy of 1%, by applying a continuous stress rate of 0.5 MPa/s. Uniaxial compressive strength was measured in one direction perpendicular to the bedding planes. A further deformation test was performed using strain gages, under natural conditions, on two representative samples of 38 mm diameter and 76 mm height, from both groups G and Y.

Figure 11: Some pictures taken during the laboratory tests.

3.3.2.1. Results

The results of the laboratory tests are presented in Table 3. The G samples were characterized by noticeably higher density than the Y samples. The average porosity and water absorption by weight of the Y samples were 1.6 and 1.5 times higher than the G samples respectively.

The gray sandstone stratum was characterized by higher mechanical compressive strength (about 1.37 times on average) than the strata of the yellow-to-yellowish gray sandstone. Figure 12 shows that the G sample was characterized by higher stiffness than the Y sample.

The mechanical laboratory results supported the absence of fracture reflections in the 3D GPR models (Figure 8, 9 and 10) in keeping with the finding that the G samples had higher mechanical properties than the Y samples. Accordingly, it is highly probable that fracture apertures in the gray sandstone strata were too small to be detected by the used antenna frequency.

Table 3: Statistical breakdown of the physico-mechanical properties measured

properties	group	No. of samples	minimum value	maximum value	average value
ρ (kg/m3)	Y	19	2460	2555	2515
	G	20	2505	2681	2580
n (%)	Y	19	5.72	9.24	7.26
	G	20	2.00	6.34	4.58
W (%)	Y	19	2.18	3.61	2.78
	G	20	0.74	2.76	1.80
Vp (m/s)	Y	19	2518	3410	2911
	G	20	2533	3919	3089
σc (MPa)	Y	19	69	94	86
	G	20	89	159	118

Figure 13 shows correlations between several physico-mechanical properties. Porosity decreases linearly with the increase of compressive strength and p-wave velocity (Figure 13a&b), while the density increases linearly with the increase of compressive strength and p-wave velocity (Figure 13c&d). The coefficients of correlations in Figure 13 show that the G samples were characterized by moderate to strong linear relations while the Y samples were characterized by weak linear relationships. This is evidently because the Y samples represented several stratum with slightly different lithological characteristics.

The laboratory tests showed the gray sandstone stratum as characterized by more resistant physico-mechanical characteristics. As a result, the bench examined was classed as having good quality gray sandstone, intermediate quality yellowish gray sandstone, and poor quality

yellow sandstone. The yellowish gray sandstone represents the rocks in a lithological transition zone between the gray sandstone and the yellow sandstone, as referred by red circles in Figure 13.

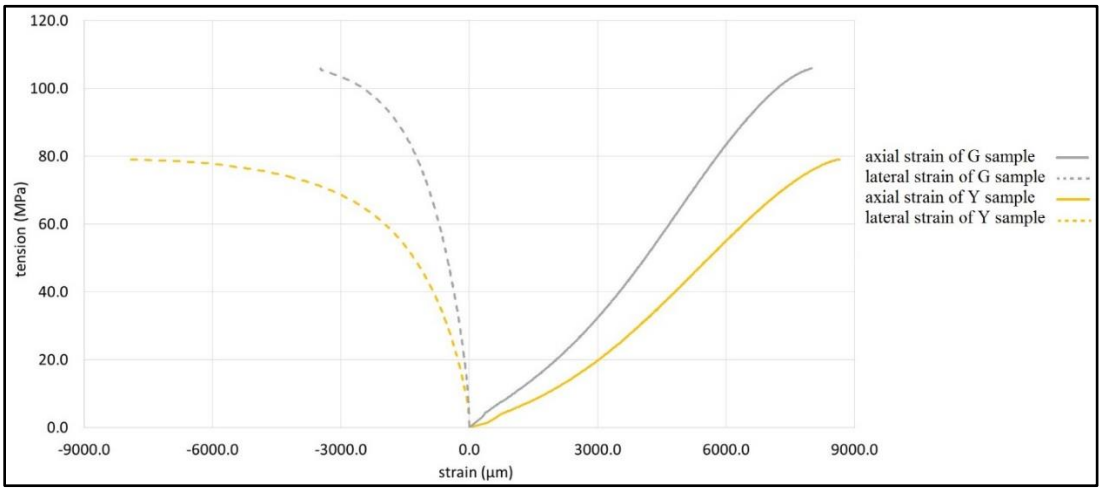

Figure 12: The stress-strain curve of two G and Y samples.

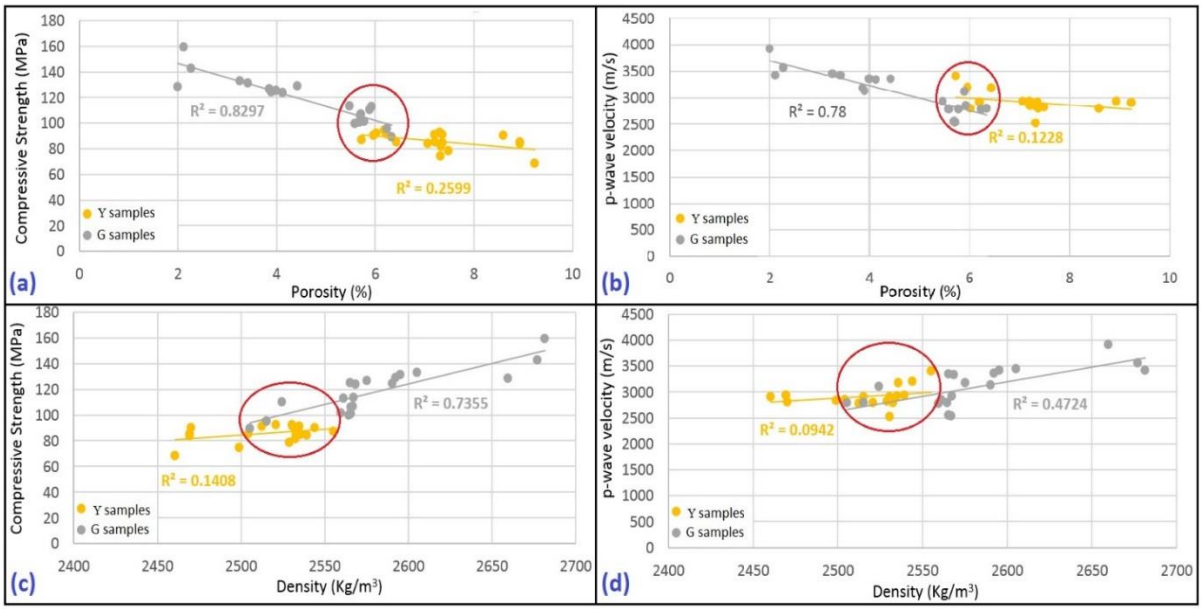

Figure 13: Correlations between (a) compressive strength and porosity, (b) p-wave velocity and porosity, (c) compressive strength and density, and (d) p-wave velocity and density.

3.4. Conclusions

A 70.0 MHz GPR antenna was able to detect large aperture fractures in a sandstone bench of lithologically differing strata. Although the maximum penetration depth achieved (14.0 m) in the fractured rock mass examined was limited on account of signal attenuation, penetration depth using this antenna may be greater in the case of more continuous homogeneous rock

bodies. Due to the limited resolution of low frequency antennas, an intensive GPR survey grid was used in this research to estimate, by interpolation, the reflections between the 2D cross-sectional radargrams. The use of a 3D GPR model led to the identification of a volumetric region of a rock stratum (gray sandstone) with a lower load of large aperture fractures than other neighboring strata of yellow-to-yellowish gray sandstone.

Together with the results of the GPR survey, the physico-mechanical properties obtained by laboratory tests, allowed the author to classify the deposit into quality categories. The gray sandstone was seen to have better physical and mechanical properties than the yellowish sandstone. Mechanical laboratory tests were also used to validate the interpretations of the 3D GPR models, leading the author to conclude that the combination of non-destructive in-situ geo-physical and destructive laboratory geo-mechanical tests is a promising tool for a sustainable evaluation of ornamental stone deposits.

CHAPTER 4

Deterministic Fracture Modelling Using High Frequency GPR Antenna

4.1. Development of a three-dimensional fracture modeling approach

4.1.1. Introduction and review

An accurate 3D detection and modeling of rock mass fractures is required (i) to obtain a preliminary deposit evaluation before quarrying, (ii) to optimize the cutting direction of stone blocks which minimizes the waste. The author defines the fractures deterministic model as the model that represents the geometric set and behavior of fractures as close as possible to reality without stochastic processes. However, the modeling of rock mass fractures, in a full 3D deterministic way, is quite difficult because of: (i) data acquisition resolution, (ii) interpolations, (iii) assumptions or manual interpretations of fractures data that may exist in a model. This section presents the application of the GPR method to fracture detection and modeling in a bench of a sandstone quarry. The author introduces improvements to the deterministic modeling of fractures and a new analytical methodology to obtain an evaluation-based fracture index, for a quarry bench, from GPR survey.

Several applications for detecting and characterizing fractures through GPR in quarries of different deposits have been presented in the literature (Botelho and Mufti, 1998; Kadioglu, 2008; Luodes, 2008; Mysaiah et al., 2011; Porsani et al., 2006; Zajc et al., 2013). With respect to 3D deterministic modeling of fractures from GPR survey in quarries, the most noticeable contributions are the works in (Grandjean and Gourry, 1996; Grasmueck, 1996; Grasmueck et al., 2013). The fracture modeling approach proposed in this section aims at improving the level of deterministic accuracy and decreasing the gap among these contributions in the application to highly fractured rock mass. The author defines the deterministic accuracy level as the level of modeling the geometric features of fracture surfaces as close as possible to reality.

The application of (Grandjean and Gourry, 1996) was carried out in a marble quarry. This method interpolated the picked fractures, from parallel 2D radargrams, in a gridded domain in which a 3D fracture surface was modeled. The conditioned grid domain in this approach may affect the deterministic accuracy level of a modeled fracture surface. The proposed approach models a fracture surface in a domain in which just the belonging reflections of a fracture surface are detected. The application of (Grasmueck, 1996) was performed in a gneiss quarry. The migrated GPR cuboid was loaded into an interactive 3D processing and interpretation

software package. Then, an automatic tracking program tracked the continuity of a fracture surface (horizon) from manual picks of the uppermost continuous troughs of the reflection bands in the GPR cuboid (Grasmueck, 1996). In this approach, a modeled fracture surface was a result of two successive phases of interpolations: (i) building the 3D GPR cuboid by the processing software and (ii) using the tracking algorithm. The proposed approach takes into consideration the modeling of small surface area fractures that do not appear as uppermost continuous troughs of the reflection bands in the GPR cuboid. The application of (Grasmueck et al., 2013) performed a 3D GPR survey that produced high resolution imaging of sub-vertical fractures in a limestone quarry. Inserting the migrated GPR cuboid to a visualization and interpreter software package (Geoprobe^{TM}) identified sub-vertical fractures. The proposed modeling approach is feasible when no interpreter software package is available. In this section (4.1), the author aimed at testing the applicability of the developed fracture modeling approach in a small scale area.

4.1.2. Case study site: a small scale area of a bench in a sandstone quarry

The case study of this section is bench B of the sandstone quarry in Firenzuola, Italy (Figure 3). The geo-coordinates of the bench center under study correspond to a latitude of 44° 8′ 8.5452″ N, a longitude of 11° 25′ 8.3172″ E and a height of 857.0 m above sea level. The rock mass of the bench was highly fractured. The vertical fractures had aperture sizes larger than the horizontal fractures. In general, the aperture size of the fractures ranged from about 0.4 cm to 3.0 cm. The owner company of this quarry considered this bench as a non-mineable area. The bench surface was quite flat and suitable for the GPR survey activities. The pictures in Figure 14 show the bench of the case study (Figure 14a), some of the irregular outcropping fracture surfaces in the bench surface traced by yellow dashed lines and indicated by black arrows (Figure 14b), and some of the outcropping fractures in the bench face (Figure 14c).

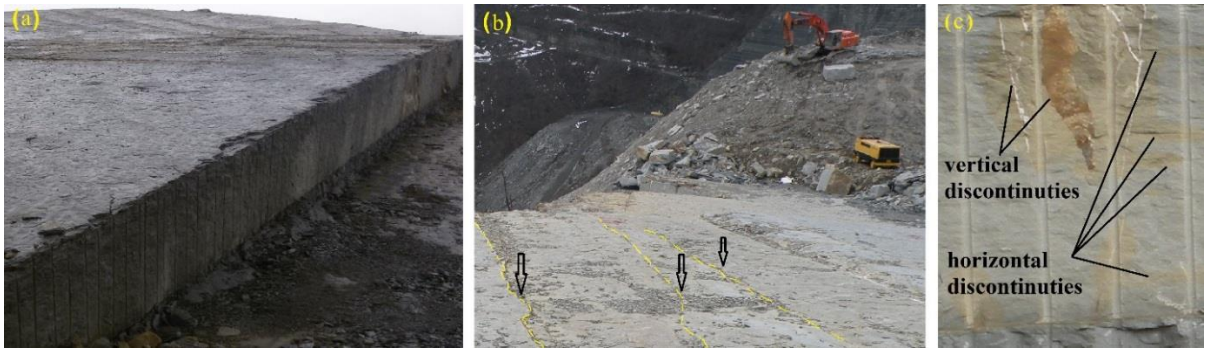

Figure 14: The bench of the case study with the marking of some out-cropping fractures in the bench surface and face.

There were three different colors of sandstone strata that cropped out in the face of the bench (Figure 15). The stratification from up to down was blackish gray sandstone, gray sandstone, and black sandstone. The measured vertical outcropping thicknesses of these strata were about 0.3 m, 1.25 m and 0.3 m respectively. The visual identification of the sandstone colors was carefully recognized due to the slight difference between the grayish and blackish grayish strata.

Figure 15: Recognition of different sandstone beds by visual observation for the bench face. On the right hand side of this picture, an irregular sub-vertical fracture surface crops-out.

4.1.3. Method and results

The key focus of this research was to use GPR as a data source for the 3D modeling of fractures in a deterministic approach. The modeling of fractures from GPR data could be carried out using an interpretation tracing technique that follows a fracture surface based on continuity indicators in parallel radargrams. Geometric features (dip, dip direction, vertices coordinates) of the modeled fractures could be then obtained through geometric formulations.

Consequently, the 3D fractures model could be visualized by coding the obtained geometric features in a visualization software package.

4.1.3.1. GPR survey

The GPR instrument used in this study (Figure 16) consisted of SIR operating System-3000, equipped with a 400.0 MHz shielded antenna adapted to a cart (all produced by Geophysical Survey Systems GSSI^{TM}). The 400.0 MHz antenna was selected considering the required penetration depth, the resolution range, and previous published works accomplished with the objective to detect fractures in sandstone rock mass (Aqeel et al., 2013; Maerz and Kim, 2000). It was showed that only the 400.0 MHz antenna, among 400.0, 500.0 and 900.0 MHz antennas, penetrated deeply enough, up to 3.0 m, in a sandstone rock mass to clearly identify the fractures (Maerz and Kim, 2000). Similarly, an application to detect fractures in a sandstone rock cut was carried out by a 400.0 MHz antenna reaching a penetration depth of 4.0 m (Aqeel et al., 2013).

Figure 16: The used GPR unit.

The surveying was carried out on a cold winter day characterized by a temperature of 5.6 ˚C and a relative humidity of 61 %. The rock mass was relatively wet because of rains in the previous days, leading to higher amplitude reflections from fracture apertures filled with water (Toshioka et al., 1995) and limiting the penetration depth since water attenuates the signal.

After testing the response of the signal in the rock mass of the bench, the preliminary data acquisition parameters could be estimated. A time range of 100 ns, 512 samples/scan, a format

of 16 bits/sample, a rate of 120 scans/s, high pass filter of 100.0 MHz, low pass filter of 800.0 MHz and a linear range gain of two points (-20 dB, 61 dB) were setup in the GPR system. Four lines (F01, F02, F03, and F04) parallel to the bench face, with an interval of 2.0 m and a length of 25.0 m each, were surveyed by the GPR (Figure 17). The bearing of the parallel survey lines was measured by a Brunton compass with respect to the North and was 130.0°. The first survey line (F01) was 2.0 m far from the vertical bench face to move the GPR cart safely. Radargram F01 had a surveying delay of 1.25 m because of a non-smooth and non-safe surface area that was ignored during the surveying. The survey lines were oriented to be parallel to the bench face in order to be perpendicular to the outcropping sub-vertical fractures in the bench surface, following (Kadioglu, 2008; Seren and Acikgoz, 2012; Tsoflias et al., 2004).

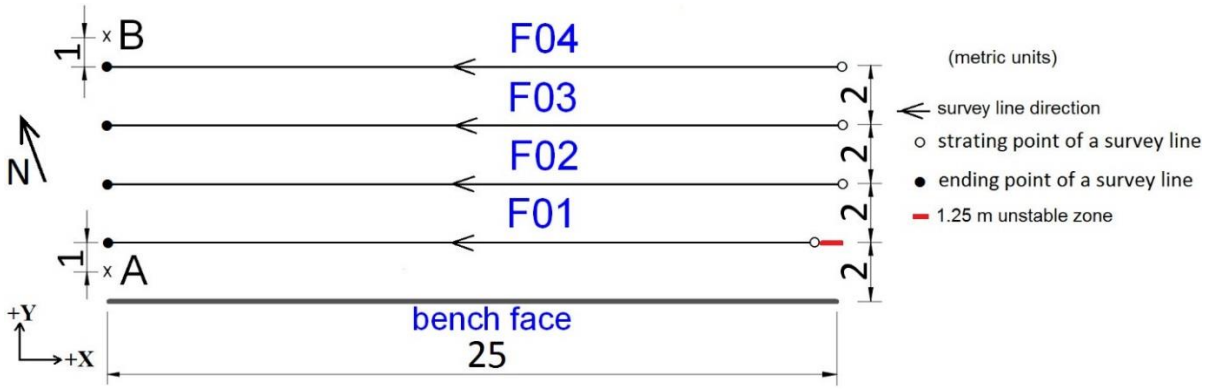

Figure 17: A plan view of the survey lines over the bench surface. Points A and B are reference points which will be used in Section 4.1.5.

4.1.3.2. Estimation of a representative dielectric constant for the rock mass

Estimation of the signal propagation velocity of the medium is required to estimate ε_r from Eq. (1). The used signal processing software package (RADAN^{TM}), in this study, allows to use a single value of ε_r, for a radargram, to convert the double travel time to a depth. The inaccurate estimation of ε_r strongly affects the true location of reflectors.

Rock mass formations are a mix of materials with different dielectric properties; for example, fractured rock mass may contain different strata and different filling materials of fracture apertures such as water, air, gas, oil or sediments. That's why, finding ε_r of an intact rock in laboratory will not accurately represent the rock mass. Even if many different rock samples were collected from the site with preserved physical conditions, they cannot accurately represent the heterogeneous and discontinuous character of the rock mass. It is recommended, when possible, to obtain a representative ε_r of the rock mass in the time of data acquisition,

for applications that require high accuracy in detecting subsurface anomalies at accurate depth, rather than using published values or values obtained in laboratory from intact rock samples. The following paragraphs describe how a representative ε_r was obtained for this case study through a technique named in literature as "known depth to reflector" (American Society for Testing and Materials (ASTM): D6432-11, 2011). This technique was used by (Maerz et al., 2015) to find the dielectric constant for a sandstone block in laboratory. The author applied this technique in-situ to obtain a more representative result for the rock mass body.

In a correlation study between sandstone colors and water adsorption performed by (Mubiayi, 2013), it was proved that blackish sandstone has a maximum water absorption capability among 6 sandstone samples with different colors. In contrast, the grayish sandstone has a minimum water absorption capability. From this point and according to the wet rock mass condition, it was expected for the blackish sandstone stratum to have the highest water content. A preliminary analysis of radargrams showed that the boundaries of the strata are almost perpendicular to the bench surface. The detection of the strata boundaries in the radargrams depends on the amount of amplitude reflections. The reflections in the blackish sandstone stratum were the strongest, as expected, because of the high water content in this stratum (see F01 as an example in Figure 18). As shown in Figure 18, the gray sandstone has the weakest amplitude reflections (mostly the white zone) and the blackish gray one is in an intermediate phase of the water content. The lower boundary of the grayish sandstone (referred by a blue line in Figure 18) was selected as a horizontal reflector reference because it is the deepest reflector that crops out in the face. Therefore, a more representative value of ε_r will be estimated since the signal passes through the major part of the rock mass under study. The lower boundary of the grayish sandstone was detected in the radargrams almost at double reflective times of 27.4, 28.1, 27.7 and 27.9 ns in F01, F02, F03 and F04 respectively.

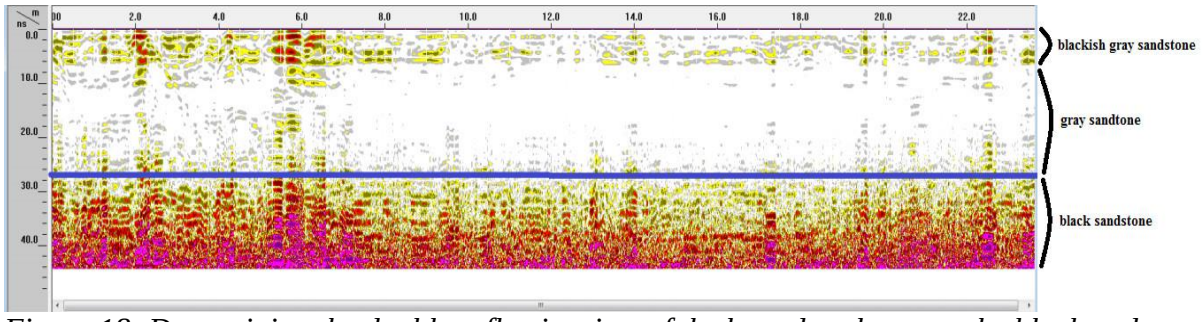

Figure 18: Determining the double reflective time of the boundary between the black and gray sandstone strata from radargram F01.

Knowing the depth of the lower boundary of the grayish sandstone strata that is visible from the bench surface (1.55 m) and the average double reflective time of this boundary (27.77 ns), the average signal propagation velocity in the rock mass could be calculated from Eq. (2). Thus, a representative ε_r for the rock mass of 7.2 was obtained from and Eq. (1). This estimated value is acceptable, since as given by (Daniels, 2004), the dielectric constant range of sandstone in wet conditions is in a range of 5.0 to 10.0.

The presented method of estimating bulk dielectric constant for this rock mass body may lead to some few uncertainties regarding the subsurface location of anomalies in the radargrams. Assuming that the depth of the lower boundary of the grayish sandstone strata (1.55 m) was constant through the whole rock body, absolute errors in the subsurface depth of anomalies were estimated as shown in Table 4.

Table 4: Absolute errors estimation regarding the proposed method of estimating bulk dielectric constant.

radargram	absolute error (cm)
F01	2.15
F02	1.76
F03	0.47
F04	0.64

4.1.3.3. GPR data interpretations

After applying standard signal processing functions, noise was removed. A deconvolution processing function was also applied, since it is important for optimally enhancing the range resolution below the quarter of the wave length (Widess, 1973) by maximizing the bandwidth and minimizing the GPR pulse dispersion. The reconstruction of the true shape of the detected fractures was carried out by applying migration (Botelho and Mufti, 1998).

The boundaries of the three sandstone strata were interpreted in Figure 19 where the yellow lines refer to the boundary between the blackish gray sandstone strata and the gray sandstone one, whilst the red lines refer to the boundary between the gray sandstone strata and the black one. The boundaries of the strata appeared in the radargrams as slightly irregular surfaces with a dominant orientation parallel to the bench surface. Therefore, the boundaries were interpreted as lines in the 2D radargrams.

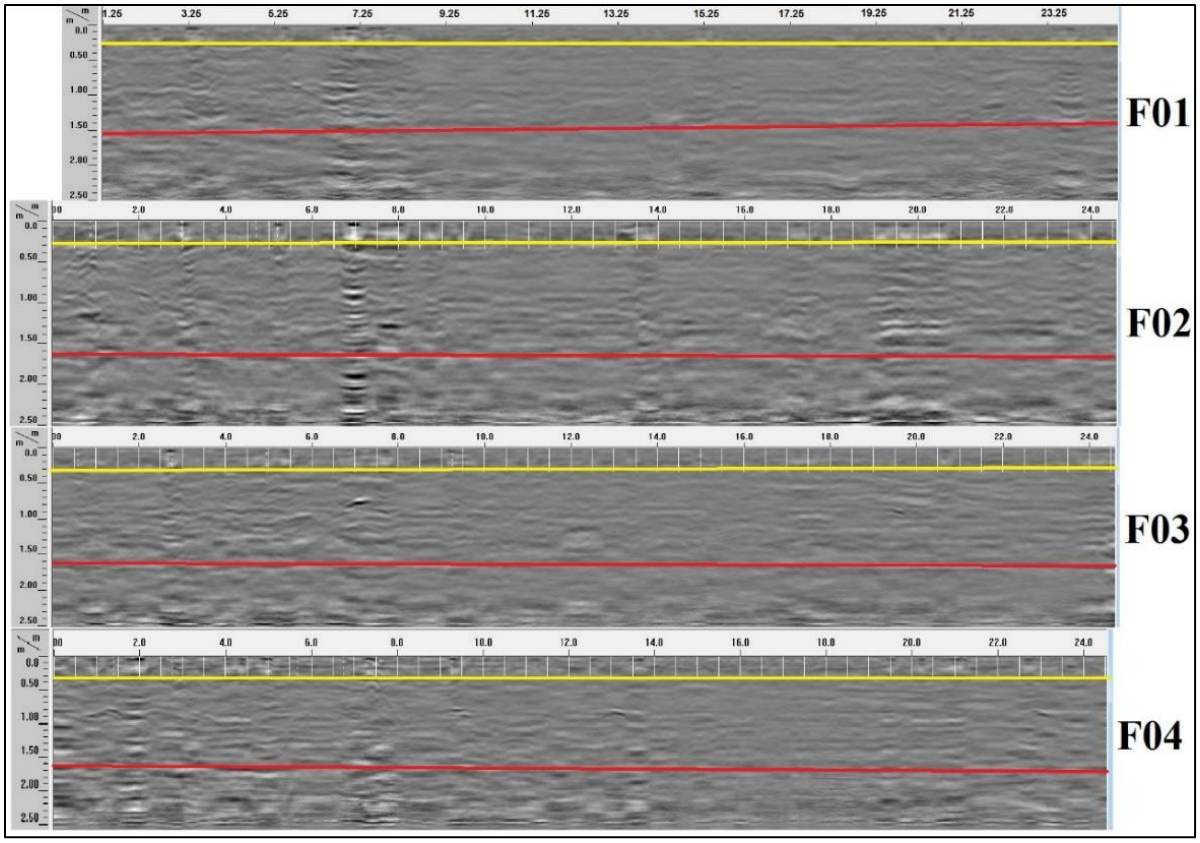

Figure 19: The processed radargrams with interpretation of the stratification boundaries of the sandstone strata.

A fracture tracing interpretation technique is proposed herein to model fracture surfaces. A fracture trace is the line (fracture reflection) resulting from the intersection between a fracture surface and a cross-sectional radargram. The proposed interpretation technique traces a fracture surface depending on the continuity indicators of a fracture trace in successive radargrams. The continuity indicators are determined by the amount of reflection amplitude, inclination, location, and length of fracture trace reflections. The vertical and the horizontal fractures were interpreted separately because of the highly fracturing status of the rock mass.

The tracing technique was applied to interpret vertical fracture surfaces in such a way that each single detected fracture trace belonging to a fracture surface was highlighted by a particular color in each radargram (Figure 20). Some of the interpreted vertical fractures (black color) could not be traced in more than one radargram. These fractures were without a continuity indicator, while others such as the yellow and cyan fracture surfaces extended all over the surveyed area. Some vertical fractures, such as the creamy color one (Figure 20), were detected only in a particular surveyed volume (F01 and F02) without more continuity indicators. The

interpretations showed that not all the outcropping vertical fractures in the bench extend in all the penetration depth (see as examples the green and pink fractures on the left hand side of Figure 20).

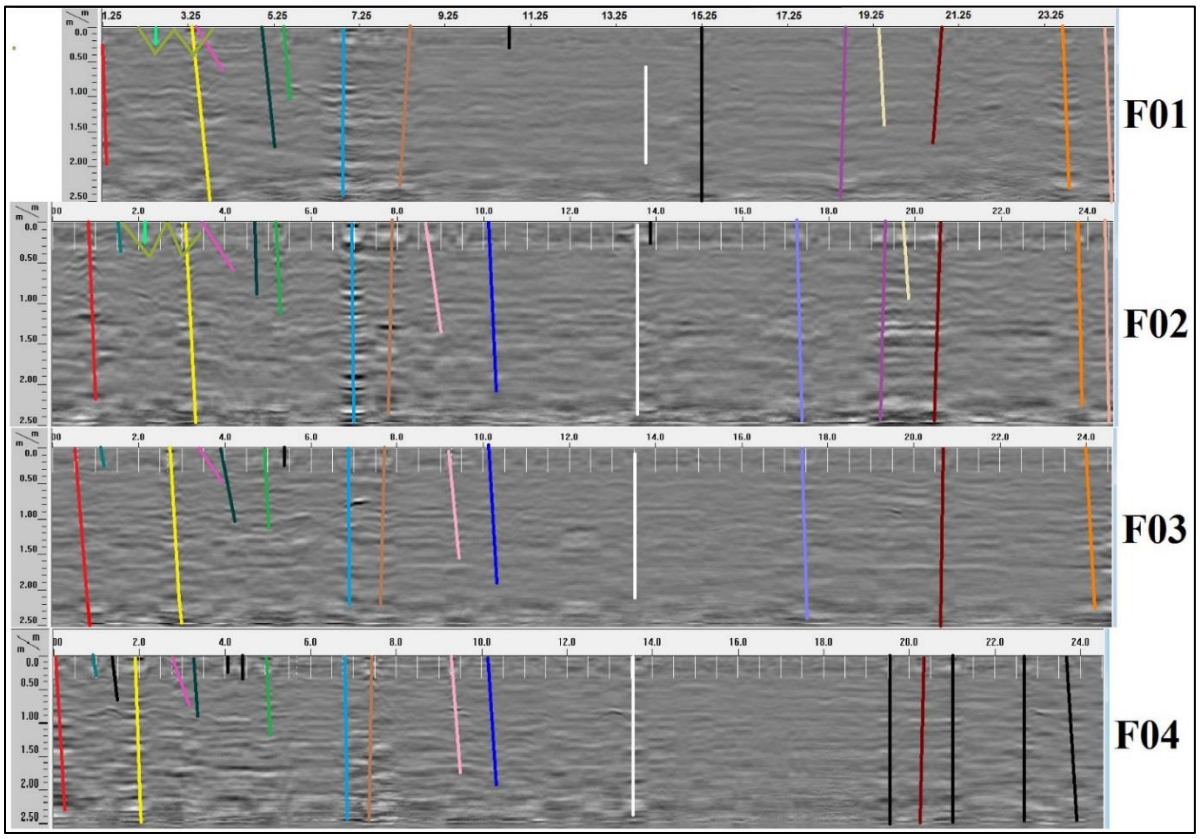

Figure 20: Interpretation of vertical or sub-vertical fractures by using the fracture tracing interpretation technique.

The horizontal and sub-horizontal fracture reflections in this rock mass showed a random fracture pattern with higher intensity and variety in characteristics. The horizontal fracture reflections were interpreted as single appearing reflections (Figure 21) because of difficulties to find continuity indicators. It is worth mentioning that the reflection spots from the vertical fractures were avoided in the interpretation of horizontal fracture reflections.

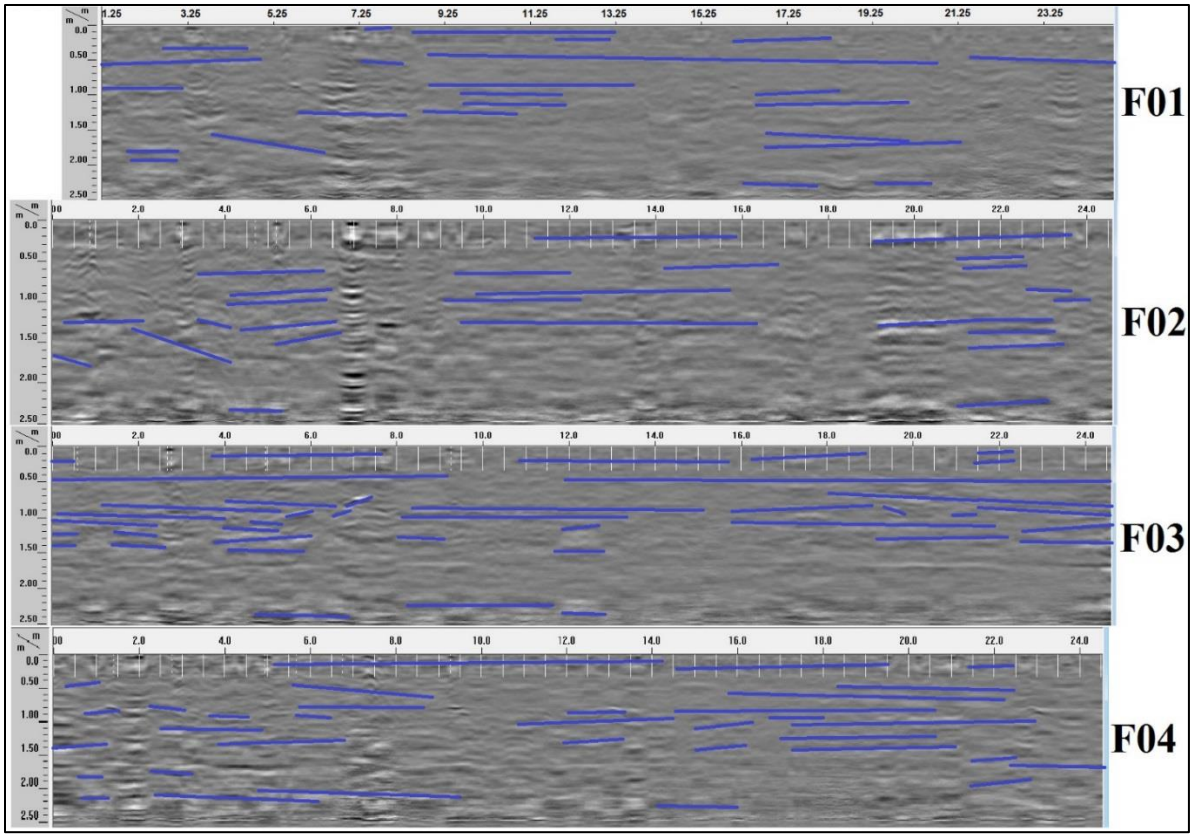

Figure 21: Interpretation of horizontal or sub-horizontal fractures.

4.1.3.4. Modeling and visualization

4.1.3.4.1. Fracture modeling formulations

Fractures propagate in the rock mass as irregular surfaces; however, they are usually modeled as planes for simplicity. The developed deterministic modeling approach represents the fractures not only as planes, but also as 3D surfaces. The geometric features of fractures (dip, dip direction, length, vertices coordinates) were obtained by developing Excel spreadsheet formulations for two schemes. The first scheme was for Fractures Interpreted by the Tracing Technique (FITT), mostly vertical fractures in this case study (Figure 20). The second scheme was for Fractures Interpreted as Single Appearance (FISA) in a radargram, mostly horizontal fractures (Figure 21) in this case study or few vertical fracture traces without continuity indicators. The input and output parameters of FITT and FISA formulations are listed in Table 5.

Table 5: Inputs and outputs of FITT and FISA formulations.

formulation	inputs	outputs
FITT	▪ Extremity coordinates of fracture traces (X, Z). ▪ Bearing of the survey lines. ▪ Interval between the survey lines.	▪ Trend and plunge of fracture traces. ▪ Length of all fracture traces. ▪ Dip, dip direction and strike of modeled surfaces. ▪ Generating and arranging of vertices coordinates of fracture surfaces.
FISA	▪ Extremity coordinates of fracture traces (X, Z). ▪ Bearing of the survey lines. ▪ Interval between the survey lines. ▪ Number of surveying lines. ▪ Offset from the bench face.	▪ Trend and plunge of fracture traces. ▪ Length of all fracture traces. ▪ Dip, dip direction and strike of modeled planes. ▪ Generating and arranging of vertices coordinates of fracture planes.

The fractures modeling concept used in this section is close to the one published in (Grandjean and Gourry, 1996), in particular, for the modeling of vertical fracture surfaces. The fractures model approach in (Grandjean and Gourry, 1996) was based on correlating the detected fracture reflections (spots) in the parallel radargrams and then interpolating a 3D fracture surface in a regular spaced grid (Figure 22a). Accordingly, some spots-free areas in a modeled fracture surface were included as a part of a fracture surface, neglecting that there might be multiple separate surfaces of fractures. The modeling approach presented in this section models a fracture surface without a dimensioned grid and just depends on the interpolation of the detected traced extensions (Figure 22b). The reason is to decrease the amount of assumptions, particularly for regions without data.

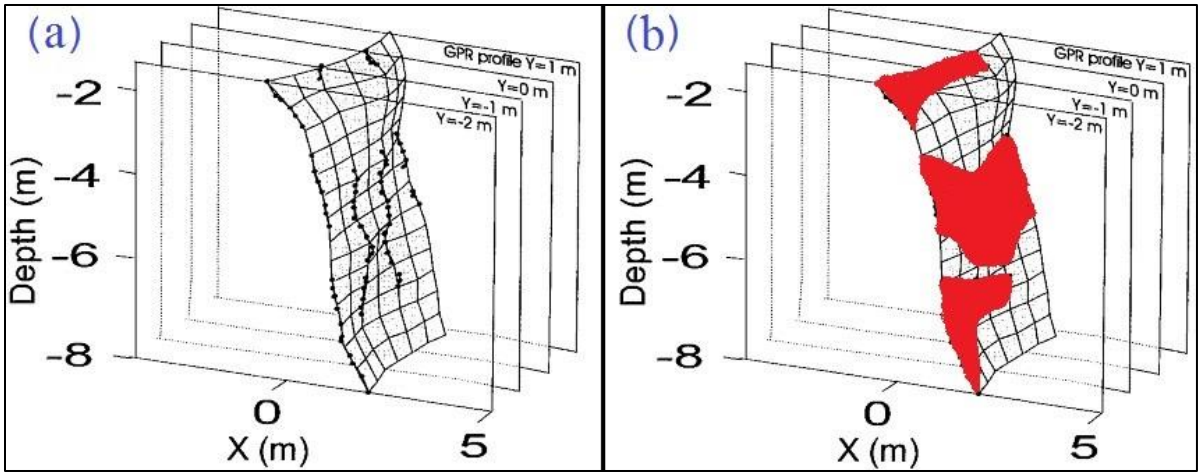

Figure 22: The proposed method interpolates fracture surfaces just from detected reflections in parallel radargrams ignoring the reflections-free areas (a simulation to the proposed method by 3D red surfaces is shown on the right) and does not interpolate a fracture surface in a conditioned regular spaced grid (Grandjean and Gourry, 1996) as shown on the left.

For the FITT formulation, the majority of the interpreted fracture traces of a fracture surface had different plunges (δ) and coordinates (x, z) in the successive radargrams (Figure 23). The FITT formulation calculated the dip direction (ϕ) and strike (α) of the regression plane of a fracture surface. The bearing of the survey lines was necessary to calculate the dip direction of a fracture plane. The dip angle (θ) of a regression plane was calculated by taking the average of δ. The trend (γ) of a fracture trace was assumed to be either in the bearing of the survey lines (130.0˚) or in the opposite direction (310.0˚).

On the other hand, for FISA, the formulation was different because it modeled each single fracture trace as a plane extending in half the interval distance before and after the radargram in which the fracture trace was detected. Each fracture plane took a dip angle and a dip direction equivalent to δ and γ of the belonging fracture trace. The single fracture traces detected in the first and last radargram were modeled as planes extend just inside the limit of the surveying area 6.0 m x 25.0 m.

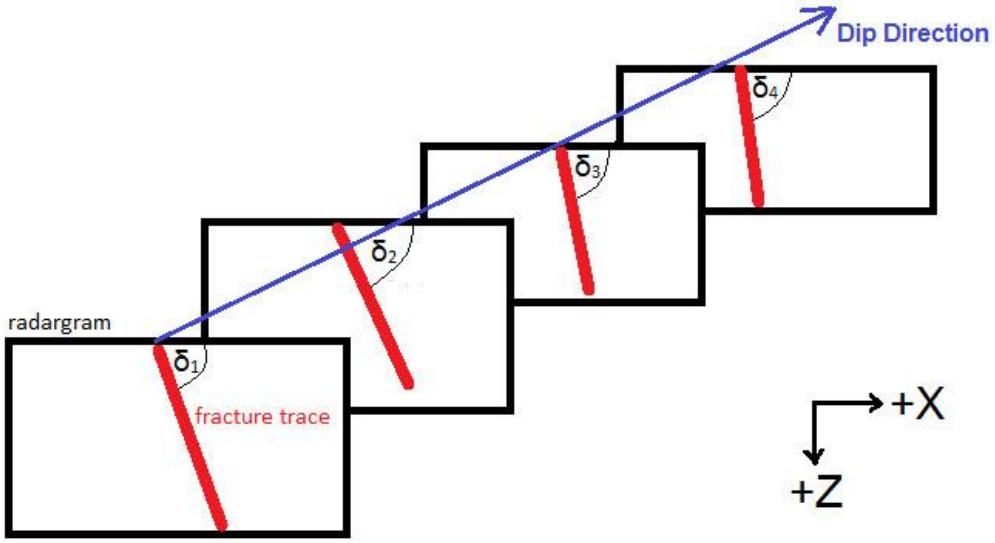

Figure 23: A sketch illustrates how FITT formulation obtained the dip and dip direction of a fracture surface.

For a 3D visualization of the modeled fractures, the vertices coordinates of each fracture surface or plane were generated and arranged by the two formulations, in a specific order necessary for a visualization programming code. In this case study, the FITT formulation was applied to 66 fracture traces that led to define the geometric features of 22 vertical fracture surfaces, whilst, the FISA formulation was applied to 133 single fracture traces producing 133 modeled fracture planes. Some numerical data from the spreadsheets of FITT and FISA formulations are shown in Table 6 and Table 7 respectively.

Table 6: Numerical data from FITT formulation for modeled fracture surfaces. The fracture surfaces No.1 and No.11 are the data of fracture surfaces interpreted in red and blue colors in Figure 20 respectively.

fracture No.	No. of frac. traces	radargram.	(X_2,Z_2) higher point		(X_1,Z_1) lower point		δ	γ	θ	α	ϕ	length, m	surfaces vertices coordinates					
			X_2 m	Z_2 m	X_1 m	Z_1 m							X_3 m	Z_3 m	Y_3 m	X_4 m	Z_4 m	Y_4 m
1	4	1	1.4	0.2	1.5	2.0	86.7	130.0	82.3	28.0	118.0	1.8	1.4	0.2	0.0	1.5	2.0	0.0
		2	0.8	0.0	1.1	2.2	82.2	130.0				2.2	0.8	0.0	2.0	1.1	2.2	2.0
		3	0.5	0.0	1.0	2.5	78.7	130.0				2.5	0.5	0.0	4.0	1.0	2.5	4.0
		4	0.1	0.0	0.4	2.3	81.3	130.0				2.3	0.1	0.0	6.0	0.4	2.3	6.0
..	..	..	..	..	..	..	..	..	..	..	..	..	..	..	..	..	..	..
11	3	2	10.1	0.0	10.3	2.1	84.8	130.0	83.8	38.6	128.6	2.1	10.1	0.0	4.0	10.3	2.1	4.0
		3	10.2	0.0	10.4	1.8	84.0	130.0				1.8	10.2	0.0	6.0	10.4	1.8	6.0
		4	10.2	0.0	10.5	1.9	82.5	130.0				1.9	10.2	0.0	8.0	10.4	1.9	8.0
..	..	..	..	..	..	..	..	..	..	..	..	..	..	..	..	..	..	..
22	..	..	..	..	..	..	..	..	..	..	..	..	..	..	..	..	..	..

Table 7: Numerical data from FISA formulation for modeled horizontal fracture planes from detected fracture traces in radargram F01 (Figure 21).

frac. trace	(X_2,Z_2) higher point		(X_1,Z_1) lower point		δ	γ	length, m	planes vertices coordinates											
No.	X_2 m	Z_2 m	X_1 m	Z_1 m				X_3 m	Z_3 m	Y_3 m	X_4 m	Z_4 m	Y_4 m	X_5 m	Z_5 m	Y_5 m	X_6 m	Z_6 m	Y_6 m
1	2.8	0.4	4.8	0.4	0.0	130.0	2.0	2.8	0.4	0.0	2.8	0.4	1.0	4.8	0.4	0.0	4.8	0.4	1.0
2	5.0	0.5	1.3	0.6	0.8	310.0	3.8	5.0	0.5	0.0	5.0	0.5	1.0	1.3	0.6	0.0	1.3	0.6	1.0
3	1.3	0.9	3.1	0.9	0.0	130.0	1.8	1.3	0.9	0.0	1.3	0.9	1.0	3.1	0.9	0.0	3.1	0.9	1.0
4	1.6	1.8	3.1	1.8	1.1	130.0	1.5	1.6	1.8	0.0	1.6	1.8	1.0	3.1	1.8	0.0	3.1	1.8	1.0
5	1.7	2.0	3.1	2.0	2.1	130.0	1.4	1.7	2.0	0.0	1.7	2.0	1.0	3.1	2.0	0.0	3.1	2.0	1.0
6	3.7	1.6	6.5	1.8	4.2	130.0	2.8	3.7	1.6	0.0	3.7	1.6	1.0	6.5	1.8	0.0	6.5	1.8	1.0
..	..	..	..	..	..	..	..	..	..	..	..	..	..	..	..	..	..	..	..
133	..	..	..	..	..	..	..	..	..	..	..	..	..	..	..	..	..	..	..

4.1.3.4.2. Coding and 3D visualization

The visualization of the modeled fractures plays a key role in the evaluation of the fracture status inside a rock mass. Among the various 3D visualization software packages, ParaView (ParaView website, 2017) was selected because it is open-source and has a multi-platform application for visualizing and analyzing scientific data sets. Among the various file formats accepted by ParaView, the Polygon File Format (.PLY) (Bourke P., 2011) was chosen. This format is used by researchers to describe objects in 3D models in a code that defines points, lines, polygons, etc. In this case study, the objects being visualized were the planes and surfaces of fractures and the volumetric boundary of the bench, see an example in Figure 24.

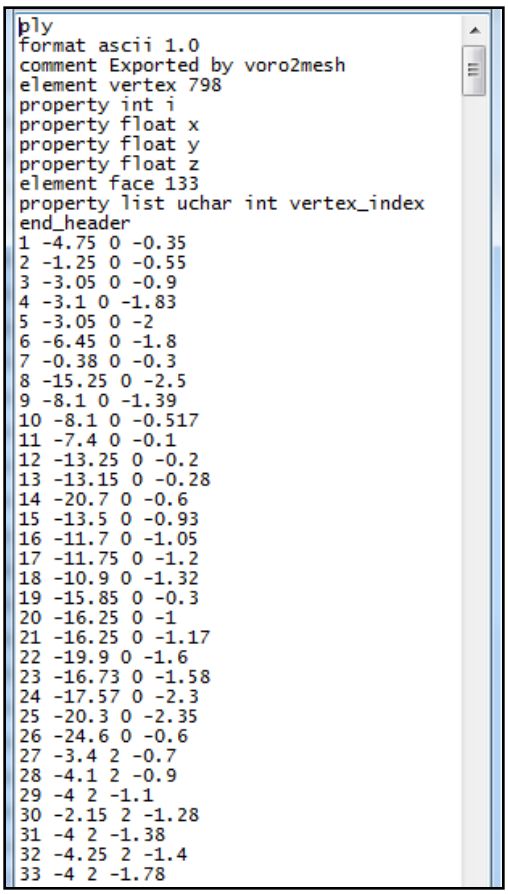

Figure 24: A screenshot showing a part of the (.PLY) format for the coding of the modeled planes of fractures from FISA formulation.

The vertices computed by FITT and FISA formulations were coded to describe the fractures planes and surfaces. In this case study, the modeled fracture planes, obtained from FISA, were included in one file of (.PLY), whilst, the modeled fracture surfaces, obtained from FITT, were included in a separate file. In addition, the geometry of the surveyed bench (25.0 m x 6.0 m x 2.5 m) was also coded to visualize the bench boundaries, jointly with the fractures.

The modeled fracture surfaces (FITT) were coded and visualized keeping the same colors used in the interpretations (Figure 25). The gray color was given to all the modeled fracture planes (FISA). ParaView enables the user to freely turn the whole body of objects in different orientations and to temporarily remove objects so as to clearly study any other objects; for instance, removing the modeled horizontal fracture planes allows a better visualization of the geometric features of the modeled vertical fracture surfaces (Figure 26). The framework of the research methodology in this section is summarized in a process chart (Figure 27).

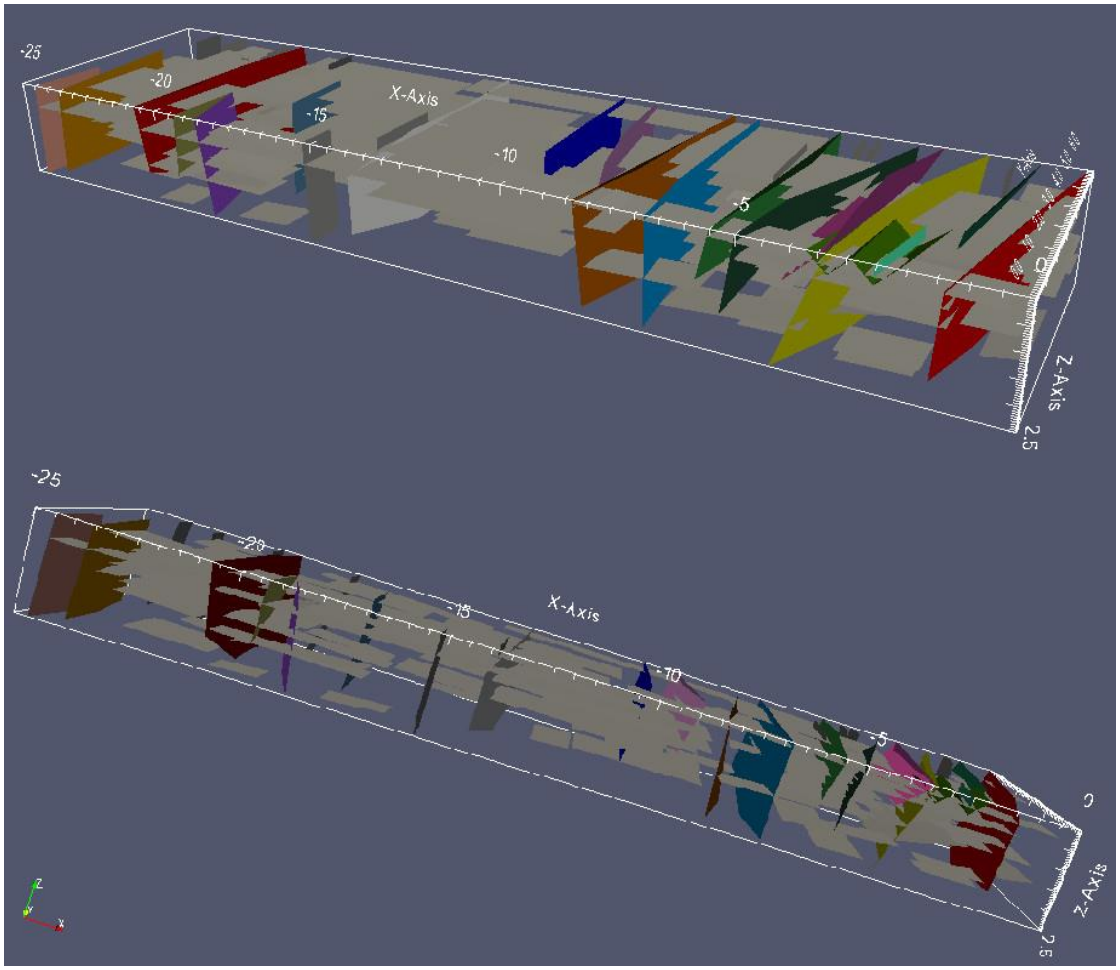

Figure 25: Screenshots, from ParaView, show the visualized 3D fractures model (FISA and FITT) in different orientations.

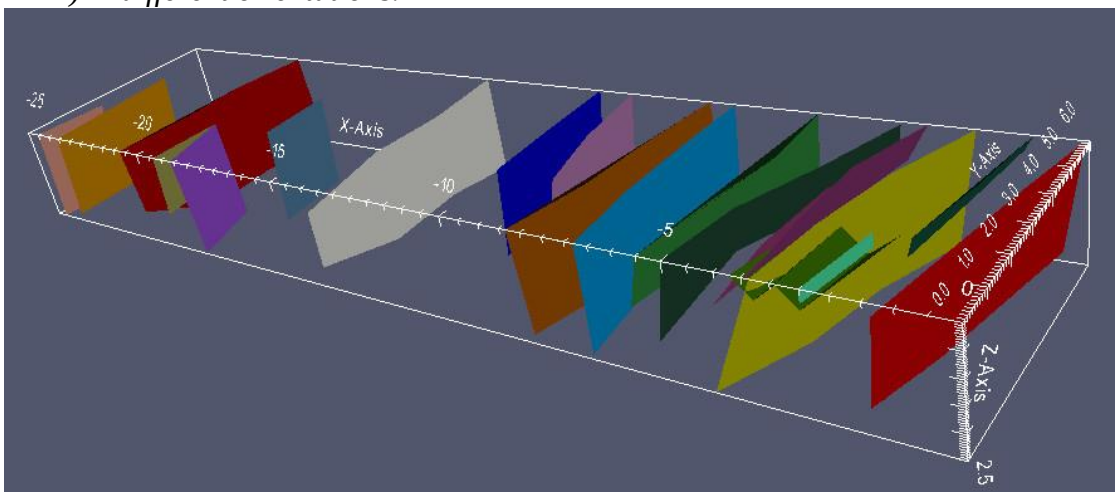

Figure 26: A screenshot, from ParaView, shows the visualized vertical fracture surfaces (FITT), filtering the fractures of FISA.

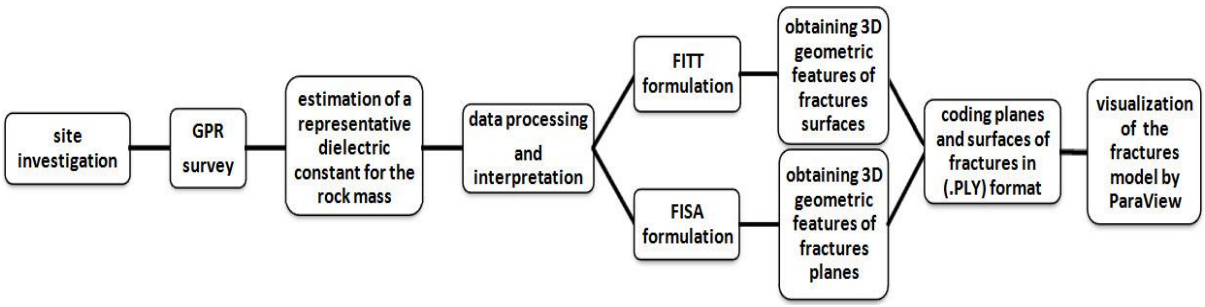

Figure 27: The framework of the research methodology of Section 4.1.

4.1.4. Analysis of results

4.1.4.1. Fracture classifications

The classical method to present and classify rock mass discontinuities is through a stereographic projection. Such graphical method allows to represent fractures and classify the fracture systems in the rock mass into sets according to their geospatial orientations (dip and dip direction). All the detected fracture traces were represented in a stereographic projection of lower hemisphere, using the Schmidt method of equal area (Figure 28a). The geospatial data used in this representation were (γ, δ) of the fracture traces. A discrimination analysis, based on the variation in plunge allowed to classify the sets in three groups. The first group was varying in plunge from 0.0° to 16.0°, the second group was varying in plunge from 32.0° to 48.0° and the third one was varying in plunge from 60.0° to 90.0° (Figure 28b). The horizontal and sub-horizontal fracture traces (set 1) were predominant by 62.0%, whilst the vertical and sub-vertical fracture traces (set 3) existed by 33.0%. A small percentage of 5.0 % (set 2) had an intermediate inclination.

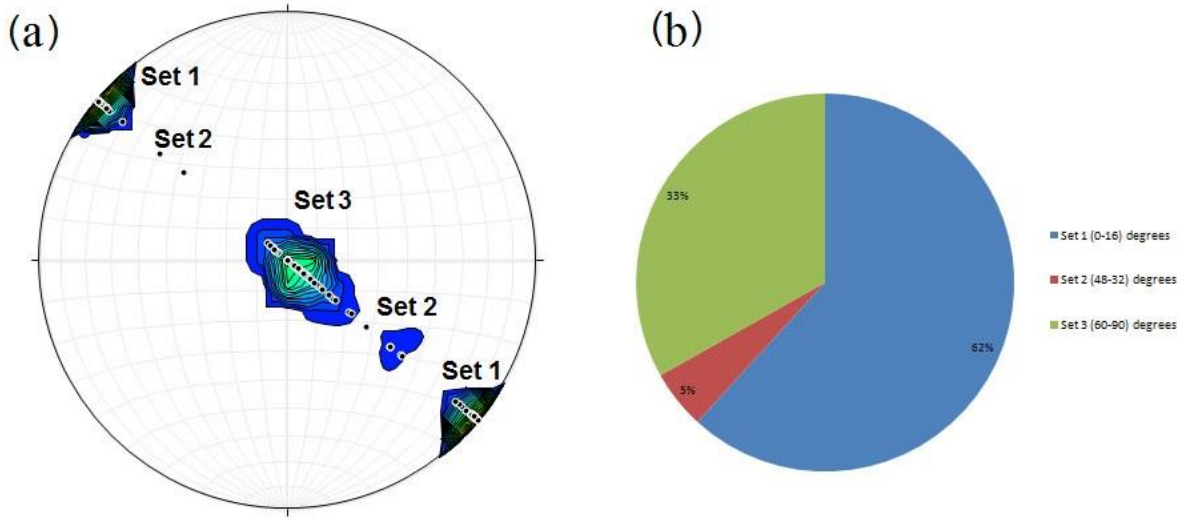

Figure 28: Graphical representation of the whole detected fracture traces through a stereographic projection (a) and through a discrimination analysis in a pie chart (b).

The mean trace length was considered as a character of fracture sets (Sonntag et al., 2012; Zeeb et al., 2013). The three sets of fracture traces were characterized by a mean trace length: set 1 had a mean trace length of 2.76 m, set 2 of 0.86 m and set 3 of 1.82 m. Thus, the analysis of fracture trace lengths may be considered as a kind of geologic validation to the GPR interpretations of fracture reflections.

Spacing between discontinuities is a characteristic of each fracture set (Priest and Hudson, 1976). Since the proposed fracture modeling formulations identify the fractures in 3D space, spacing can be estimated with additional geometric formulations. However, spacing was not estimated in the presented case study. The high intensity of horizontal fractures is the main reason for being this bench completely non-mineable, since it works against extracting commercial-size blocks.

4.1.4.2. A comparison with the traditional manual method

The manual survey method is the traditional method to characterize fracture orientations from rock faces (ISRM, 1978; Priest and Hudson, 1981). The manual method was applied to the out-cropping vertical fracture traces in the bench face. It led to measuring, through a digital inclinometer, the plunges of 25 vertical and sub-vertical fracture traces, since the bench face was vertical and flat. This manual survey was carried out to compare its result with the orientations of the modeled fracture surfaces (FITT). This comparison was used as a possible validation for the proposed approach, following (Assali et al., 2014; Fisher et al., 2014; Park and West, 2002). The comparison between the modeled horizontal fracture planes (FISA) and

the traditional manual method was not considered, since few horizontal fracture traces outcropped in the bench face.

The comparison was carried out through a graphical representation of fracture orientations in a stereographic projection of lower hemisphere, using the Schmidt method of equal area. The orientations of the modeled 22 vertical fracture surfaces are represented in Figure 29a. The stereograph shows that there were two sets of vertical fractures, being Set 1 the predominant one. The mean direction of these data was 124.0° with a maximum frequency of 59.09 %; the direction of Set 1 varied from 112.0° to 135.0°, while the direction of Set 2 varied from 292.0° to 307.0° (Figure 29b).

The stereographic representation of the manual method data (Figure 30a) demonstrated that the manual method data had a behavior almost similar to the modeled fracture surfaces; however, the differentiation between the fracture sets was not as clear as in (Figure 29a). The mean direction was 130.0° with a maximum frequency of 60.0 % (Figure 30b) which was almost close to the mean direction and the maximum frequency of the modeled vertical fractures. It is worth mentioning that the GPR survey, followed by modeling, is able to characterize the orientations of hidden or outcropping fracture surfaces, whilst the traditional method is limited to characterizing the orientations of outcropping fracture traces in a rock surface.

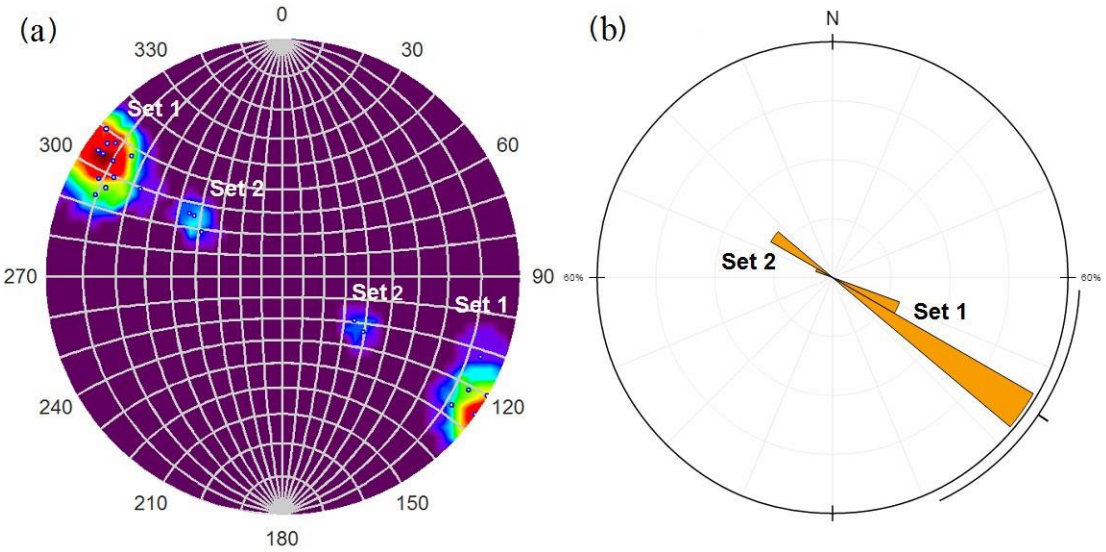

Figure 29: Graphical representation of the orientations of the modeled vertical fracture surfaces in a stereographic projection (a) and in a rose diagram (b).

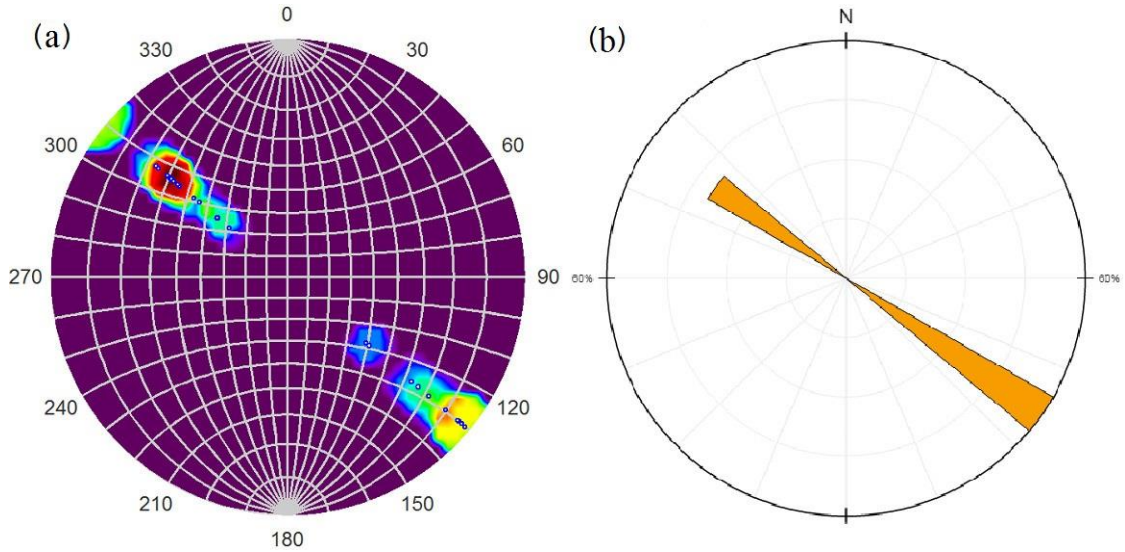

Figure 30: Graphical representation of the data obtained by the manual method in a stereographic projection (a) and in a rose diagram (b).

4.1.4.3. A comparison with a geostatistical mapping of out-cropping fractures

An area of 25.0 m long (x-axis) and 11.0 m wide (y-axis) was considered for a comparison between the out-cropping fractures in this area and the detected fractures by GPR, hence the four radargrams (F01, F02, F03, F04) were located inside this area. The survey line of F01 was the first considered line in x-axis followed by 11 parallel survey lines with a spacing of 1.0 m. Surveying the locations of the out-cropping fractures on the bench surface was carried out by a property in the used GPR unit which allows recording a mark over a point on a survey line. While moving the GPR cart along a survey line, the surveyor can put on the operating system a mark on the radargram once the cart moves over an outcropping fracture. These marks appear in the x-axis of the radargrams and help the data interpretation. In this comparison study, the out-cropping sub-vertical fractures in the bench face were marked to map the intensity of the out-cropping fractures in a relatively large area of the bench surface and to compare the outcropping intensity of fractures with what is hidden in the interior body of the rock mass.

The coordinates of each recorded mark, of the out-cropping sub-vertical fractures, were picked out from the x axis of the 12 radargrams. It should be mentioned that some out-cropping sub-vertical fractures were not recorded as marks due to human errors, however, majority of the out-cropping sub-vertical fractures were recorded. The picked marks were graphically represented in such a way that focused intensity of out-cropping fractures from parallel radargrams in centres of 1.0 m^2 confined surface area (Figure 31a). In Figure 31, the x (m) axis

is the one parallel to the bench face. The centre of each 1.0 m^2 was described by a 3D coordinate of (x, y, z), where z was the number of marks within the 1.0 m^2. A data set of coordinates (Figure 31b) for the tested area were inserted in Surfer^{TM} software package and then interpolated by Ordinary Kriging technique. Kriging is an interpolation method used for generating maps on a grid of spaced data.

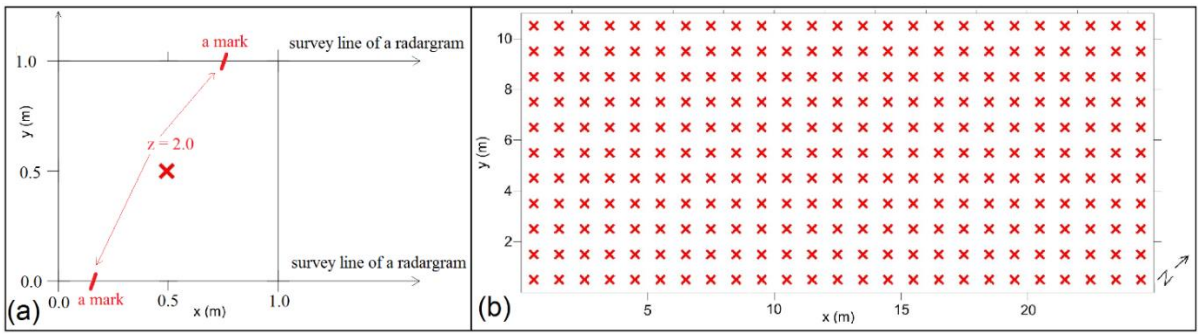

Figure 31: Graphical illustration of how the GPR survey marks of the out-cropping sub-vertical fractures were numerically linked to a centre of 1.0 m^2 confined surface area (a) and the distribution of the resulting data set (b).

The interpolation was performed by variogram that provides a description of how data are spatial depended (auto-correlated) with distance (Wackernagel, 2003). The semi variogram analysis of data and the model are shown in Figure 32 whilst the values of the experimental variogram and the parameters of the variogram model are given in Table 8 and Table 9 respectively.

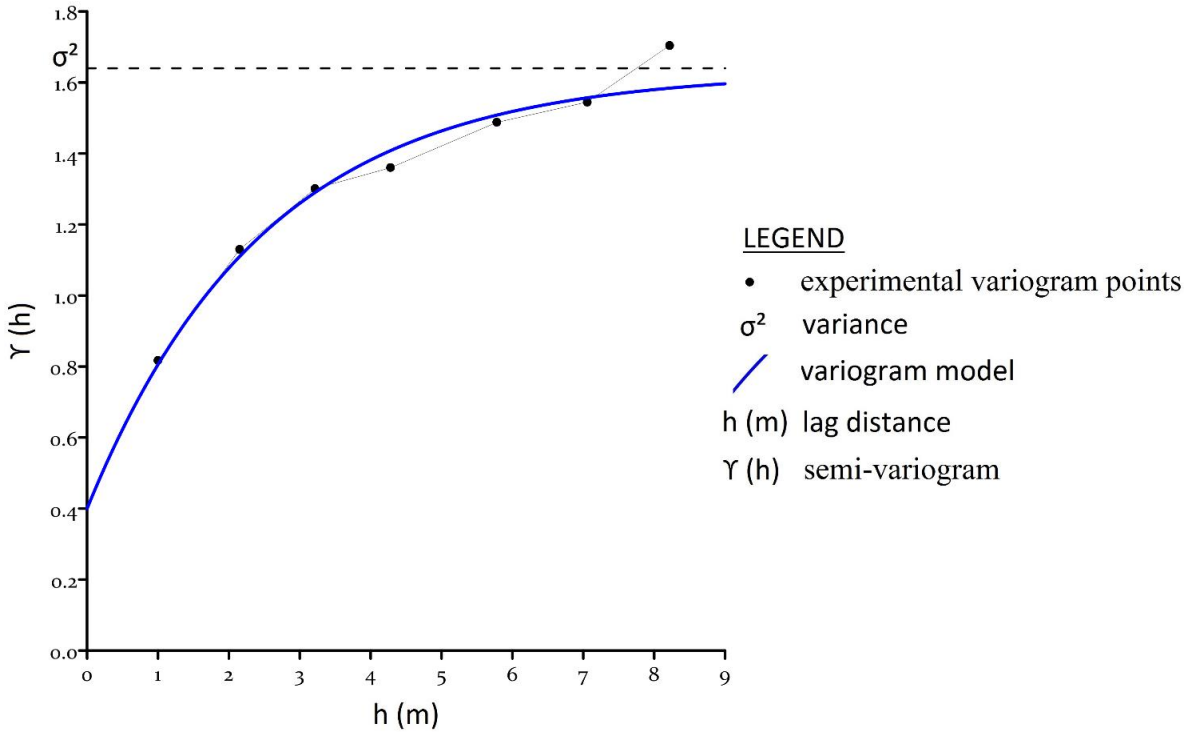

Figure 32: Semi-variogram analysis conducted on the data set.

Table 8: Values of the experimental variogram.

h (m)	γ (h)	number of pairs
1.00	0.82	514
2.15	1.13	1370
3.21	1.30	2444
4.28	1.36	1808
5.78	1.49	2468
7.06	1.54	2598
8.22	1.70	2204

Table 9: Parameters of the variogram model.

variogram structure		
nugget effect	exponential model	
	c - sill	a - range
0.40	1.23	2.50

The estimation standard deviation map and the resulting contour map of the out-cropping fracture intensity in the tested area are presented in Figure 33a and Figure 33b respectively. The contour map shows that the west zone was more fractured than the east zone. In particular, the white zone in the contour map was the zone free of out-cropping sub-vertical fractures, referred by black ellipses in Figure 33b. This zone may be preliminary considered as a fresh

rock by the eye-observation, when what inside the rock mass body is unknown. A check of the GPR results in the white zones was performed. The results showed that the white zone, however it was the freest zone of out-cropping sub-vertical fractures, was characterized by sub-horizontal fractures inside the rock body (see, for example, F02 and F04 in Figure 21).

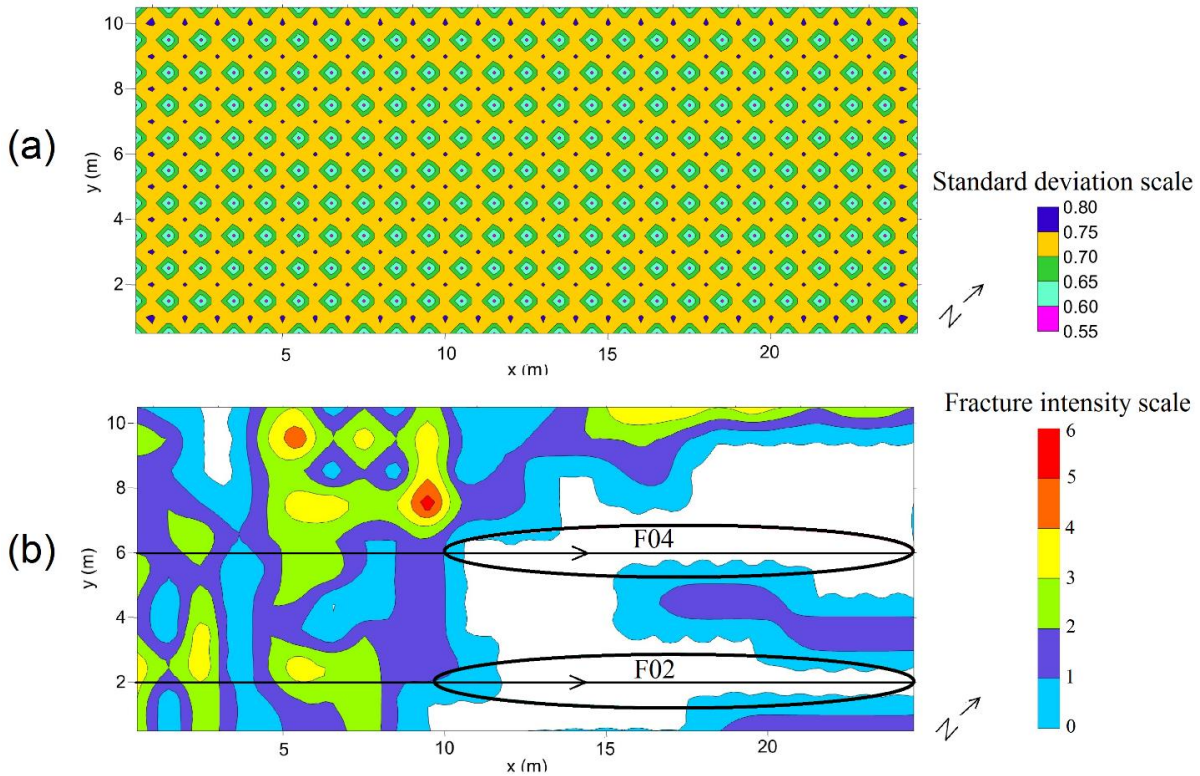

Figure 33: The map of the standard deviation of the Kriging estimation (a) with the resulting Kriging contour map of the estimated fracture intensity (b).

4.1.5. Evaluation-based fracture index

For the purpose of pre-exploitation evaluation, a method for classifying the rock mass into volumetric zones, based on the amount of fractures, is presented. An evaluation-based fracture index for the bench of the case study was obtained through a distribution statistical analysis of the detected fractures inside the bench. The bench was divided, parallel to the bench surface, into five regions with equal intervals of 0.5 m (Table 10), since the maximum penetration depth is 2.5 m. For each region, the number of the detected vertical and horizontal fracture traces was determined from the radargrams. When a fracture trace exists in a region, this region takes a load of "1" representing a fracture trace. In case a fracture trace extends in several regions, each region takes a load of "1". Thus, each region has a certain integer load of fractures for each radargram.

Table 10: Identification of the depth regions. Each region is identified by a subsurface depth, where 0.0 m refers to the surface of the bench.

depth region	subsurface depth (from-to)
region 1	0.0 - 0.5 m
region 2	0.5 - 1.0 m
region 3	1.0 - 1.5 m
region 4	1.5 - 2.0 m
region 5	2.0 - 2.5 m

The histograms of the load of vertical and horizontal fracture traces in each depth region enabled to study the fracture distribution behavior within the depth regions (Figure 34). With regard to the vertical fractures (Figure 34a), region 1 was the most fractured one in all the radargrams and the frequency decreases with the depth increase. Radargram F03 had the lowest frequency of the vertical fractures over the majority of depth regions, whilst radargram F02 had an opposite behavior. Regarding the general trend, the fracture frequency decreases gradually with the increase of depth in all the radargrams.

On the other hand, the histogram of the horizontal fracture frequency (Figure 34b) shows that the fracture frequency, through all the radargrams, mostly increases gradually with the depth increase up to reaching a changing point in the third region and then it decreases dramatically with the depth increase. Radargram F03 had the highest frequency in the first three depth regions, and interestingly, the horizontal fractures in Radargram F03 disappeared in region 4. Behaviors of the normal distribution of fracture traces are clear in radargrams F02 and F04.

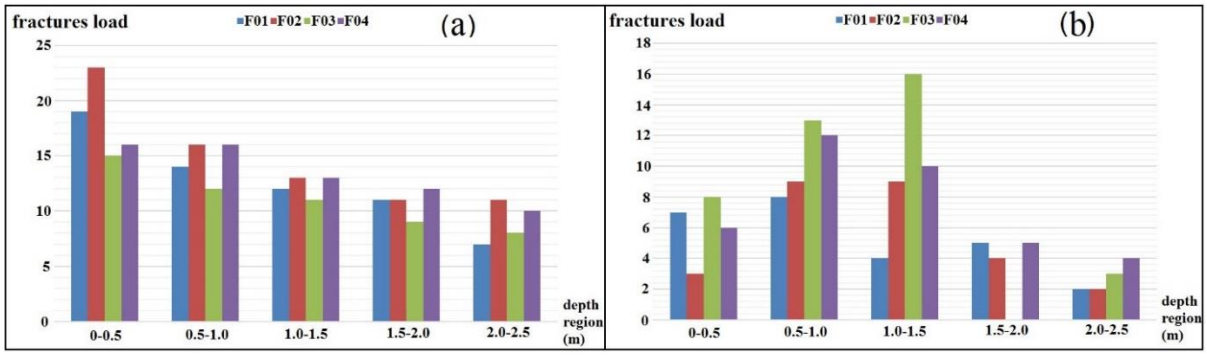

Figure 34: Graphical representation of the fractures load of vertical fractures (a) and horizontal fractures (b) inside the depth regions through the radargrams.

In order to study the fracture distribution behavior in the bulk volume of the bench, the total load of horizontal, vertical and all fractures, for each depth region, through the four radargrams, is graphically presented by the histogram in Figure 35. This proved that the bulk volume of

regions 4 and 5 (named as bulk volume 1) had a lower fractures load than the bulk volume of the remaining regions (named as bulk volume 2).

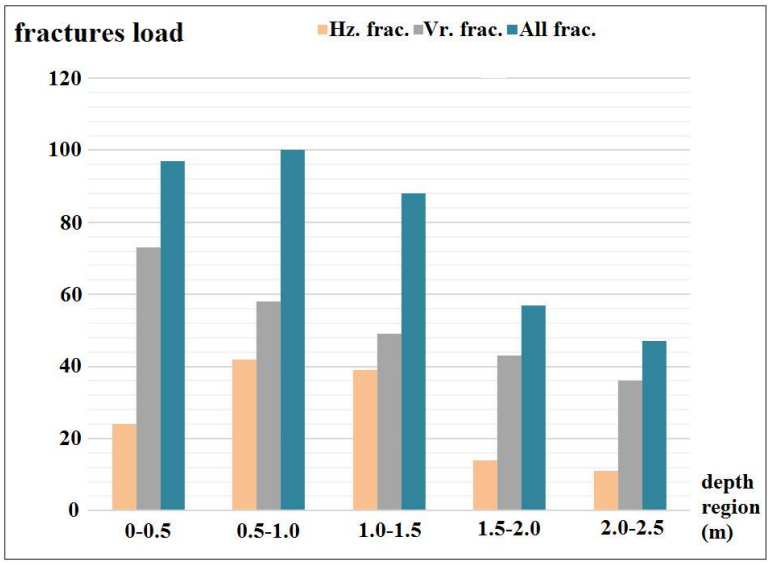

Figure 35: Graphical representation of the total load of fractures within the depth regions.

For a more detailed classification of volumetric zones, it was assumed that the load of fractures in a radargram was the same in a volumetric zone clipped by two imaginary planes, parallel to the vertical cross-section of radargrams. The first imaginary plane was spaced, apart from a radargram, half the interval between radargrams (1.0 m) in the +Y direction, whilst the second one was in the -Y direction.

Accordingly, this led to dividing the bench vertically into four main volumetric zones, and a total of 8 volumetric zones were obtained. Each volumetric zone in bulk volume 1 had dimensions of 25.0 m x 2.0 m x 1.0 m, whilst the volumetric zones in bulk volume 2 had dimensions of 25.0 m x 2.0 m x 1.5 m. Bulk volume 1 and bulk volume 2 were graphically represented by green and turquoise hatching lines respectively in Figure 36. Then, each volumetric zone can be cut into a commercial size of ornamental stone blocks, since the standard dimensions of a commercial block size ranges between 2.0 m x 1.0 m x 0.5 m and 3.0 m x 2.0 m x 1.0 m (United Nations, 1976). The author defines the evaluation-based fracture index (Figure 36) as an index of integer numbers starting from 1 ranking the fractures load in each volumetric zone. In Figure 36, the numbers inside brackets refer to the total fractures load per each volumetric zone. The fracture load in a volumetric zone is the total fracture load of the depth regions inside it. An index of 1 is given to the volumetric zone of the lowest fracture load. The index number increases when the fracture load inside a volumetric zone increases.

In case, several volumetric zones have the same load of fractures, each of them takes the same index.

However, the bench of this case study was non-mineable because of fractures, and the proposed evaluation-based fractures index can be used in the preliminary pre-exploitation planning for mineable benches. Particularly, by adding further technical parameters to the index, in a large surveying area, the index can be used in the objective of production scheduling.

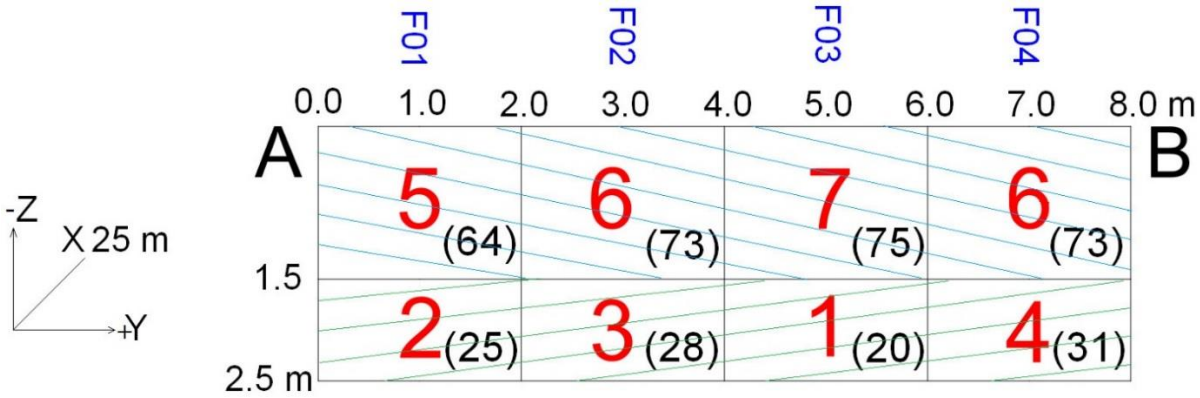

Figure 36: An illustrative sketch shows the evaluation-based fracture index (in red color text) for each volumetric zone. The location of points A and B, in the top view of the bench surface, were graphically introduced in Figure 17.

4.1.6. Conclusions

GPR is a successful tool for detecting fractures, even in wet and highly fractured rock mass conditions. The processed radargrams led to detecting fractures, in a sandstone rock mass, up to a depth of 2.5 m using a 400.0 MHz GPR antenna. Estimation of a representative dielectric constant for a rock mass in-situ is a promising way to optimize the accuracy for detecting fractures at their real subsurface locations. The use of parallel GPR survey lines crossing the main sub-vertical outcropping fractures is necessary for detecting hidden surfaces of fractures. The proposed tracing interpretation technique allowed to successfully model fractures as 3D surfaces which simulate the real geometric behavior of fractures. The modeling assumptions used in FISA scheme may cause some little uncertainties, however results can be improved when all the detected fractures can be modeled following the FITT scheme. A combination of FITT and FISA formulations allowed to build a full 3D model for the existing fracture sets with different orientations. For a better perception of the modeled fractures in the rock mass, the geometric features of the modeled fractures could be coded in Polygon File Format (.PLY) which is readable for a visualization software package (Paraview).

As a validation of the GPR measurements and interpretations, a comparison of the fracture orientation showed that the GPR measurements' results were close to the manual method results. However, the comparison was limited to the dipping angles because of the well-known drawbacks of the manual method.

As a contribution for pre-quarrying evaluation, a frequency analysis of the detected fractures in the radargrams accomplished a 3D evaluation-based fracture index for the bench. This index is a quantitative mapping of fractures; other geologic and economic factors shall be considered in future research to improve this index.

4.2. Implementation of the developed fracture modeling approach

In this section, it is presented an implantation of the developed fracture modeling approach in section 4.1 on a relatively large scale bench. The resulting large-scale fracture model in Section 4.2.1 will be an input for the quarry scale optimization algorithm in Chapter 7. Moreover, in Section 4.2.2, the author presents a further implementation of the developed fracture modeling approach to a commercial-size ornamental stone block which is significant for performing a production optimization model as well, but on a block scale, as will be presented in Chapter 6.

4.2.1. Case study site: a large scale area of a bench in a limestone quarry

4.2.1.1. Site description

This study was carried out in a bench of a limestone quarry located in Poggio Imperiale, Foggia, Italy (Figure 37). The quarried area in this zone belongs to the Apricena quarrying basin which affects the towns of Apricena, Poggio Imperiale and Lesina. The Apricena quarrying basin covers over 24.1 km^2 and is the largest mining area in the Apulian region of Italy. The limestone deposit in this quarrying basin consists of successions that are characterized by the prevalence of terms used for the main type of stone quarried from each of them: "Fiorito Succession", "Biancone Succession" and "Serpeggiante Succession". The limestone deposit in the bench under study is fine and ultra-fine-grained beige-white micritic limestone which belongs to "Fiorito Succession" (Reina and Loi, 2015).

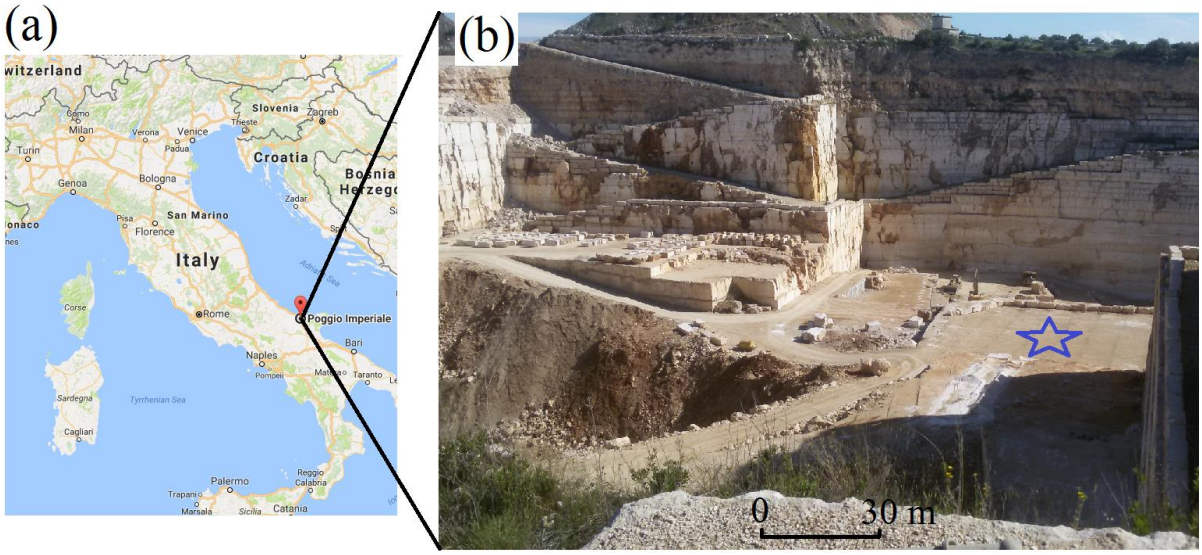

Figure 37: (a) The location of Poggio Imperiale in the map of Italy (Google Maps), (b) a panoramic view of the quarry; the blue star refers to the surface of the bench under study.

The geo-coordinates of the bench center under study correspond to a latitude of 41° 48′ 18.1″ N, a longitude of 15° 22′ 28.7″ E and a height of 95.0 m. It could be observed by the naked eyes that the rock mass of the bench was characterized by two sub-vertical sets of fractures, named Set 1 and Set 2 (Figure 38). Set 1 refers to the fractures that propagate parallel to the bench face, whereas Set 2 refers to the fractures that propagate in the direction perpendicular to the bench face. As can be seen in Figure 38, the spacing of fractures in Set 1 was quite larger than in Set 2; that made the quarried blocks in this bench had a marketable size. The aperture size of the out-cropping fractures ranged from about 0.2 cm to 3.0 cm. The quarrying method in this quarry varies from a zone to another: using either the drilling and blasting method or the diamond wire cutting method. The quarrying method in the bench under study was the drilling and blasting method. The rock mass stratification could not be optically observed from the bench face, whose height was 2.30 m, due to the chemical blasting effect (black and white substances) on the appearance of the bench face (Figure 38) and the thin-aperture discontinuity between two strata, as shown in the side view of the bench (Figure 39). However, it was clear that the strata in this quarry were stratified parallel to the bench surface. The technical manager of this quarry reported that the quarry targets cutting blocks with surface area (XY plane) as large as possible and due to the variable thickness of strata, any reasonable thickness (Z) of the extracted blocks can be acceptable.

Figure 38: A view of the bench face and highlighting the two sets of fractures.

Figure 39: A left-side view to the bench face where horizontal strata were optically observed (named a, b, c, d, and e).

The bench surface was quite flat and suitable for the GPR survey activities. The rock mass of the bench was slightly wet since the GPR survey was carried out 8 hours after the end of a 10-hour light rain. However, the surface of the bench was dry owing to the sun that came out after the rain. The surveying was carried out on a winter day characterized by a temperature of 14˚C and a relative humidity of 71 %.

4.2.1.2. GPR survey design

A three-dimensional GPR survey grid was designed in a rectangular shape with four vertices named A, B, C, and D as shown in Figure 40. The side AB is the one parallel to the bench face and 3.0 m far from the bench face since a major part of the neglected area within these 3.0 m was full of stone debris. The bearing of the side AB was 345.0° from the North direction. The dimensions of the rectangular grid were measured by a tape of 1.0 cm accuracy and an arithmetical check was performed on the lengths of the diagonals, AC and BD, before the survey, to check that the rectangular shape was geometrically correct. The number of survey lines in the X direction were 14, from F01 to F14, with a spacing of 2.0 m whereas in the Y direction were 21 survey lines, from F15 to F34, with a spacing of 3.0 m. The length of each survey line in the X direction was 27.0 m whereas in the Y direction was 65.0 m. No further survey lines after F34 could be surveyed within the grid in the X direction due to the non-availability of an electrical power supply, in the site, to recharge the GPR system batteries and the surveyors preferred to save the remaining power in the GPR system for another survey in the site.

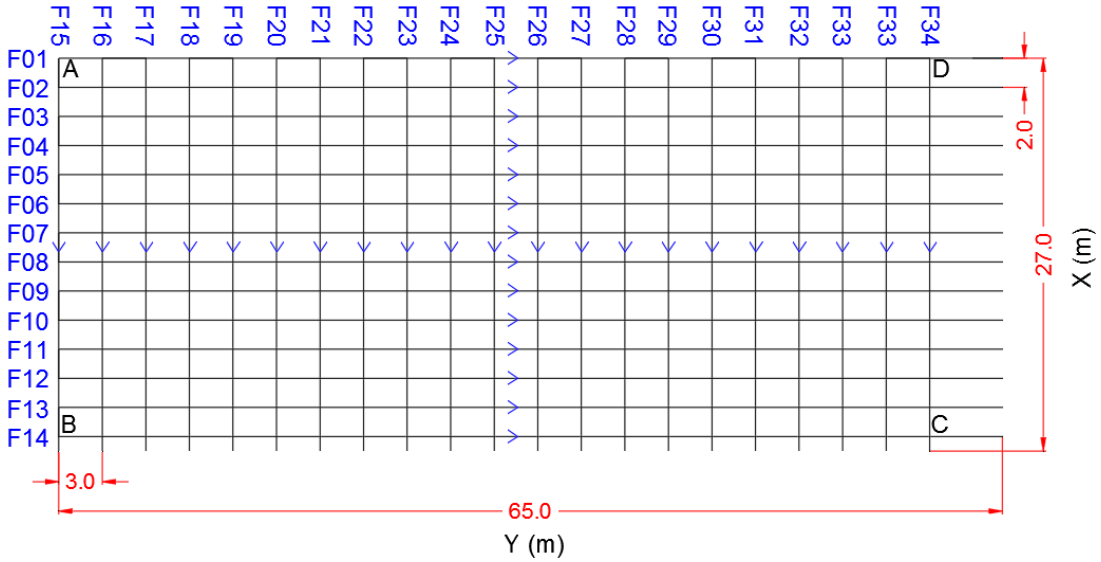

Figure 40: GPR survey design. The blue arrows refer to the direction of the survey lines.

A GPR instrument of a four-wheel mounted dual frequency antenna (250.0 and 700.0 MHz) was used (Figure 41) to perform the survey on the bench surface. The model of this instrument is Opera Duo, manufactured by IDS GeoRadar Srl. The grid was marked on the surface every one meter, as shown in Figure 41, to ease the correct movement from a survey line to another.

The time taken to plan and survey this area was about 140.0 minutes with the human power of three persons.

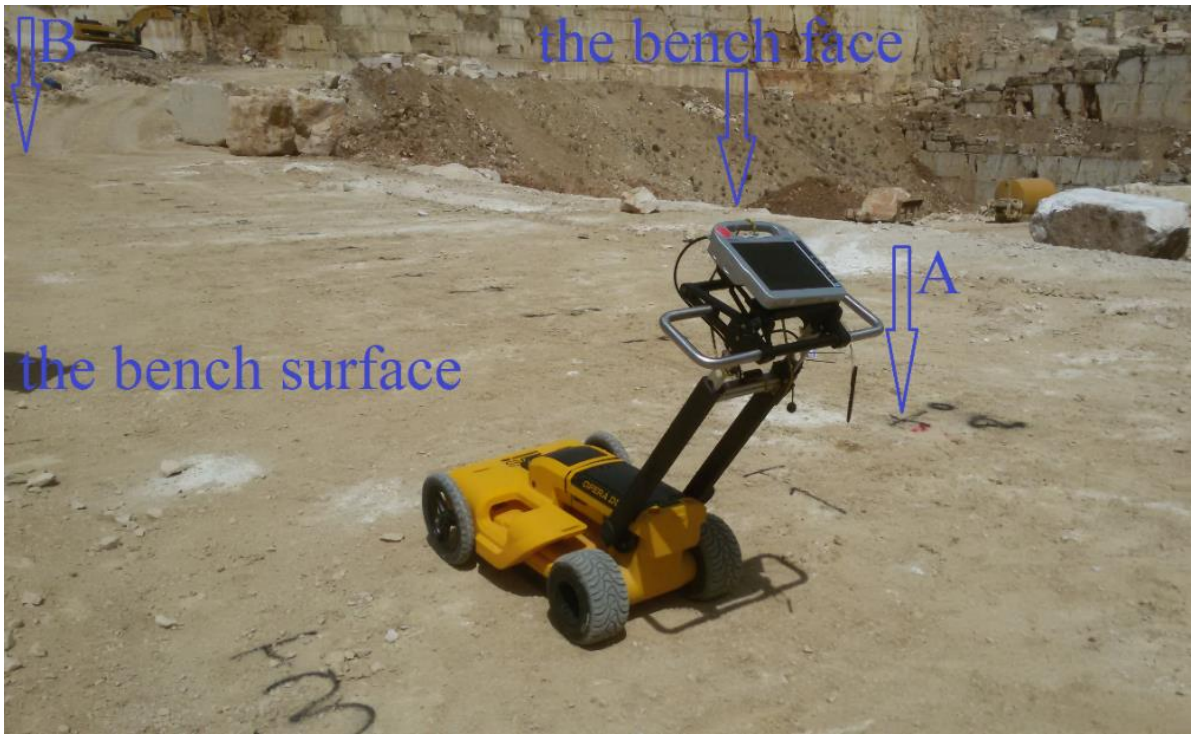

Figure 41: The used GPR unit and indications to the locations of points A and B on the bench surface.

4.2.1.3. Data processing and velocity estimation

The used signal processing software package in this case study was GRED™, produced by IDS GeoRadar Srl. In this case study, only the 700.0 MHz radargrams were considered since this frequency provided enough penetration depth with a higher resolution, compared to the 250.0 MHz radargrams. Standard signal processing functions consist of: adjusting the start time, background removal, vertical bandpass filter, linear and smooth gain functions, and data migration were applied equally to whole the 2D radargrams using the software package GRED™.

The bulk propagation velocity was estimated from the hyperbolic reflections of the sub-vertical fractures in different radargrams from the X and Y directions and within different subsurface depths. A number of 94 hyperbolic reflections were fitted using the fitting hyperbola option provided in the software package GRED™ (Figure 42). It was found that the propagation velocity was highly varied within the rock mass body as referred in Chapter 5. The maximum and minimum propagation velocity were 136.0 Mm/s and 89.0 Mm/s respectively. In this case

study, the average propagation velocity of 110.0 Mm/s was considered. Consequently, the estimated bulk dielectric constant of the limestone rock mass of the bench was 7.4. This estimated dielectric constant value is coherent with expectations, giving that, from bibliography data, the dielectric constant of limestone, in dry conditions, should range from 4.0 to 8.0, whilst in wet conditions it should range from 6.0 to 15.0 (Cassidy, 2009). Using the estimated value of propagation velocity, the double travel time was converted into true depth in the 34 radargrams giving a maximum penetration depth of 3.95 m in the radargrams of 700.0 MHz.

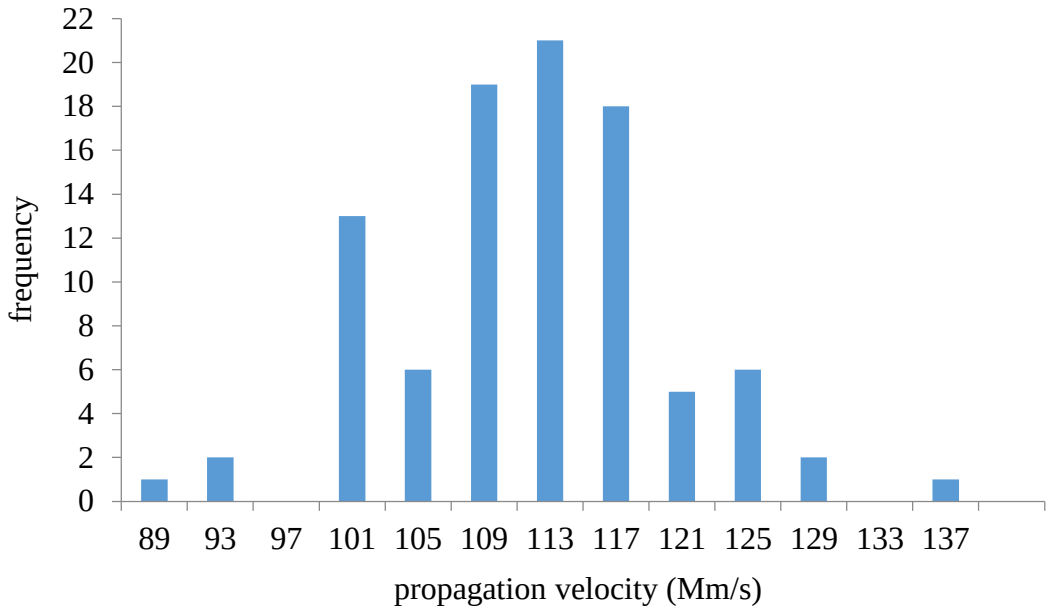

Figure 42: histogram of the propagation velocities measured from the fitting hyperbola method. The propagation velocities in the X axis of the chart were plotted within a bin of 4 Mm/s.

4.2.1.4. Interpretations and modeling

The surveyed area of the bench was divided into volumes in a relation to the radargrams in the X and Y directions (Table 11). The fractures in each volume were interpreted and modeled separately. Then, the fractures were modeled in the connections between the volumes as well. See Appendix A for details. It is worth mentioning that the migrated reflections of the air wave due to antenna bumping were noticed and excluded from the interpretations.

Table 11: The interpretaion volumes.

volume	radargrams	direction
1	F01-F02-F03-F04	Y
2	F05-F06-F07-F08	Y
3	F09-F10-F11-F12	Y
4	F13-F14	Y
5	F15-F16-F17-F18	X
6	F19-F20-F21-F22	X
7	F23-F24-F25-F26	X
8	F27-F28-F29-F30	X
9	F31-F32-F33-F34	X

In all the radargrams, the stratification of the surveyed rock mass body was detected. It was observed that - from the radargrams - the upper and lower surfaces of the detected three rock strata were not flat: wavy surfaces were detected (see an example in Figure 43). However, the average thicknesses of the strata were considered (Table 12).

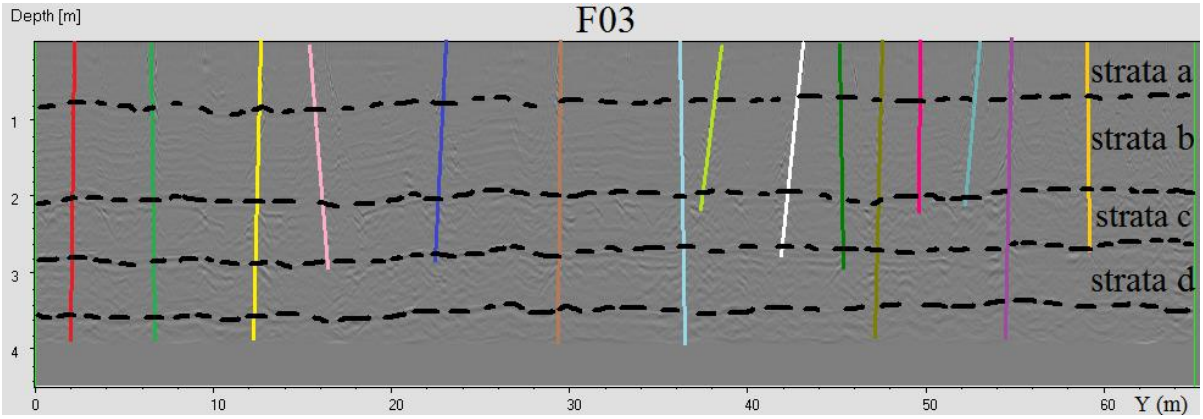

Figure 43: Interpretation of the detected stratification using black dashes.

Table 12: The thickness of the detected rock strata.

rock stratum	from Z(m) – to Z(m)	thickness (m)
stratum a	0.0 m – 0.8 m	0.8 m
stratum b	0.8 m – 2.0 m	1.2 m
stratum c	2.0 m – 2.8 m	0.8 m
stratum d	2.8 m – 3.6 m	0.8 m

The fractures were modeled within a rock mass body with dimensions of 27.0 m X, 65.0 m Y, and 3.95 m Z. The PLY files of the fracture data and the surveyed volume were imported in ParaView for 3D visualization (Figure 44). As shown in Figure 44, the two sets of fractures

are in somehow orthogonally intersected. The fractures detected in the radargrams of the X direction and the Y direction were visualized in the model in yellow and red color respectively.

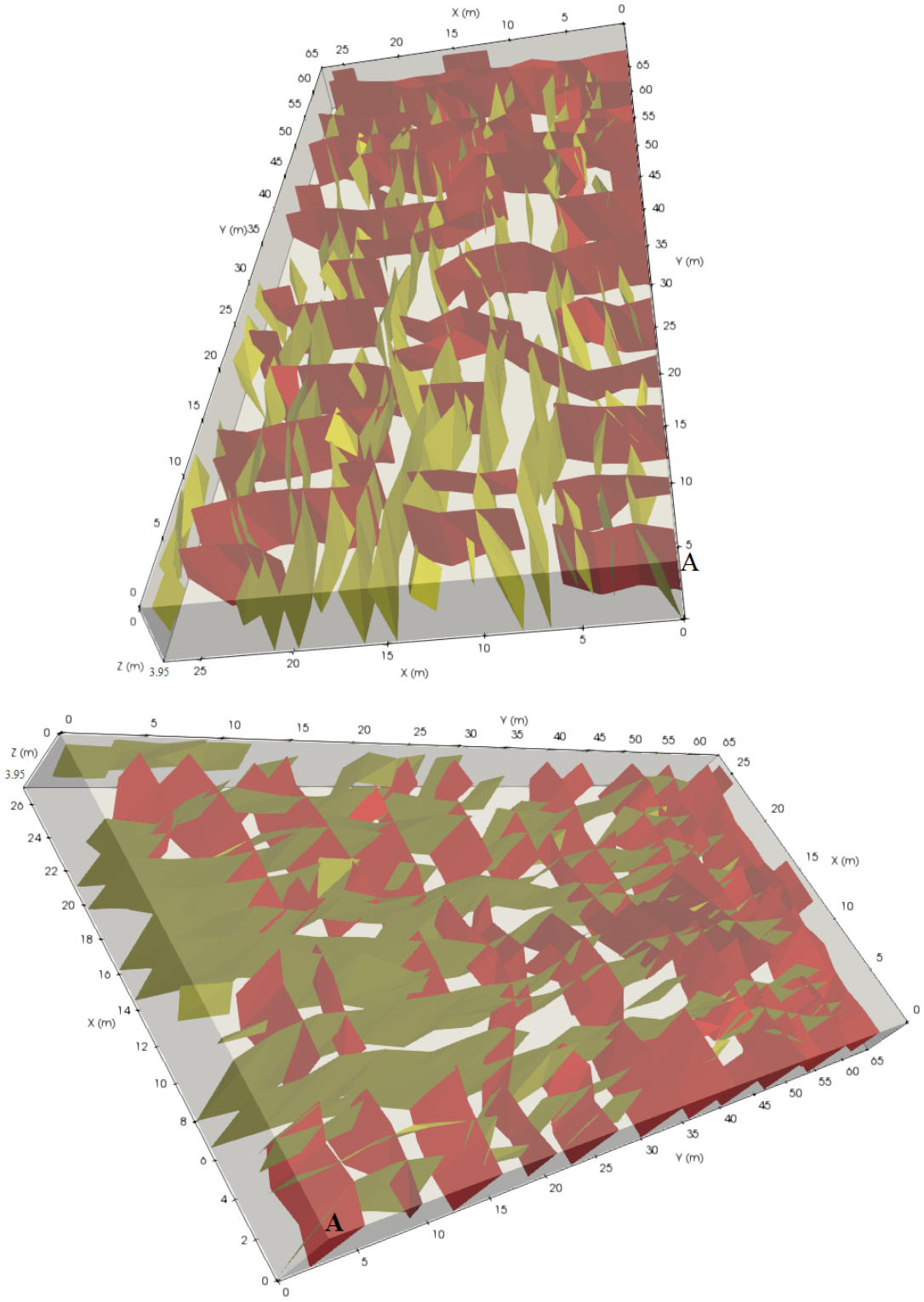

Figure 44: The visualized 3D fracture model in two different orientations. Vertex A of the survey grid is indicated on the model.

4.2.2. Case study site: commercial-size limestone block

4.2.2.1. Background

In addition to the commercial importance of the marketable sizes of ornamental stone blocks, a leading factor that gives a profitable value to the stones is the commercial size of slabs and tiles cut from blocks. Discontinuities adversely affect the quality of ornamental stone blocks and consequently affect the size of slabs and tiles that can be obtained from blocks. The identification of structural weaknesses of ornamental stone blocks before processing is an economic significant task. In order to carry out this quite non-easy task, quarrymen have developed traditional-observation based methods, which entail wrong or non-reliable results. Nowadays, there is an evident lack in the application of invasive non-destructive methods for this task. For instance, current research on the quality evaluation for the building stones industry (Yarahmadi et al., 2017c) can be improved by considering invasive non-destructive detection methods of discontinuities. Deterministic geo-spatial features of discontinuities (e.g. dip angle, dip direction, length) inside the quarried blocks are significant for the decision-making process with reference to: (i) whether or not a block is processable; (ii) the quality ranking of the blocks for commercial marketing; (iii) determining the optimum face for cutting slabs so as to enhance the recovery ratio (see Chapter 6).

Regarding the use of GPR in the scale of ornamental stone blocks, the most noticeable contributions are the works carried out by (Arosio, 2016; Arosio et al., 2012; Rey et al., 2015; Zanzi et al., 2017). In marble and red travertine blocks, the use of 2D radargrams allowed the detection of discontinuities (Rey et al., 2015). In a limestone block, the tomographic interpolation of GPR data allowed the 3D visualization and mapping of the main defects inside the block (Zanzi et al., 2017). In marble and porphyry blocks, detection of discontinuities, cavities and clay inclusions was performed through 2D radargrams and 3D visualization of the GPR data (Arosio et al., 2012). Through simulated GPR data on sandstone blocks, fractures could be characterized in terms of fracture aperture and filling material (Arosio, 2016). This paper presents the application of a three-dimensional deterministic model of discontinuities - based on a GPR survey - to an ornamental stone (limestone) block. According to the authors' best knowledge, it is the first application of this kind.

4.2.2.2. Block description

A fractured block was selected to perform this study. The block under study was extracted - through the drilling and blasting method - from the limestone quarry presented in Section 4.2.1. The dimension of the block was measured through a tape of 1.0 mm accuracy. Each length measurement was repeated several times along each length. The averaged measured dimensions of the block were x = 1.55 m, y = 2.90 m, z = 1.10 m. The upper and lower surfaces and the two surfaces of the lateral sides of the block were sown by means of a cutting machine of blocks processing. Therefore, the upper surface was quite flat and suitable for the GPR survey. The rock medium of the block was slightly wet since the block had been stored in open air and the GPR survey was carried out 8 hours after the end of a 10-hour light rain. However, the upper surface of the block was dry owing to the sun that came out after the rain. The block was lifted from the ground surface over two squared cross-sectional wood supports (Figure 45a). The block was characterized by three out-cropping horizontal (parallel to the upper surface of the block) tiny-size partly-open aperture fractures (Figure 45b and Figure 45c). The aperture size of these fractures was about 1.5-2.0 mm. These planes of fractures cropped-out in the four side surfaces of the block (parallel to the z axis). However, they were hardly visible or almost non visible, to the naked eye, in the non-processed (non-flat) surfaces. These out cropping fractures propagated in the block in a wavy 3D surface with a mean absolute amplitude of about 2.0 cm

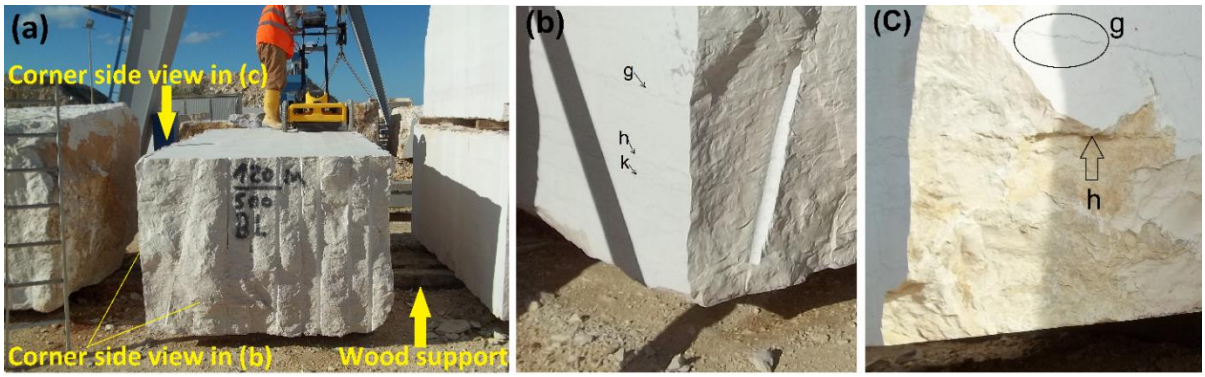

Figure 45: (a) The surveyed block over the wood supports. (b) The corner side view indicated in Figure 45a referring to outcropping planes of partly-open aperture fractures named g, h, and k. (c) The black ellipse refers to a noticeable open aperture part of fracture g and the black arrow refers to a part of the 3D surface of the fracture h.

4.2.2.3. GPR survey and data processing

The same GPR unit used in Section 4.2.1 was used in this study as well. Three lines parallel to the *y*-axis were surveyed by the GPR (Figure 46) on the upper surface of the block. The design of the survey lines optimally considered the dimensions of the GPR instrument. Standard signal processing functions consist of: adjusting the start time, background removal, vertical bandpass filter, linear and smooth gain functions were applied to the three radargrams using the signal processing software package GRED™, produced by IDS GeoRadar Srl. In this study, only the 700.0 MHz radargrams were considered since this frequency provided enough penetration depth with a higher resolution compared to the 250.0 MHz radargrams.

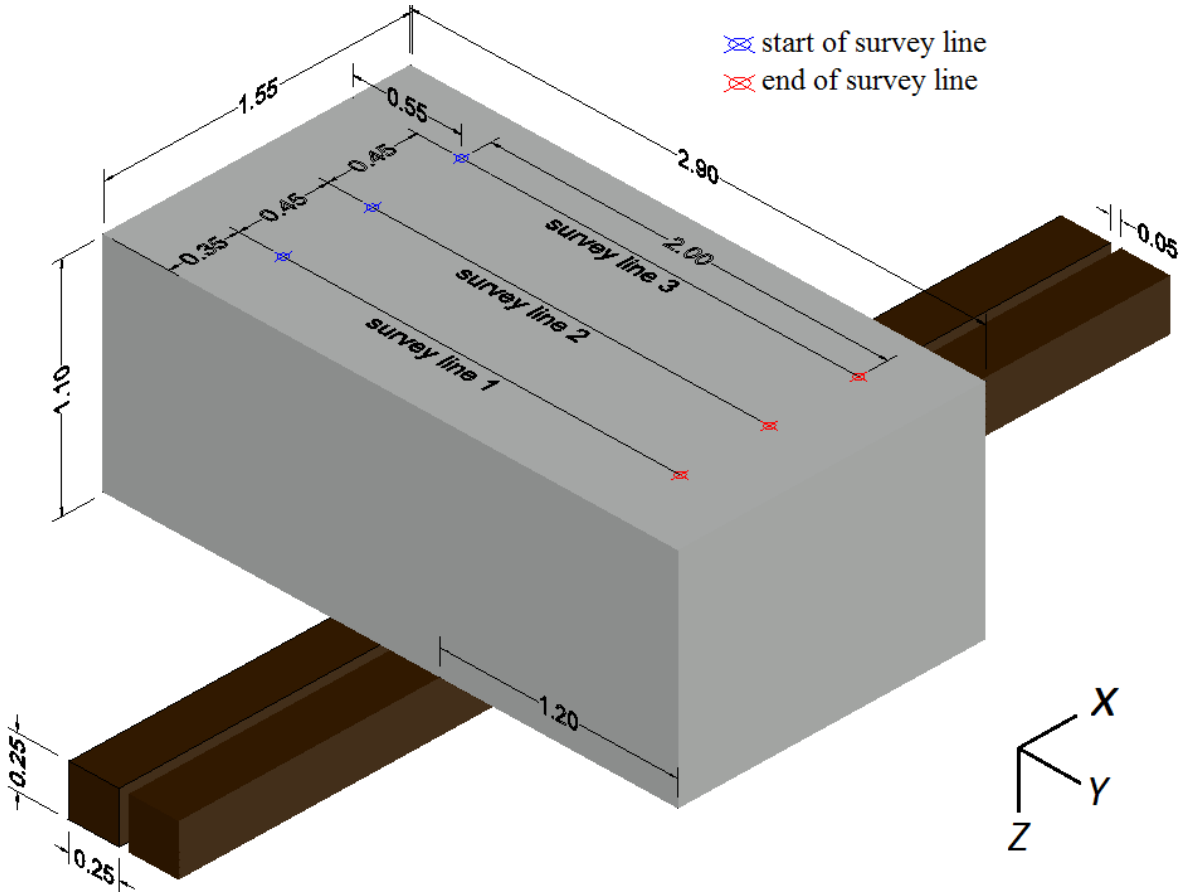

Figure 46: The GPR survey design within a three-dimensional view of the block over the two pieces of wood supports (metric units).

Estimation of a representative dielectric constant of the rock medium was carried out using the "depth of the known reflector" technique. In this study, the depth of the known reflector considered was the lower surface of the block at the depth of 1.10 m (the block dimension).

This surface was detected easily in the radargrams since it is the start of a new air wave. In addition, being this surface lifted over two wood supports, hyperbolic reflections from these two pieces of wood acted as reference as well (see the red circles in Figure 47). The lower surface of the block was detected at an equal double travel time of 20.65 ns in the three radargrams (see the red arrows in Figure 47), giving that the default propagation velocity in the GRED^{TM} software package is 100.0 Mm/s (Megameter/second). The velocity of propagation calculated was 107.0 Mm/s and the relative dielectric constant for this block was 7.9. These values were coherent with expectations, giving that, from bibliography data, the dielectric constant of limestone, in dry conditions, should range from 4.0 to 8.0, whilst in wet conditions it should range from 6.0 to 15.0 (Cassidy, 2009). Using the estimated value of propagation velocity, the double travel time was converted into true depth in the three radargrams. The lower surface of the block was then detected precisely in the radargrams at the true depth of 1.10 m (Figure 48).

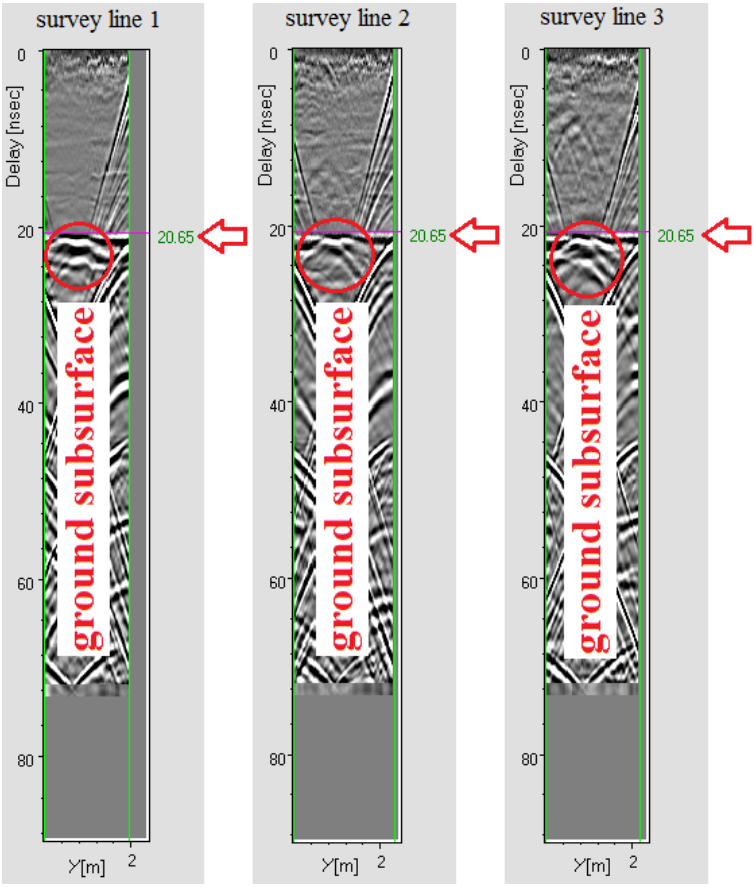

Figure 47: The radargrams of the three survey lines.

4.2.2.4. Interpretations and modeling

Interpretations of the discontinuities detected inside the rock body of the block were performed through the three processed radargrams acquired by the 700.0 MHz frequency antenna (Figure 48). A discontinuity extending in more than one radargram was interpreted by the same color in all radargrams. The out-cropping three fractures (*g*, *h*, and *k*), in Figure 45, in the block were detected in the radargrams. Fracture *k* was partially detected in radargram No. 3. This may have been caused by the reduction in the aperture size of the fracture. Sub-horizontal and sub-vertical planes of discontinuities were detected inside the rock body of the block. However, they were neither out-cropping in the block faces nor visible to the naked eye. Discontinuities were traced within the three radargrams (such as fractures *g* and *h*) or within just two radargrams (such as the yellow and brown fractures)

In addition, hyperbolic reflections were detected inside the rock body. These hyperbolic reflections were interpreted as voids or 3D cavities. One of them (colored in fuchsia) was detected only in radargram No. 3 and did not extend to the rest of the radargrams. The other one (colored in blue) extended in the whole body surveyed with a dipping direction toward the bottom of the block.

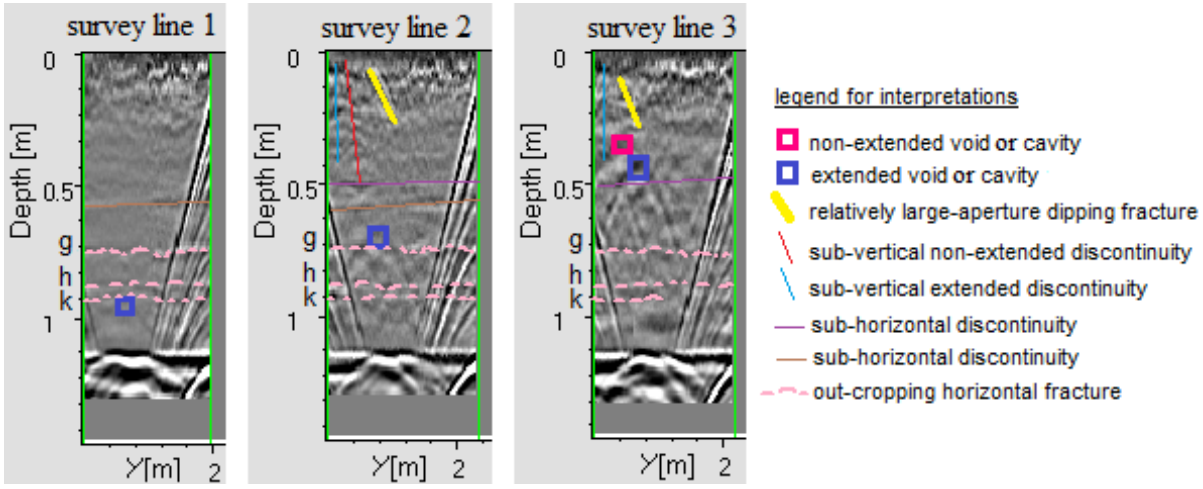

Figure 48: Interpretations of the discontinuities by tracing the extension.

For the interpreted cavities or voids, it was assumed, for simplicity, that they had a square side length cross-section of 8.0 cm. The 3D coordinates of the discontinuities and the tested volume of the block (0.9 m, 2.0 m, and 1.1 m) were coded in the file format (.PLY), readable by the used 3D data visualization software package ParaView. This allowed to visualize the modeled

discontinuities within the surveyed volume of the block in different orientations for a better perception of the results (Figure 49).

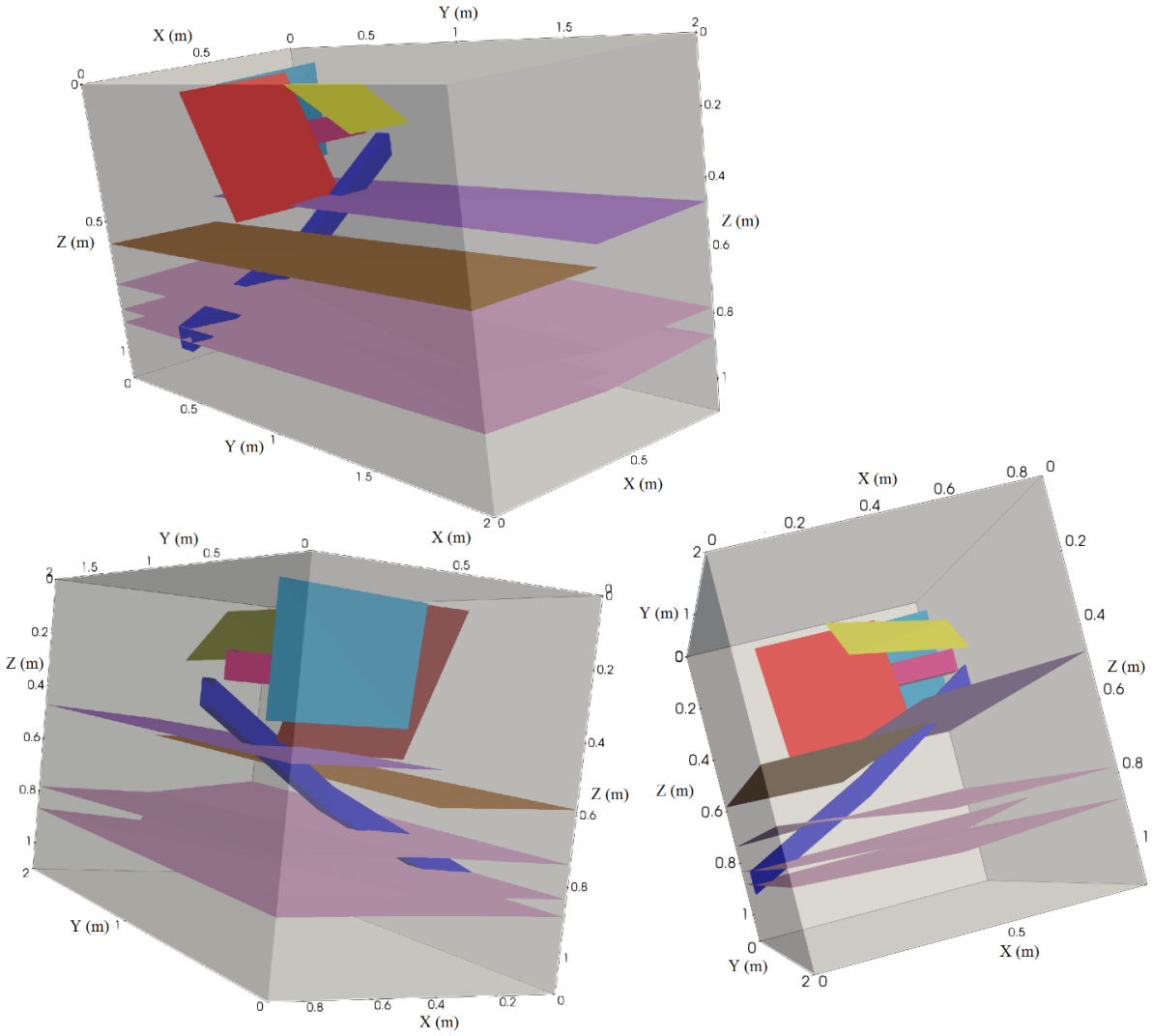

Figure 49: Visualization of the modeled discontinuities, with the same colors used for the interpretations in Figure 48, inside the block in different orientations.

CHAPTER 5

Three-dimensional Modeling of the Dielectric Constant in a Rock Mass

5.1. Introduction and review

For all the fields of GPR applications, estimating the velocity of propagation of electromagnetic waves in a medium or the dielectric constant of a medium is an important parameter for two main purposes: i) to detect subsurface anomalies in a true subsurface depth and migrate diffractions to be focused in their correct geometric shapes (Yelfm, 2007), ii) to estimate hydrological parameters of soil or rock medium such as water content and porosity (Dannowski and Yaramanci, 1999; Gacitúa et al., 2012).

A homogeneous medium, as it could be concrete at a large scale, has a velocity of propagation with little variability in the medium compared to a non-homogeneous medium, such as rock mass. Rock mass is a medium that contains different lithologic strata with inherent planes of structural discontinuities such as fractures, joints, etc. Discontinuities may be filled with different materials such as water, air, etc. so that, the velocity of propagation of electromagnetic waves in a rock mass body is varied and may be in a large scale. This requires to pay more attention in estimating a representative velocity of propagation or bulk dielectric constant for the applications of GPR in a rock mass medium. The purpose of this chapter is to numerically and graphically investigate the variability of the velocity of propagation and the dielectric constant in a rock mass body in real time of surveying. The result of this chapter is significant to improve the deterministic accuracy level of fracture detection and modeling using GPR and in particular for the modeling approach presented in Chapter 4, if considered in future work.

5.1.1. Methods of the propagation velocity estimation

Most common currently that the propagation velocity is estimated by the reflected waves method. There are two commonly used reflected waves acquisition techniques: the Common-Mid Point (CMP) and the Wide Angle Reflection and Refraction (WARR) (Huisman et al., 2003). Examples for CMP and WARR applications can be found in (e.g. Dannowski and Yaramanci, 1999; Tillard and Dubois, 1995) and in (e.g. Dekeyser et al., 2007; Porsani et al., 2006) respectively. In these two acquisition techniques, the survey is carried out over a horizontal reflector where antennas are separated away from each other by a certain amount for each measurement.

A technique based on the reflected waves method - called "known depth to reflector" - is based on a wave reflection from a buried object with a known depth. Then, the velocity of propagation can be estimated by Eq. (2) (ASTM International: D6432-11, 2011). Another technique based on the reflected waves method concerns the reflection coefficient. The amplitude of the reflection from the air to a medium surface compared to the incident amplitude reflection, usually from a metal plate, can be used to determine the bulk dielectric constant of a medium (Hoegh et al., 2015). This technique is common in road or asphalt evaluation taking into consideration several assumptions and limitations (Saarenketo and Scullion, 2000).

The direct waves method is based on the movement of waves from a transmitter to a medium and then to a receiver following a known pathway (transillumination principle). In this method, the transmitter and receiver antennas are placed on the opposite sides of a rock mass through two trenches or boreholes. The thickness of the rock mass between the transmitter and the receiver shall be larger than the wave length to eliminate the effect of the near filed zone (Artagan and Borecký, 2015). The uncertainty in this method is in determining the exact path of GPR signal (Daniels, 2004). The transillumination principle in addition to CMP and WARR are known as variable offset survey methods. It is impossible to perform the variable offset methods through a monostatic GPR antenna, housed in a case with a fixed separation, which currently is the most available one (Greaves et al., 1996).

Since a large portion of GPR activities are performed in a non-homogeneous medium, such as rock mass, the reflected waves method is currently recommended for estimating the velocity of propagation, particularly when the technique of "known depth to reflector" is applicable in-situ, since it gives results in real time, as presented in Sections 4.1.3.2 and 4.2.2.3 . In some cases, a possible solution is to estimate the velocity of propagation or the dielectric constant from intact rocks, in laboratory, by applying the technique of "known depth to reflector" (Aqeel et al., 2013) or through a dielectric capacitive cell (Elshafie and Heggy, 2013; Mukherjee et al., 2010). This solution gives acceptable results only if many samples are representatively collected from the surveyed volume and preserved in the same physical conditions of the GPR surveying time. It is necessary to take into consideration that the physical and mechanical properties of intact rocks, taken from the same surveying area, are generally with variable characteristics even at small scale. It is worth mentioning that using

the values of the dielectric constant and of the velocity of propagation, from published common tables, does not provide trusted values.

For most of cases “depth of known reflector” is inapplicable due to absence of subsurface information. Since most of the current GPR instrument are monostatic and hyperbolic reflections are quite common in radargrams, the author used, in this chapter, a fixed offset survey method for mapping the propagation velocity to investigate to what extent the dielectric constant is variable in a rock mass. An in-situ GPR test was elaborated based on the insertion of steel rods, acting as reflectors, in a rock mass. Then, a mathematical formulation, driven from a hyperbolic reflection model, allowed estimating the variability of the velocity of propagation in radargrams. Consequently, a 3D mapping of the dielectric constant variability in the rock mass was obtained.

5.2. Methodology

5.2.1. Site preparation and GPR data acquisition

The GPR survey was performed in the bench (bench B) of the sandstone quarry, presented in Section 4.1.2. This bench was convenient for performing this study since it was a typical non-homogeneous discontinuous rock mass. Some of the out-cropping sub-vertical fractures which characterized the rock mass nature of this bench can be seen in the bench surface in Figure 50. The GPR instrument, used in this research, consisted of a shielded dual frequency antenna of 200.0 and 600.0 MHz mounted on a cart and linked to a real time data monitor (Figure 50). The GPR unit is manufactured by IDS GeoRadar Srl. A dual frequency antenna saves surveying time, since it allows to survey through two different frequencies within a single scan simultaneously. Moreover, it provides a good compromise between penetration depth and resolution (Rafezi et al., 2015).

Figure 50: A picture taken in the bench surface of the case study shows the shielded dual frequency GPR antenna used in this study.

The GPR test aimed at detecting hyperbolic reflections resulting from buried steel rods at different depths in rock mass medium. The use of buried steel rods, as reflectors, in homogeneous media for GPR tests in laboratory experiments was presented by (e.g. Colla, 1997; Colla et al., 1998; Molyneaux et al., 1995; Qiao et al., 2015; Zhan and Xie, 2009). In this chapter, the author used steel rods buried in a non-homogeneous discontinuous medium (rock mass). These rods were drilling rods used by the drilling machine of blasting boreholes. A perforation of six boreholes was carried out nearly normal to the vertical bench face of the case study. Six rods were completely inserted in the boreholes (Figure 51a). The drilling rods were rigid and have a 3.0 m long hexagonal cross-section with a 1.1 cm circumradius.

The rods were designed to be buried, orthogonally to the bench face, in a diagonal pattern to avoid the limitation of horizontal and vertical resolution; no rods were closely buried in the same horizontal or vertical plane. The horizontal spacing between the first three rods (shallowest rods) was designed to be relatively large (1.0 m) to evaluate the possible existence of variation of the propagation velocity in a large portion of the rock mass. Since these three rods were the nearest to the bench surface, it was expected to be detected in the radargrams of both frequencies, considering the physical aspects of the electromagnetic waves. Using a large spacing between rods in the deep part of the rock body may lead to losing the opportunity to evaluate the propagation velocity in a large portion, since the waves at the deep rods were subjected to attenuation. The deepest three rods (rods 4, 5, and 6) were buried using a smaller spacing in a trial to study the variation of the propagation velocity in a relatively smaller portion of the rock mass. This design was limited also by the maximum area provided by the quarry

owner to perform the in-situ test as well as the availability of the drillers, drilling machines, and amount of drilling rods.

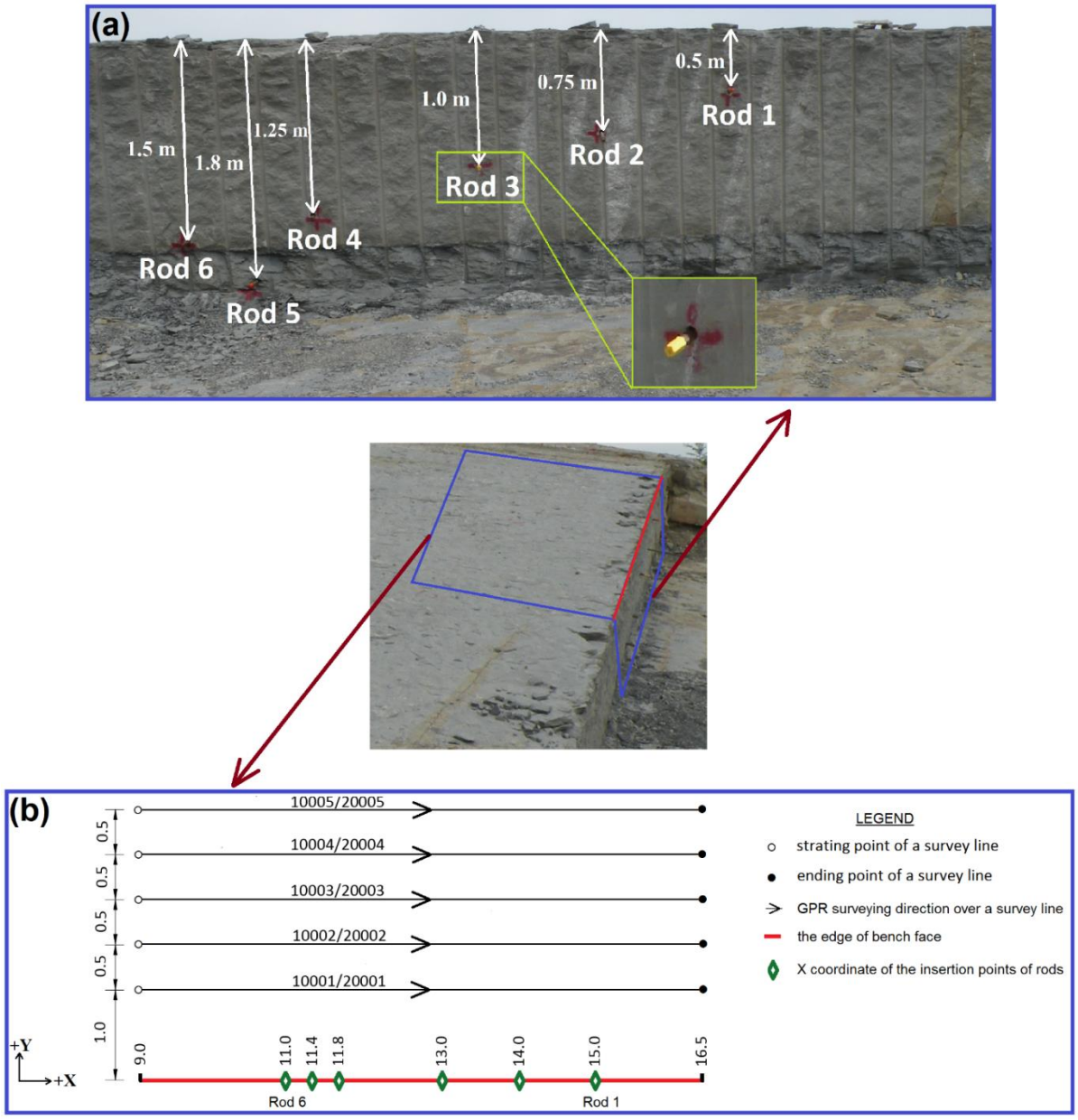

Figure 51: (a) A front view of the bench face showing the insertion depths of the rods from the edge of the bench face. (b) A plan view of the GPR surveying design over the bench surface with indications of the insertion points of the rods (metric units).

After testing the response of the GPR signal in the rock mass of the bench, preliminary acquisition parameters, compromised for the two frequencies, could be estimated. The operating system was set up with a time range of 100 ns, 512 samples/scan, a format of 16 bits/sample, a rate of 100 scans/m, high pass filter 100.0 MHz, low pass filter 1900.0 MHz.

Data acquisition was performed through 5 survey lines over the bench surface, parallel to the vertical bench face, and almost perpendicular to the steel rods. The design of the survey lines is graphically presented in Figure 51b. All radargams were recorded starting at 9.0 m from a reference point in the bench edge to 16.5 m. Each survey line was named with a code formed of 5 digits (e.g. 10001). The first digit refers to the antenna frequency (thus: 1 refers to 600.0 MHz and 2 refers to 200.0 MHz), whilst the last digit refers to the survey line number.

5.2.2. Data processing and interpretation

When a GPR antenna moves in a survey line over a buried pipe-like target, a hyperbolic reflection is obtained due to the conic emission pattern of the electromagnetic waves (Daniels, 2004; Geophysical Survey systems Inc., 2006). The main aim of the signal processing is to clarify the outline shape of the hyperbolic signatures from the steel rods in the radargrams. The radargrams were processed using a signal processing software package (GRED ^{TM}), which is a product of IDS GeoRadar srl.

Firstly, the zero time was adjusted manually. The background noise was eliminated by applying horizontal background removal. A minimum value of 0.0 m and maximum value of 10.0 m were set in the filtering algorithm to remove horizontal components in the X direction. The filtering of frequencies in the vertical direction was performed using the vertical bandpass filters tool. A low frequency bandpass filter of 100.0 MHz, for both the radargrams of 200.0 MHz and 600.0 MHz, was used, whilst high bandpass filters of 1000.0 MHz and 1500.0 MHz were used for the radargrams of 200.0 MHz and 600.0 MHz respectively. Power equalization of the amplitudes on the basis of an automatically estimated linear attenuation was carried out through the linear gain function, followed by an automatic smoothing gain filter. Finally, by selecting a proper color scale and adjusting the display gain, it was possible to spot some lower amplitude regions. After the data processing, the hyperbolic reflections, from the buried steel rods, were visually enhanced (Figure 52). In Figure 52, the depth scale on the left concerns the default velocity of propagation: 100 Megameter/second (Mm/s) for 200.0 MHz radargrams and 84 Mm/s for 600.0 MHz radargrams.

The hyperbolic signatures of the rods 5 and 6, were overlapped in confused status (Figure 52, radargram 20001), but not detected at all in the other radragrams. This behavior could be caused by: (i) small spacing between the deep rods; (ii) drilling deviations of the drill holes due to technical drilling difficulties in the deep part of the rock; (iii) signal attenuation.

Regarding signal attenuation, it was found that the signal of the 200.0 MHz frequency started to attenuate within a depth range between 1.45 m and 1.80 m where rods 5 and 6 were buried while for the signal of the 600.0 MHz frequency, the signal clearly attenuated at a depth of 1.25 m (Figure 53). In Figure 53, the penetration depth presented in the graphs considered the average propagation velocity in the radargrams obtained from the method presented in Section 4.1.3.2. Thus, rods 5 and 6 were located in a zone of attenuation which played a role – might be with another referred reasons - for non-identifying the targets. Not all the hyperbolic reflections of the 6 rods were clearly identified in the radargrams, at least the hyperbolic reflections of rods 1, 2, and 3 could be clearly identified in all radargrams.

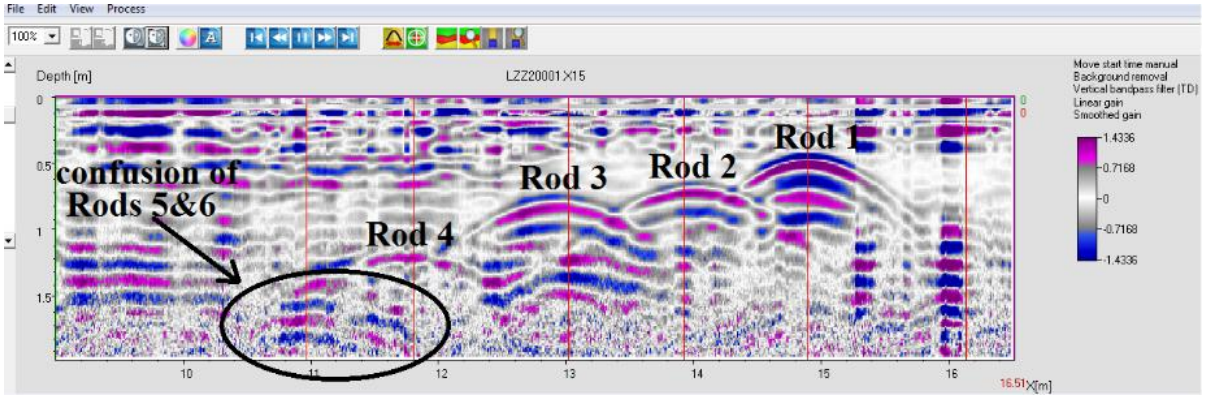

Figure 52: Radargram 20001 after signal processing. The vertical red lines are surveying markers put by the surveyor during the data acquisition. The first marker on the right does not refer to any rod and the marker of rod 5 is lacking.

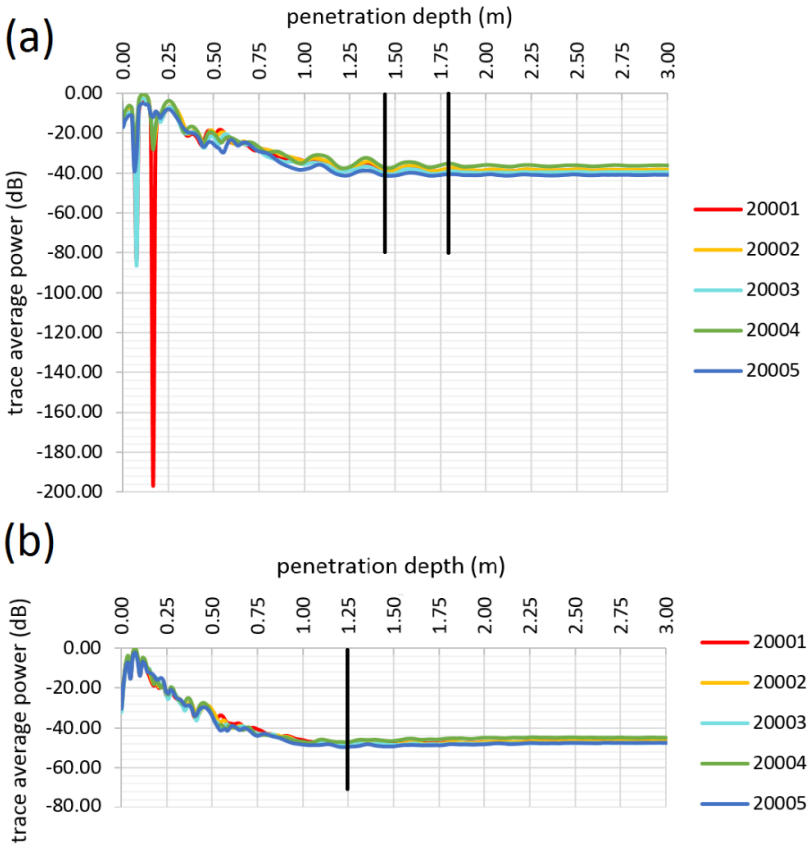

Figure 53: The trace of the average power of the signal within the five radargrams of 200.0 MHz (a) and 600.0 MHz (b) with referring to the depth of the attenuation by vertical black lines.

5.2.3. Reflection model of a buried cylindrical object

The geometric setting of a reflection hyperbola in a radargram is described in Figure 54 and in (Eq. 3). From this geometrical setting, Al-Nuaimy et al., (2000) derived a simple reflection model of a hyperbola, satisfying a three parameter hyperbola equation (Eq. 4). Since this model is valid for a shielded antenna with a fixed separation distance between transmitter and receiver, the velocity of propagation is assumed to be constant in a tiny triangular region. This region is bounded by the separation distance, the pathway of the emitted waves, and the pathway of the received waves.

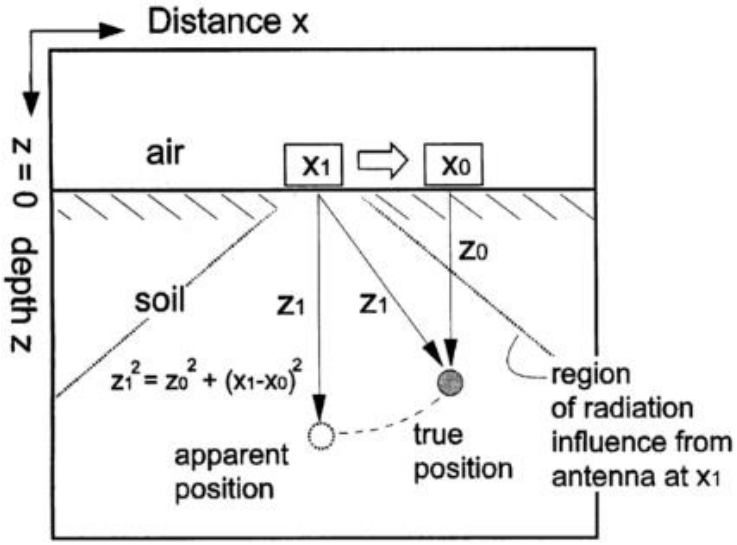

Figure 54: The geometrical setting of an antenna position and a target position that creates a hyperbolic reflection from a point reflector. ($x_\circ, z_\circ$) are the coordinates of the true position of a reflector. (x_1, z_1) are the coordinates of the apparent reflection from the reflector when the antenna position is at x_1, after (Al-Nuaimy et al., 2000).

$$z_1{}^2 = z_\circ{}^2 + (x_1 - x_0)^2 \tag{3}$$

Substituting by $z_1 = \frac{vt_1}{2}$ and $z_\circ = \frac{vt_\circ}{2}$ in Eq. 3 gives:

$$t^2 = t_\circ{}^2 + \frac{4}{v^2}(x - x_\circ)^2 \tag{4}$$

In the model of Eq. 4, the hyperbolic signature is assumed to be from a point reflector, considering that the radius of a reflector (R) is zero. The characterization of the hyperbolic signatures assuming that R = 0 leads to errors (He et al., 2009). When R is considered to be zero (point reflector), it would affect the spread of hyperbola tails caused by a higher value of the velocity of propagation. As a result, incorrect values of the velocity of propagation and the dielectric constant of the medium will be estimated. Subsequently, the effect of considering R on the hyperbolic signature was studied (Figure 55) and a more generalized hyperbolic equation (Eq. 5 and 6) was developed by (Shihab and Al-Nuaimy, 2005).

$$(z_1 + R)^2 = \left(z_\circ + R\right)^2 + (x_1 - x_0)^2 \tag{5}$$

Substituting by $z_1 = \frac{vt_1}{2}$ and $z_\circ = \frac{vt_\circ}{2}$ in Eq. 6 gives:

$$\left(\frac{t_1 + \frac{2R}{v}}{t_\circ + \frac{2R}{v}}\right)^2 - \left(\frac{x_1 - x_0}{\frac{v}{2}t_\circ + R}\right)^2 = 1 \tag{6}$$

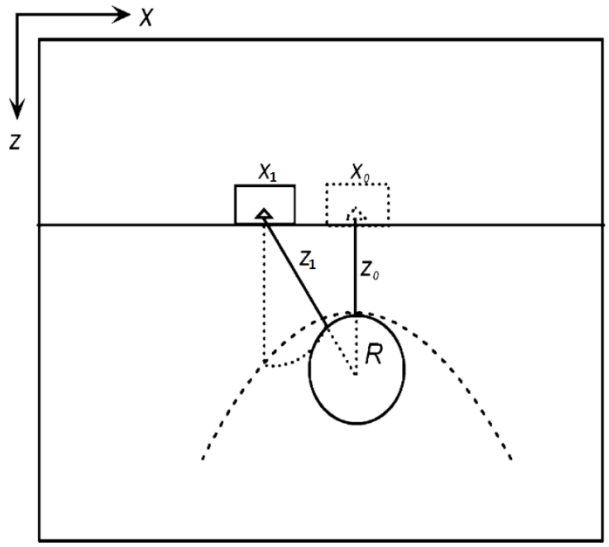

Figure 55: The geometrical setting considering the radius (R) of a cylindrical target, after (Shihab and Al-Nuaimy, 2005).

In this chapter, the hexagonal cross-section of the used rods were assumed to be circular. Therefore, the concept of Eq. 5 was used to estimate the velocity of propagation. It is necessary for the velocity of propagation to be a dependent variable in a side of an equation model. Accordingly, substituting by $z_1 = \frac{vt_1}{2}$ and $z_\circ = \frac{vt_\circ}{2}$ in Eq. 5 and rearranging, in such a way that causes a quadratic function of v gives:

$$\left(\frac{{t_1}^2}{4} - \frac{{t_\circ}^2}{4}\right) v^2 + \left(t_1 R - t_\circ R\right) v - \left(x_1 - x_\circ\right)^2 = 0 \quad (7)$$

Solving Eq. 7, using the quadratic formula, gives two solutions: v_a and v_b (Eq. 8), where the negative one will be neglected. The application of this velocity model is presented in the next section.

$$v_{a,b} = \frac{-t_1 R + t_\circ R \pm \sqrt{\left(t_1 R - t_\circ R\right)^2 + \left({t_1}^2 - {t_\circ}^2\right)\left(x_1 - x_\circ\right)^2}}{\frac{1}{2}\left({t_1}^2 - {t_\circ}^2\right)} \quad (8)$$

5.2.4. Estimation of the velocity of propagation in pathways

Commercial software packages of the GPR signal processing provide a function to fit hyperbolic signatures in radargrams by manually moving the tails of a fitting hyperbola. This function can estimate reliable results when the medium is homogeneous, since the variability of the velocity of propagation is not noticeable in a radargram. For instance, in concrete, hyperbolic signatures from conduits are often characterized by a regular shape and similar inclination of tails (e.g. Varela-ortiz et al., 2013). Whereas, in a non-homogeneous medium

such as rock mass, the irregularity of shape and asymmetric inclination of tails are noticeable (Figure 56) due to the non-homogenous and discontinues nature of a rock mass. As shown in Figure 56, radargram 10005, a few centimeters below the bench surface, there was a hyperbolic reflection from a vertical fracture. It was noticed that the hyperbolic signature behavior of this vertical fracture was different from the hyperbolic signature behavior of rod 1 in the same radargram. Moreover, on the right of radargrm 10005, there was a fracture zone that affected the velocity of propagation; consequently, the hyperbolic signature of rod 1 in this survey line had a more noticeable different behavior compared to the hyperbolic signature of rod 1 in the other radargrams.

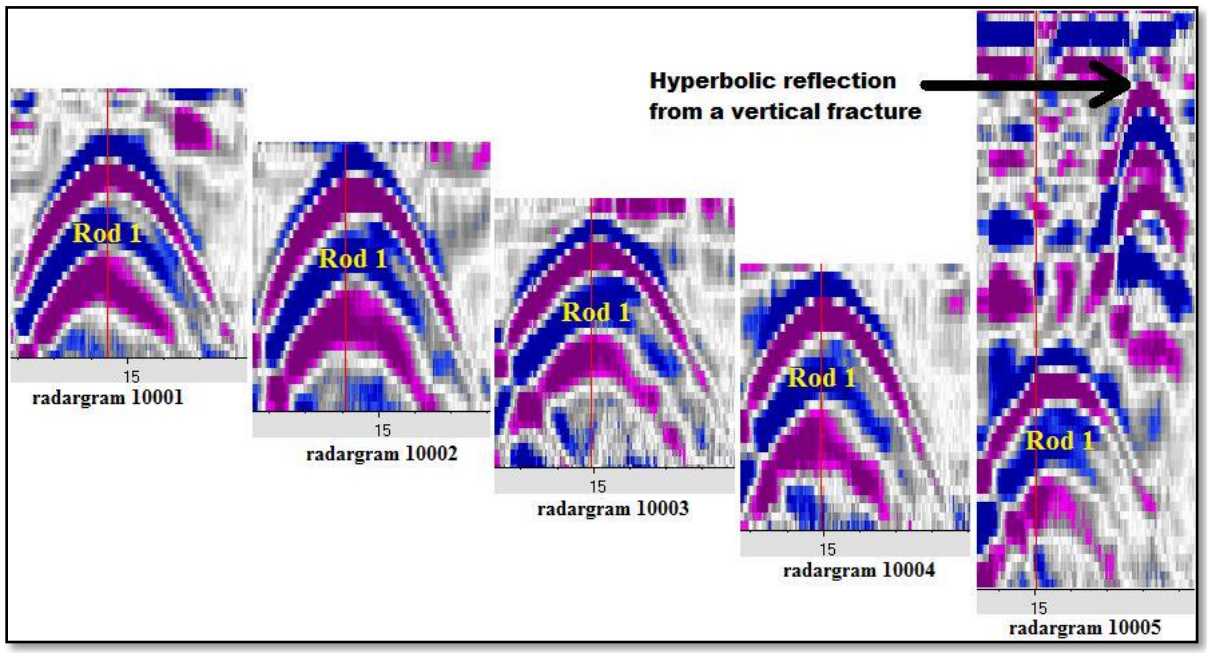

Figure 56: The variable behavior of the hyperbolic signatures of rod 1 in radargrams 10001, 10002, 10003, 10004 and 10005. All the radargrams follow the same amplitude scale shown in Figure 52.

Variable velocities of propagation in several pathways from antenna positions over the surface and a buried reflector can be estimated by Eq. 8. This was limited to reflections that have hyperbolic signatures. The methodology was based on picking data from the outline of hyperbolic signatures and inserting the picked data in a developed mathematical formulation. For each hyperbola in the radargrams of the case study, a number of points (P) were picked manually from the hyperbolic signature outline (Figure 57). Each picked point (P) was characterized by coordinates of (x, t) and causes a pathway from an antenna position over the

picked point and the rod. An illustration to how points (P) were picked in a hyperbola of the case study is presented in Figure 58. A formulation developed in an Excel spreadsheet facilitated generating points (U), laid on each pathway with constant horizontal spacing (S), and calculated the velocity of propagation in each pathway (Figure 59). In two-dimensions, a point U was characterized by the same velocity of propagation of the pathway on which a point U laid. Obviously it is physically not correct, but the objective was to transform the velocity value at each U in 2D to a dielectric constant value since it was assumed in 3D that a point U was a center of a micro cubic rock mass with a side length smaller than (S).

It is worth mentioning that points (P) of the hyperbola of each rod were separately picked twice: one from the radargrams of 200.0 MHz, and the other from the radargrams of 600.0 MHz. This was to compare the results of different pickings and to finally build a combined model of the dielectric constant in the rock mass.

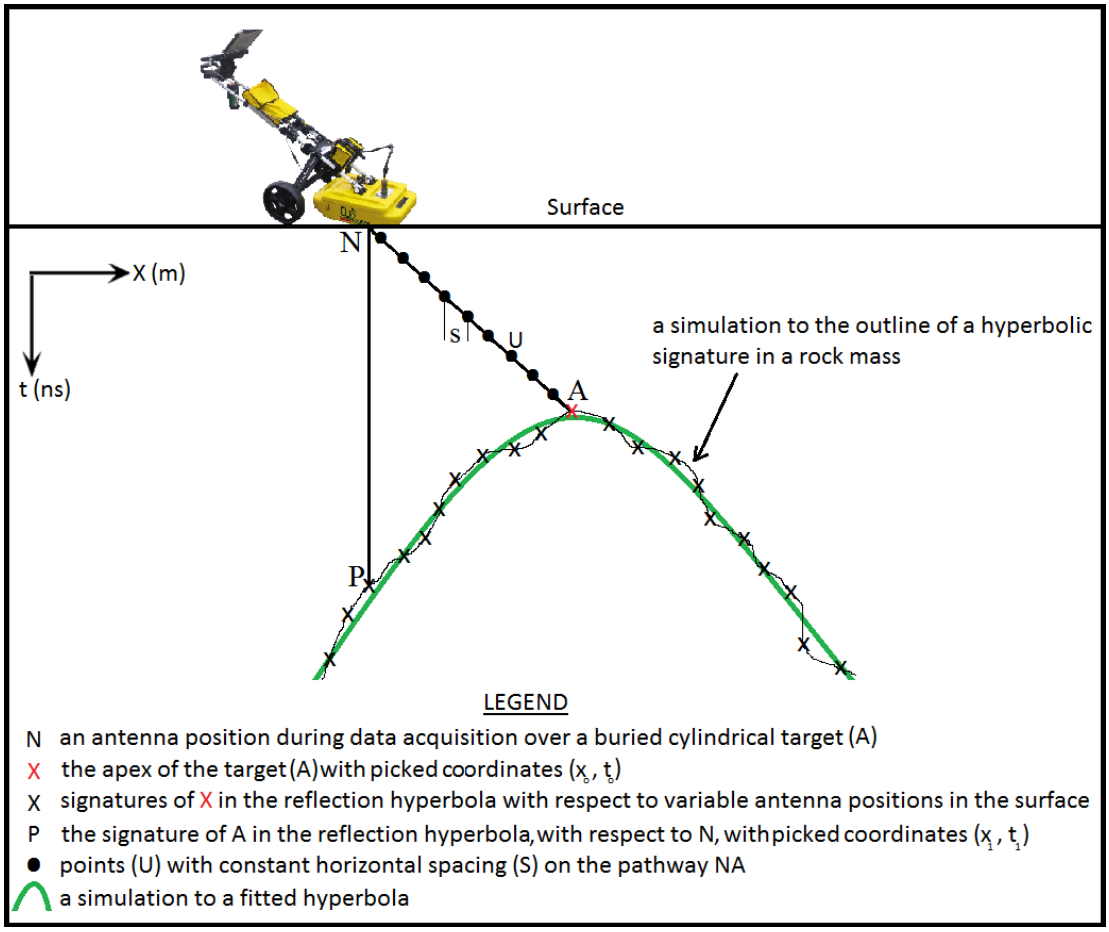

Figure 57: An illustrative sketch of the method used to estimate variable propagation velocities in several pathways from a hyperbolic reflection. A hypothetical fitted hyperbola (in green) simulates the difference between the actual values and the fitted values of velocities.

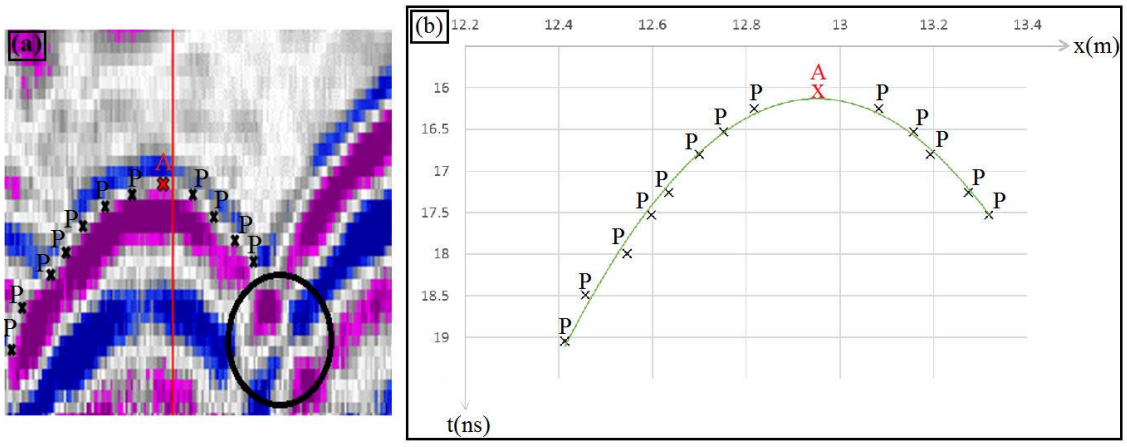

Figure 58: (a) A simulation of picking points P and point A from the outline of the hyperbolic signature of rod 3 in radargram 10001. The black circle refers to a zone neglected from picking, due to the overlapping of the tails of two hyperbolas. (b) A graphical representation of the actual picked points from the outline of the hyperbolic signature of rod 3 in radargram 10001 with a hyperbolic fitting.

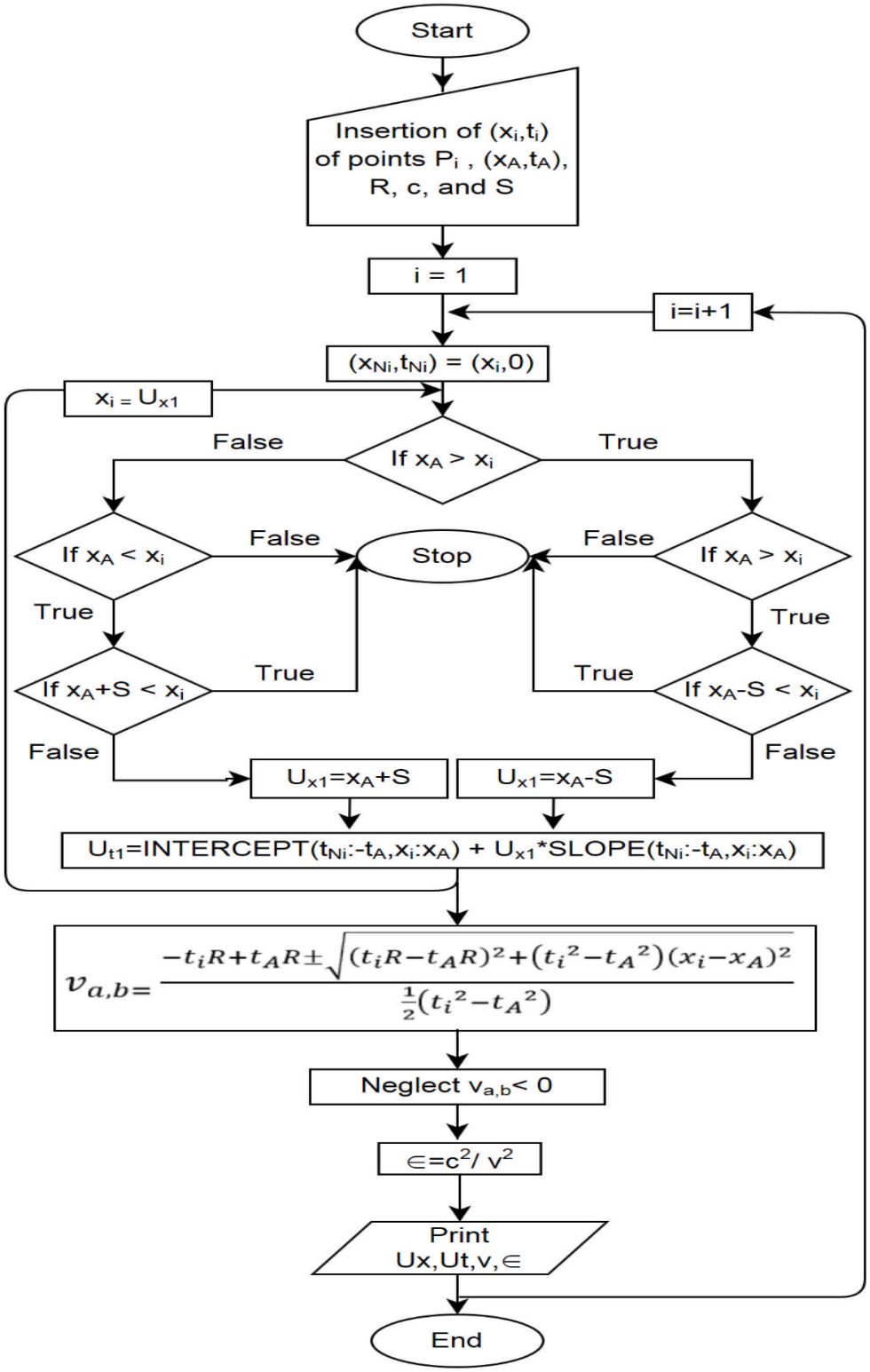

Figure 59: Flowchart of the formulation developed for estimating variable velocities of propagation in pathways.

5.3. Results

5.3.1. Visualization of the pathways' velocities

The visualization of the results was significant in this research for a deeper understanding of the variability of the velocity of propagation in pathways and to map the dielectric constant in the rock mass. Among several visualization software packages, Voxler™ (Golden Software LLC, 2017) was selected, because it has a multi-platform application for volumetric data visualization.

In order to visualize data, Voxler™ requires a set of points in a form of (x, z, y, variable). For visualizing the velocity in pathways from an antenna position to the apex of a rod, a set of points U in form of (U_x, U_z, U_y, v), generated by the developed formulation, was inserted in Voxler followed by simple processing procedures. Voxler™ is able to link points (U) laid in a pathway with a specific velocity of propagation. As an example, the pathway velocity over rod 1 in radargram 20001 is shown in Figure 60. As shown in Figure 60, there was an indication for a symmetry zone in velocity, between the two red pathways, over point A. Moving more to the right and the left, after the red pathways, velocity decreased gradually.

The author introduces the term Triangular Cross-sectional Rock Mass (TCRM) to describe a bounded area over a buried rod. The TCRM over a rod is geometrically framed by the pathway borders most to the right, most to the left, and the surface. For rod 1 in Radargram 20001, the TCRM was the cross sectional rock mass inside the triangle MLA (Figure 60). It is shown in Figure 60 that the velocities of propagation were randomly varied in the TCRM over rod 1 in a range of velocities from 103 to 113 Mm/s. The term TCRM was introduced to be used as a comparison parameter of the average velocity of propagation over the rods and to explore the variability in the velocity of pathways through a wider area (a full radargram) as well. Pathway velocities over rods 1, 2, 3, and 4 in radargram 20001 were visualized in Figure 61. The velocity was varied in a wider range, from 77.0 to 120.0 Mm/s, for a wider area than in Figure 60, and however, velocity variability for each TCRM over the rods, in Figure 61, was still clear. The general trend of the velocity variability was to decrease towards rod 4.

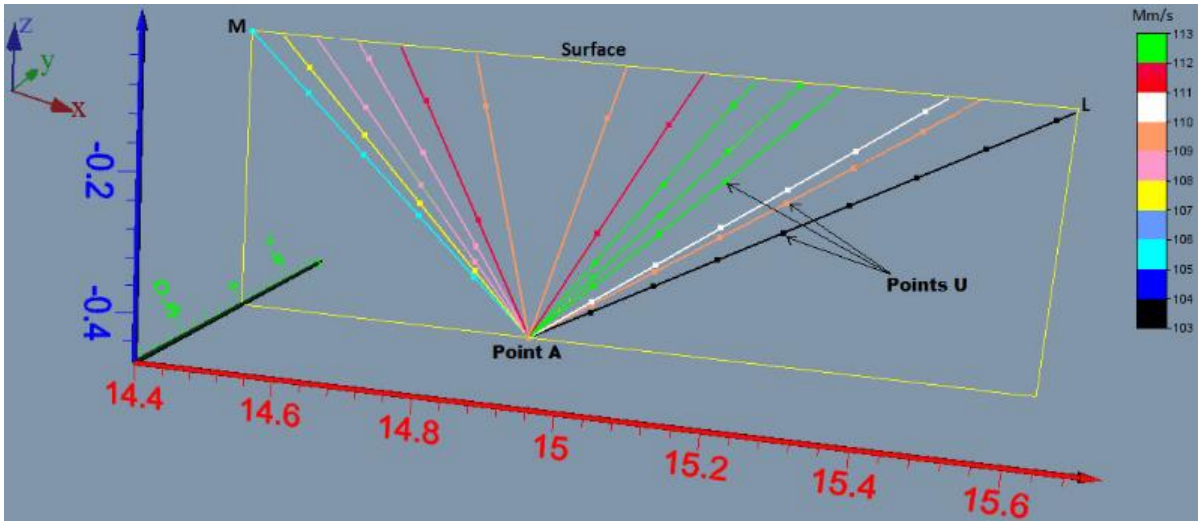

Figure 60: Visualization of pathways with variable velocity of propagation from antenna positions to the apex of rod 1 (point A in the figure) in radargram 20001.

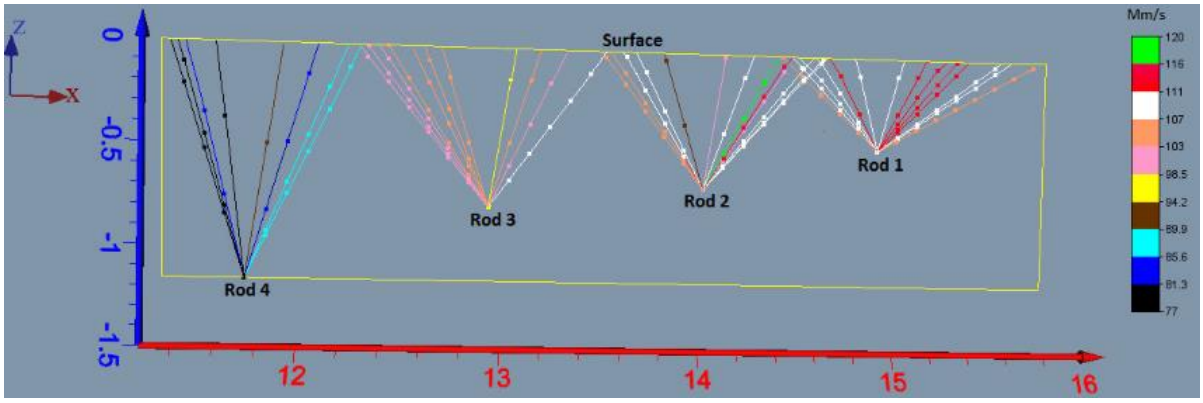

Figure 61: Visualization of the pathways of variable velocities of propagation in radargram 20001.

The points (P) were picked in independent ways from the two hyperbolic signatures of a rod in both the radargrams of 200.0 MHz and 600.0 MHz of a surveyline. A total of 787 and 748 points (A+N+U) with 4D coordinates (x, t or z, y, v or ε_r) were generated by the formulation developed, from the radargrams of 200.0 MHz and 600.0 MHz respectively. The results of two independent picking of points P, in the radargrams of 200.0 MHz and 600.0 MHz, were compared in terms of the average velocity of propagation in the TCRM over each rod (Table 13). The difference between the values of the average velocities of propagation in the TCRM for a rod in two independent pickings were in a range from 0.12 % to 1.52 % with a relative difference mean of ± 0.82 Mm/s (not considering the footnoted value in Table 13). In survey lines 1, 2, and 3, the average velocity of propagation of TCRM decreased gradually towards rod 3. Differently, in survey lines 4 and 5 there were peaks in the average velocity of

propagation of TCRM over rod 2. In the perpendicular direction to the survey lines, there was no noticeable trend for the average velocity variability of TCRM over the rods.

Table 13: Estimated velocities of propagation of the TCRM over the rods.

detected rods	antenna (MHz)	estimated velocity of propagation of TCRM (Mm/s)				
		survey line 1	survey line 2	survey line 3	survey line 4	survey line 5
rod 1	200.0	108.9	110.2	110.4	106.7	104.2
	600.0	108.1	110.8	109.4	107.8	104.3
rod 2	200.0	107.6	106.2	104.8	110.0	114.3
	600.0	106.7	107.0	105.7	108.9	113.9
rod 3	200.0	102.2	103.2	99.0	97.2	98.6[a]
	600.0	100.6	104.4	99.9	96.3	98.6
rod 4	200.0	84.5	lost data	lost data	lost data	95.7
	600.0	84.9	lost data	lost data	lost data	95.1

A propagation velocity for the cross-sectional rock mass of each radargram could be estimated by taking the average of the pathway velocities; consequently, an average dielectric constant for each radargram could be estimated as well (Table 14). In Table 14, taking an average value from different frequencies was just for considering the largest amount of data obtained from the 200.0 and 600.0 MHz radargrams, since the modelled velocities obtained from data of independent manual pickings in each frequency of a radargram. In the cross-sectional rock mass of survey line 1, the average dielectric constant was the highest (8.9), followed by a sudden decrease in survey line 2 and then it started to gradually increase up to a value of 8.5 in survey line 5.

For the purpose of accurate estimation of the bulk dielectric constant of the studied rock mass body, whole the modelled velocities obtained from the 200.0 and 600.0 MHz radargrams could

[a] The hyperbola of rod 3 in radargram 20005 is not clear enough to be trusted for picking points P due to noise. It is assumed that the results of picking points from the hyperbol of rod 3 in radargram 2005 are equal to the results obtained from rod 3 in Radargram 10005.

be averaged as well. The bulk velocity of propagation in the rock mass body was 104.0 Mm/s, whilst the bulk dielectric constant value of the rock mass body was 8.4. These values were those recommended in any data processing and interpretation of 3D GPR data in this rock mass.

Table 14: Estimated velocity of propagation and dielectric constant for each radargram.

antenna (MHz)	estimated velocity of propagation (v) per radargram (Mm/s)				
	survey line 1	survey line 2	survey line 3	survey line 4	survey line 5
200.0	100.8	106.5	104.7	104.6	103.2
600.0	100.1	107.4	105.0	104.3	103.0
avgerage v from combining 200.0 and 600.0 MHz	100.5	107.0	104.9	104.5	103.1
antenna (MHz)	estimated dielectric constant (ε_r) per radargram				
	survey line 1	survey line 2	survey line 3	survey line 4	survey line 5
200.0	8.8	7.9	8.2	8.2	8.4
600.0	9.0	7.8	8.2	8.3	8.5
avgerage ε_r from combining 200.0 and 600.0 MHz	8.9	7.9	8.2	8.3	8.5

5.3.2. Velocities from the hyperbola fitting method

Hyperbola fitting is a typical method, provided by several packages of GPR signal processing software, for estimating the velocity of propagation in a medium by using mathematical models that minimize error criterion. The fitting is based on adapting the tails of a synthetic hyperbola to visually fit hyperbolic signatures in radargrams. Roughly speaking, the fitting hyperbola method can optimally minimize the error criterion in homogeneous medium, such as concrete, since the hyperbolic signatures in homogeneous medium are quite sharp, regular and symmetric. While in a non-homogeneous medium such as rock mass, the hyperbolic signatures can have different characteristics.

The purpose of the section was to present that the results obtained by the proposed method were relevant or close to the method of fitting hyperbola used in a commercial software package. The author used the results of the fitting hyperbola method as a reference to validate

the values of velocities obtained by the developed method. The study in this section was limited to exploring to what extent the values of the estimated velocities of propagation from the proposed method, particularly within the TCRM, and the hyperbola fitting method are relevant. The hyperbolic signatures of the buried rods, in all the radargrams of 200.0 MHz and 600.0 MHz, were fitted by the processing software GRED^{TM} (Figure 62). The fitting was performed in the outer boundary of the hyperbolic signature, from which points (P) were picked. The results are presented in Table 15. In Table 15, the results from the fitting showed that the estimated velocities of propagation from radargrams of 200.0 MHz and 600.0 MHz were almost close or similar; however, it depends on the operator's experience in fitting the synthetic hyperbola tails. The difference between the values of average velocities of propagation in Table 13 and Table 15 were in a range from 0.0 % to 2.5 %, mainly due to the differences between estimated values and estimated fitted values, with a relative difference mean of ± 1.17 Mm/s.

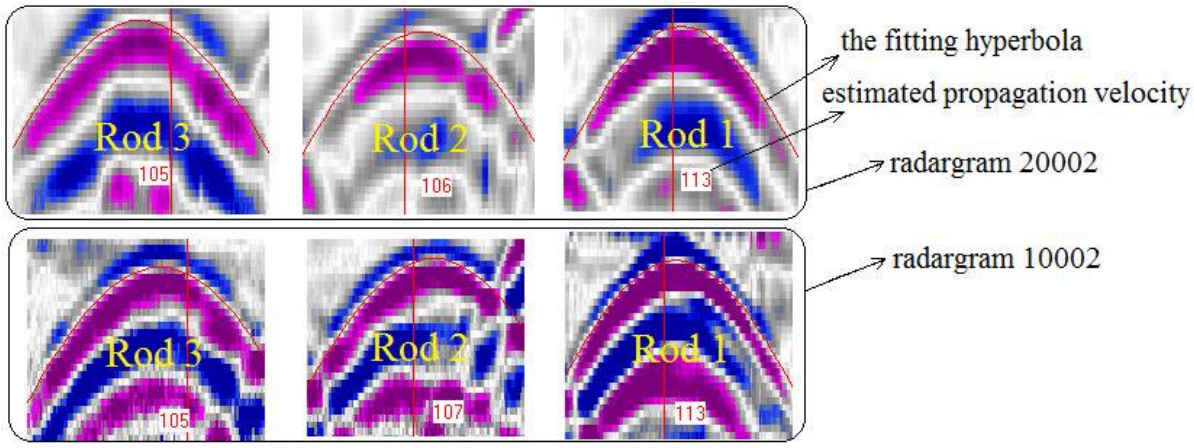

Figure 62: Estimating the velocity of propagation in radargrams 20002 and 10002, using the hyperbola fitting method, through the processing software package (GRED^{TM}).

Table 15: Estimated velocity of propagation through the hyperbola fitting method in the processing software package (GRED^{TM}).

detected rods	antenna (MHz)	estimated velocity of propagation from fitted hypberbolas (Mm/s)				
		survey line 1	survey line 2	survey line 3	survey line 4	survey line 5
rod 1	200.0	111.0	113.0	111.0	107.0	103.0
	600.0	110.0	113.0	111.0	107.0	104.0
rod 2	200.0	109.0	106.0	106.0	110.0	115.0
	600.0	108.0	107.0	106.0	110.0	113.0
rod 3	200.0	102.0	105.0	100.0	99.0	100.0[b]
	600.0	102.0	105.0	101.0	100.0	100.0
rod 4	200.0	85.0	lost data	lost data	lost data	97.0
	600.0	84.0	lost data	lost data	lost data	97.0

5.3.3. Three-dimensional mapping of the dielectric constant variability

From Figure 60 & 61 and Tables 13 & 14, there are obvious indicators that the dielectric constant of the rock mass was varied in a random behavior that requires 3D mapping for deeper studying. Since it was assumed that points U, in three dimensions, are micro cubic units, they can be characterized by dielectric constant values. The 4D coordinate set of points (U_x,U_z, U_y, ε_r) were interpolated by the inverse distance method, using Voxler^{TM} software package, to map the dilectric constant in the rock mass (Figure 63a&b). The dielectric constant variability was modeled in a 3D rock cuboid; however, there were no corresponding data below the rods. Thus, the uncertainty of the modeled dielectric constant values in the 3D volume below the rods was quite higher than the upper 3D rock volume which contains whole the data of the TCRM.

It was noticed that there were few differences in the dielectric constant mapping between the models of 200.0 MHz (Figure 63a) and 600.0 MHz (Figure 63b). However, the general

[b] The hyperbola of rod 3 in radargram 20005 is not clear enough to be trusted, due to noise, for fitting. It is assumed to have the same value obtained from fitting the hyperbola of rod 3 in Radargram 10005.

variability behavior, in the two models, was the same. These differences consisted in the relative increase or decrease in size of an interpolated isosurface of a dielectric constant value; the isourfaces in Figure 64 were identified in Table 16. The differences were mainly because of a relative increase or decrease in the number of picked points (P), over a particular part in the outline of a hyperbolic signature of a rod, in a radargram of a frequency, and the number of picked points (P), in the equivalent part of the hyperbolic signature, of the same rod, in the equivalent radargram of the other frequency.

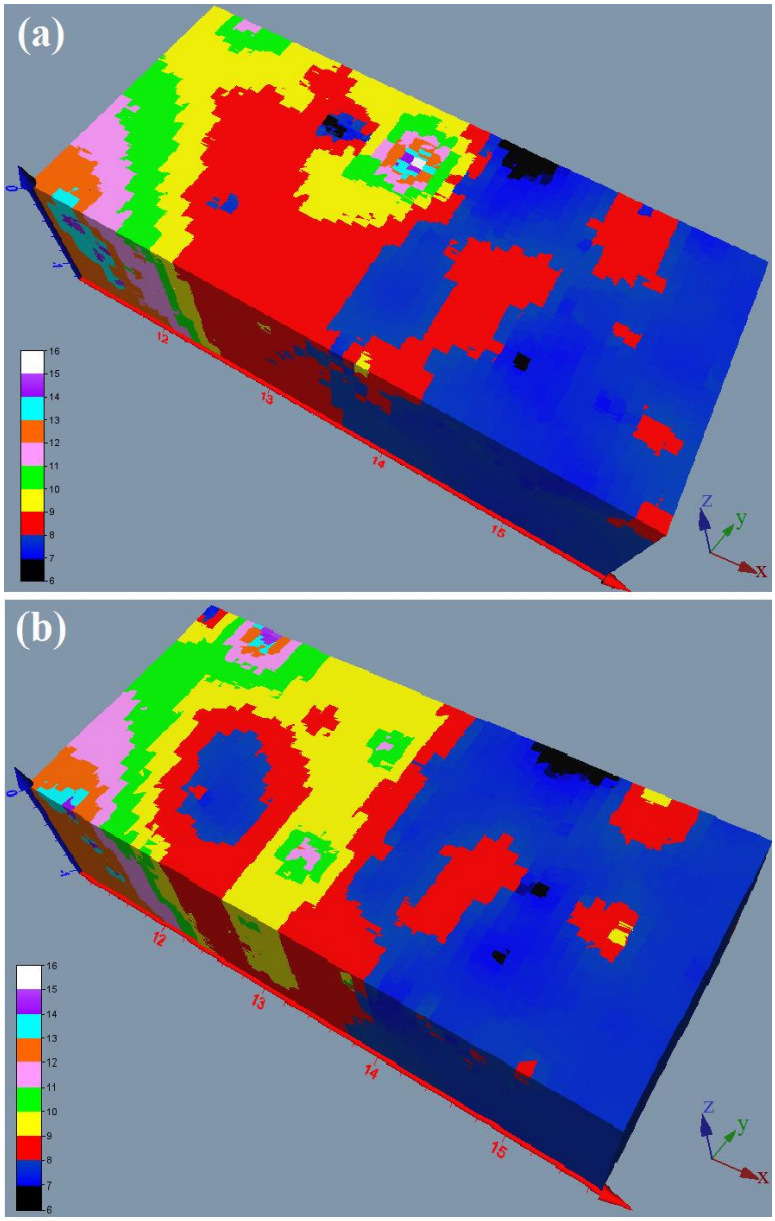

Figure 63: Mapping of the dielectric constant variability, in the rock mass, obtained from two independent pickings of points P in the radargrams of 200.0 MHz (a) and 600.0 MHz (b). The dielectric constant values are indicated by a color scale on the left for the two models.

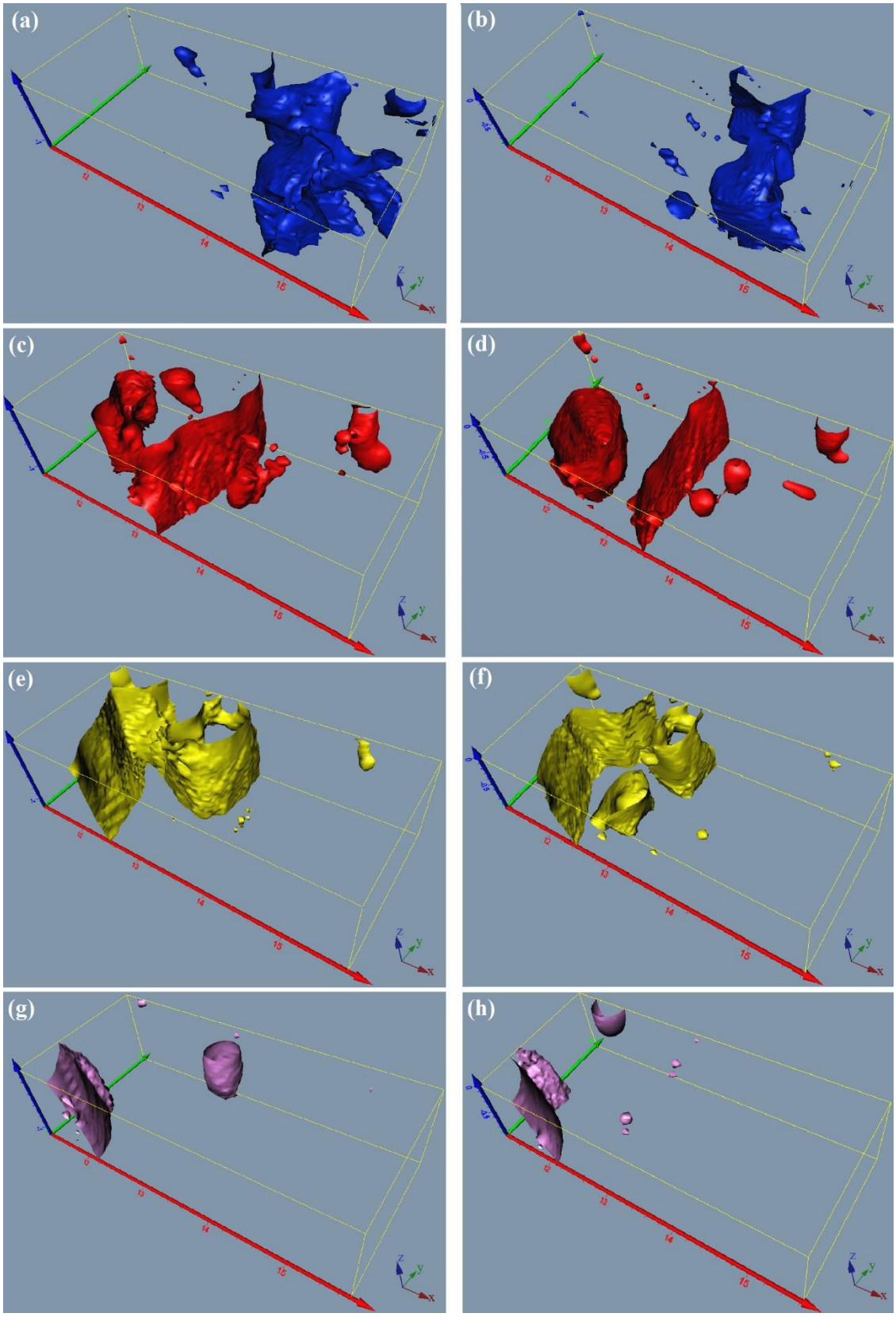

Figure 64: Isosurfaces of different dielectric constant values in the rock mass. The isosurfaces values in the sub-figures are identified in Table 16.

Table 16: Identification of the values of the isosurfaces in Figure 64.

figure	Isosurface value of dielectric constant	from the model of
18-a	7.5	200.0 MHz
18-b	7.5	600.0 MHz
18-c	8.5	200.0 MHz
18-d	8.5	600.0 MHz
18-e	9.5	200.0 MHz
18-f	9.5	600.0 MHz
18-g	11.5	200.0 MHz
18-h	11.5	600.0 MHz

Combining together the points (U) obtained from the two independent picked points (P), in 200.0 MHz and 600.0 MHz radargrams, will increase the number of the 4D set of points (U) required for mapping. It leaded to a more accurate and representative model of the 3D mapping of dielectric constant variability (Figure 65). From the combined model, it is clear that the major part of the rock mass had a dielectric constant value in a range from 7.0 to 9.0 which was compatible with the bulk dielectric constant value (8.4) obtained from Table 14.

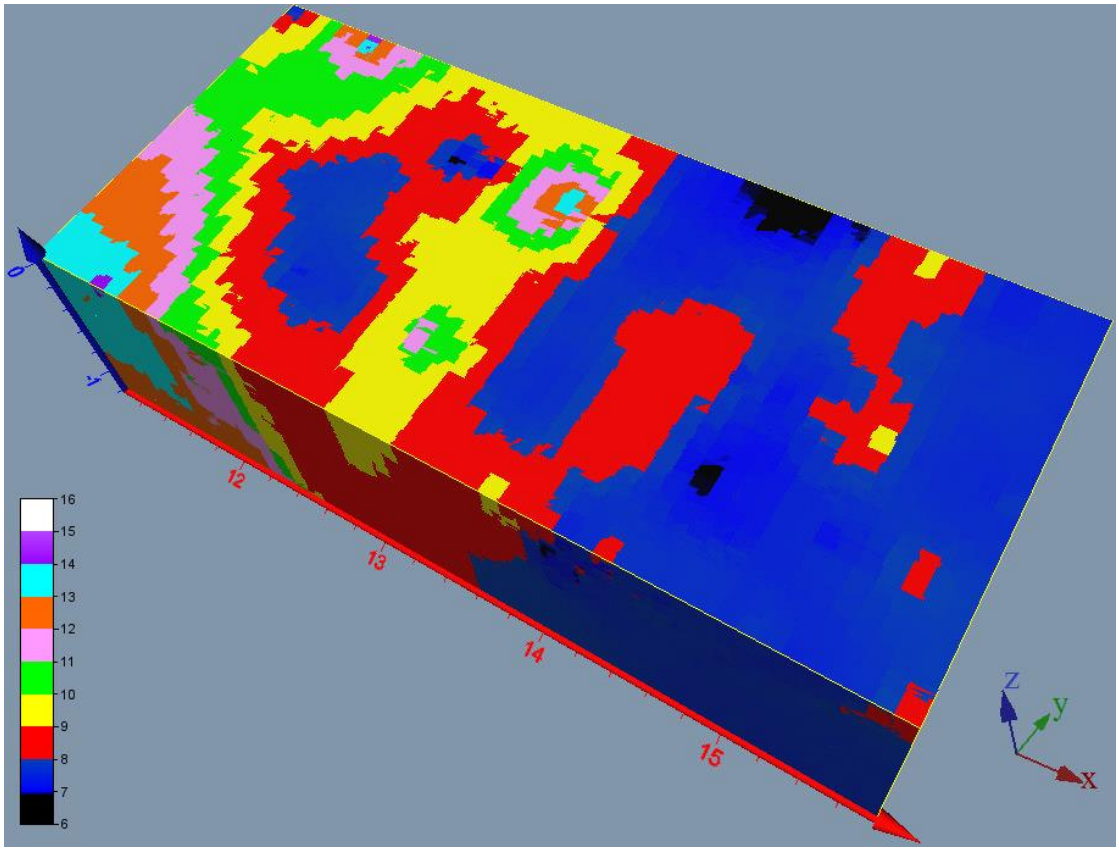

Figure 65: Mapping of the dielectric constant variability obtained from combining the two independent picked points (P) in 200.0 MHz and 600.0 MHz radargrams. The dielectric constant values are indicated by a color scale on the left of the figure.

It is worth mentioning that the interface between the blackish gray sandstone and the gray sandstone could not be recognized in the 3D models of the dielectric constant. This is mainly because the propagation velocity was estimated in pathways where passed by both the blackish gray sandstone and the gray sandstone strata. Thus, a represented value of the propagation velocity in a pathway within the two stratum was calculated. The interface of the blackish gray sandstone and the gray sandstone could be visible only if a number of rods were buried at the depth of the interface between the two strata.

5.4. Conclusions

In non-homogenous medium, the propagation velocity of electromagnetic waves is subjected to variation in space. To characterize the propagation velocity variation in a rock mass, the author surveyed by GPR a rock mass where buried steel rods were used as artificial reflectors. The reflectors produced hyperbolic signatures in radargrams which were used through a developed velocity estimation method that took in account several pathways of the electromagnetic waves in the rock mass. The velocity of propagation was estimated through three main scales within the rock mass: (i) micro scale (TCRM), (ii) radargram scale, and (iii) macro scale of 3D rock body. The results showed that the velocity of propagation in a radargram varied randomly within the whole radargram and even within just a region over a buried rod (TCRM). The estimated average propagation velocities, within the TCRM over the rods by the proposed method were found close to those obtained by the fitting hyperbola method provided in the signal processing software package GRED^{TM}. A promising use of Voxler^{TM} software package in this study allowed to visualize the modeled pathways of velocity in 2D in addition to mapping the dielectric constant in the 3D rock mass body by interpolating the discrete points within the pathways. Since an average value of the dielectric constant is being used to convert the travel time to depth in a radargram, the knowledge of range variation of the dielectric constant in a radargram can be used to divide the radargram in several portions, using different average values for each one. Such division of radargrams has not been considered so far in the signal processing software packages which can be useful for GPR applications that require high accuracy of identifying subsurface depth of utilities.

CHAPTER 6

Block Scale Optimization

6.1. Background

Ornamental stone products are sold as blocks, slabs and or tiles. For each item, there are several commercial sizes which serve different applications of building and construction. Slabs and tiles are cut from blocks and then followed by the processing required for each specific application. Commercially, a leading factor that gives a profitable value to the stones is the commercial size of slabs and tiles cut from blocks. The size of slabs and tiles is controlled by the kind of application.

Generally, the larger the slabs and tiles, the higher the selling price. Discontinuities adversely affect the quality of ornamental stone blocks and consequently affect the size of slabs and tiles that can be obtained from blocks.

Following this, in terms of optimization of cutting slabs aiming to maximizing the recovery ratio, the following research questions were opened: i) what is the optimum size of slabs/tiles that can be cut from a block?, ii) which face of the block (parallel to x-plane, y-plane, or z-plane) is the optimum cutting face, and iii) and what is the optimum rotation angle of cutting slabs from a block? These research questions could be answered, as presented in this chapter, through developing an optimization model for cutting slabs and tiles from blocks based on the developed 3D deterministic fracture modeling approach provided in Chapter 4. Up to the author's best of knowledge, this is the first kind of production optimization model in the scale of ornamental stone blocks.

6.2. Method

6.2.1. Development of a 3D geometric optimization algorithm

The algorithm developed is based on generating a hypothetical 3D cutting grid for a block. The 3D cutting grid consists of slabs with equal dimensions (dim_x, dim_y, dim_z), as shown in Figure 66. The 3D cutting grid spreads from the geometric center of the block (C) within a specified domain of dimensions: n_x, n_y, n_z. This domain geometrically allows the 3D cutting grid of slabs to cover the 3D domain of the block, during the whole run of the algorithm, using an extra number of slabs as safety factor. The geometric parameters of the block are described by the spatial domain bounded by the minimum and maximum Cartesian coordinates (x_min, x_max, y_min, y_max, and z_min: z_max).

The algorithm checks for the intersection between the slabs (generated in the hypothetical cutting grid) and the discontinuities model or the six faces of the block body. In this paper, the discontinuities model refers to a model of fractures, joints, voids, or any structural weaknesses. Iteratively, the 3D cutting grid is rotated, through a 3D rotation, in such a way to test the possible cutting orientations of slabs, which can be parallel to the XY plane, XZ plane, or YZ plane of the block (see Figure 67 and Table 17). In addition, the cutting grid is moved through several 3D displacements (dx, dy, dz), defined by:

$(-dim\_x)/2 \leq dx < (+dim\_x)/2$, with a step of dx_step, for dx

$(-dim\_y)/2 \leq dy < (+dim\_y)/2$, with a step of dy_step, for dy

$(-dim\_z)/2 \leq dz < (+dim\_z)/2$, with a step of dz_step, for dz

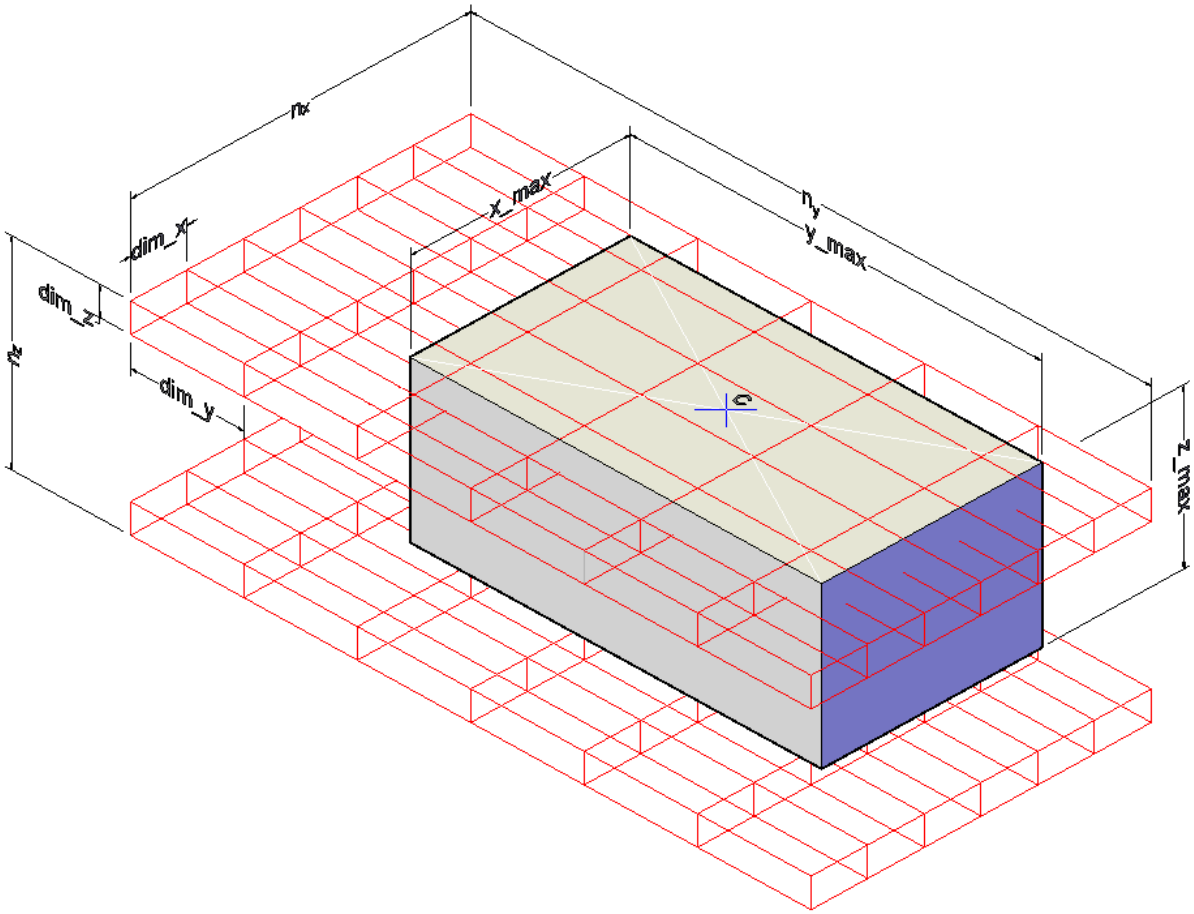

Figure 66: An illustrative sketch shows the 3D cutting grid of slabs (coloured in red) within the block body.

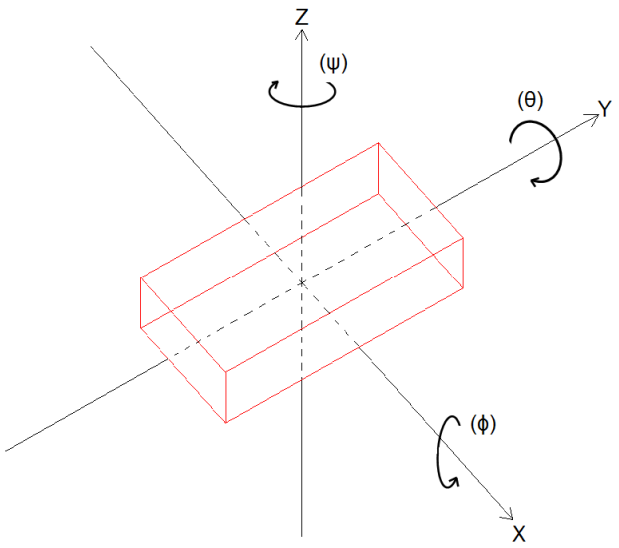

Figure 67: An illustrative sketch shows the possible orientaion-rotation of the 3D cutting grid of slabs.

Table 17: The six possible orientations-rotations of the 3D cutting grid of slabs.

cutting orientation of slabs	rotation of slabs	the relative orientation-rotation		
		theta θ	phi ϕ	psi ψ
XY plane	0°	0°	0°	0°
XY plane	90°	0°	0°	90°
XZ plane	0°	90°	0°	0°
XZ plane	90°	90°	90°	0°
YZ plane	0°	90°	0°	90°
YZ plane	90°	90°	90°	90°

The intersection between a slab and a discontinuity (or the faces of the block body) is searched by using a fast segment/triangle intersection algorithm (Guigue and Devillers, 2003). Each discontinuity as well as the faces of the block body are geometrically represented by triangles. For each 3D cutting grid patterns of slabs generated, each slab is tested if it intersects a discontinuity or a face of the block. Therefore, for each slab composed of 12 edge segments, the algorithm checks the intersection between the 12 edge segments and all the triangles that compose the discontinuities model. Then, the algorithm calculates the number of non-intersected slabs and total number of slabs (intersected + non-intersected) with a full size inside the block body. Consequently, the recovery ratio can be calculated for each displacement in each orientation-rotation to determine the optimum cutting grid configuration using Eq. (9). The recovery ratio can also be called coefficient of utilization as given and defined in (Vidić et al., 2012). Hence, the recovery ratio described in Eq. (9) is limited to a certain slab size and

it doesn't consider that a remaining portion of the block body can or cannot be optimally cut in smaller sized slabs.

$$recovery\ (\%) = \frac{volume\ of\ non-intersected\ slabs\ with\ full\ dimension\ inside\ the\ block\ body\ x\ 100}{total\ volume\ of\ the\ block\ body\ studied} \quad (9)$$

During the cutting operation of the slabs, a volume of the block is also wasted due to the sawing process. This algorithm considers the thickness of the cutting saw and the relative volume of waste produced.

6.2.2. Software development (SlabCutOpt)

The developed algorithm was coded using the C++ programming language which can work in the environment of parallel processors to speed the computation process. The developed software packages was named "SlabCutOpt" derived from the aim of the program which is "Slab Cutting Optimization".

6.2.2.1. Input files

The input data of SlabCutOpt is composed of several files:

• SlabCutOpt.par: it is an ASCII file containing the input parameters of the model. It must contain: the geometric parameters of the block body, the orientation-rotation and displacement parameters and options about the operating mode and the output mode, etc. Optionally, the algorithm can operate in 2D, avoiding testing for the Z dimension. See Appendix B for details;

• PLY files: each modelled discontinuity or set of discontinuities has to be stored in PLY file format. See Appendix C for details;

• PLY_FileList.dat: it is the ASCII file containing the list of the Ply files of the modelled discontinuities set. See Appendix D for details.

• slab_dimensions.dat: it is the ASCII file containing the list of the different sizes of slabs to be tested. See Appendix E for details

6.2.2.2. Output files

The output of SlabCutOpt are ASCII files with detailed information about the results of the run. The output files of SlabCutOpt are composed of several files:

•Results.log file: it is an ASCII file, where for each slab size, each line contains: the orientation of the 3D cutting grid of slabs, the displacements used, the number of non- fractured slabs inside the block body, and the number of fractured slabs inside the block body. See Appendix F for details.

•slabs vtu files: for each single displacement or the solution of maximum number of non-intersected slabs within each slab size, a vtu file is written to allow 3D visualization of the results. The vtu files can be then visualized using ParaView program. A slab type colour is assigned to each slab to allow easy identification of slabs inside the block body: fractured slabs and non-intersected slabs. See Appendix G for details.

6.3. Case study

In this section, the results of applying the developed optimization model (SlabCutOpt) on the limestone block, presented in Section 4.2.2, are presented. Commercially, there is a wide range of slabs and tiles which each size serve a certain construction or building purpose. For the rock material of the limestone block under study, the selling price list of all the products of slabs and tiles is confidential. However, with an agreement with the quarry management, the author converted the price list from Euros (€) to Relative Money Value (RMV) in order to publish the results. RMV is the relative value of the price of a unit to the maximum unit price. In Table 18, a series of selected sizes of slabs and tiles, for the referred block material, with their RMV is listed. Interestingly, a linear relation between the size of slabs and their selling price was found (Figure 68).

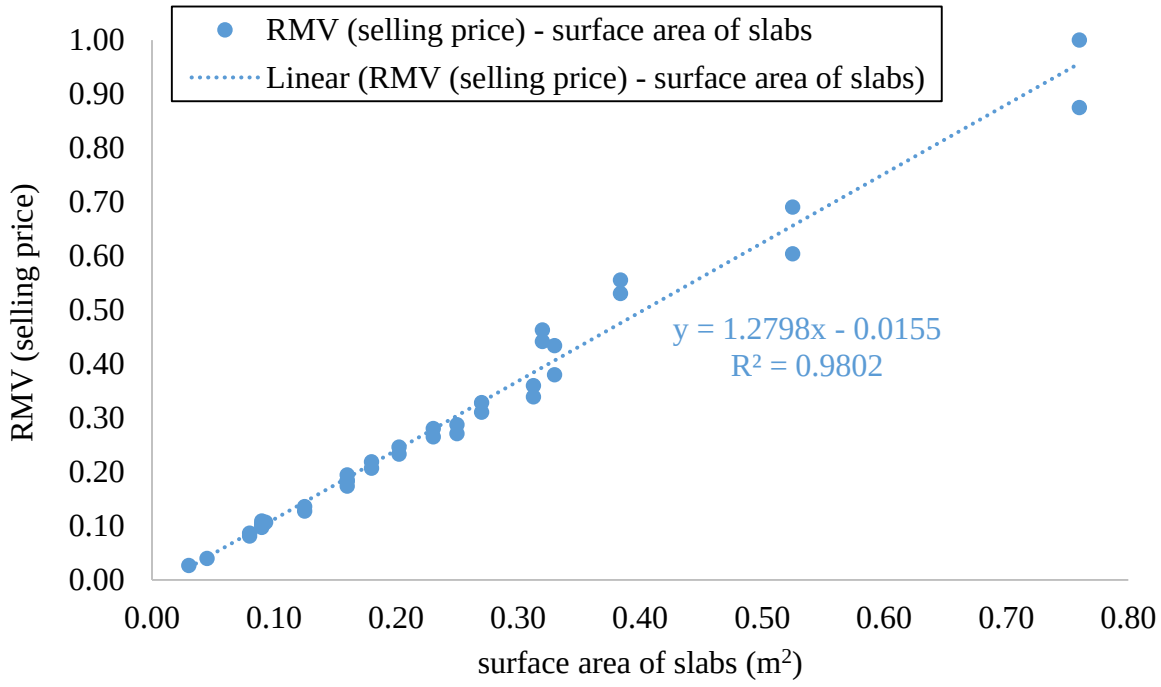

Figure 68: The linear correlation between the sizes of slabs and tiles and the RMV.

Table 18: The tested commercial sizes of slabs and tiles with their RMV.

size	dimensions of slabs and tiles			RMV per unit	surface area (m^2)
	X (cm)	Y (cm)	Z (cm)		
size 1	40.00	20.00	1.50	0.082	0.08
size 2	50.00	25.00	1.50	0.127	0.13
size 3	40.00	20.00	2.00	0.087	0.08
size 4	50.00	25.00	2.00	0.136	0.13
size 5	60.00	30.00	1.50	0.207	0.18
size 6	30.00	30.00	1.50	0.104	0.09
size 7	40.00	40.00	1.50	0.184	0.16
size 8	60.00	45.00	1.50	0.311	0.27
size 9	45.00	45.00	1.50	0.233	0.20
size 10	48.00	48.00	1.50	0.265	0.23
size 11	60.00	30.00	2.00	0.219	0.18
size 12	30.00	30.00	2.00	0.110	0.09
size 13	40.00	40.00	2.00	0.195	0.16
size 14	60.00	45.00	2.00	0.329	0.27
size 15	45.00	45.00	2.00	0.246	0.20
size 16	48.00	48.00	2.00	0.280	0.23
size 17	80.00	40.00	1.50	0.442	0.32
size 18	80.00	48.00	1.50	0.531	0.38
size 19	80.00	40.00	2.00	0.463	0.32
size 20	80.00	48.00	2.00	0.556	0.38
size 21	30.50	30.50	1.00	0.107	0.09
size 22	30.00	15.00	3.00	0.040	0.05
size 23	30.00	10.00	3.00	0.027	0.03
size 24	30.00	110.00	2.00	0.380	0.33
size 25	35.00	150.00	2.00	0.604	0.53
size 26	40.00	190.00	2.00	0.875	0.76
size 27	30.00	110.00	3.00	0.434	0.33
size 28	35.00	150.00	3.00	0.691	0.53
size 29	40.00	190.00	3.00	1.000	0.76
size 30	15.00	60.00	2.00	0.098	0.09
size 31	20.00	80.00	2.00	0.174	0.16
size 32	25.00	100.00	2.00	0.271	0.25
size 33	25.00	125.00	2.00	0.339	0.31
size 34	15.00	60.00	3.00	0.104	0.09
size 35	20.00	80.00	3.00	0.184	0.16
size 36	25.00	100.00	3.00	0.288	0.25
size 37	25.00	125.00	3.00	0.360	0.31

6.4. Results and analysis

The listed sizes of slabs in Table 18, were tested in SlabCutOpt. The used algorithm parameters (SlabCutOpt.par file) are presented in Appendix B.

For each slab size, the possible solutions were generated within the six orientations-rotations of the 3D cutting grid of slabs, see a visualized example from applying SlabCutOpt on the slab size No. 1 in Figure 69. In Figure 69, the 3D cutting grid of slabs (colored in blue) is partially visualized in a 3D clip to show the inherent resulting intersected and non-intersected slabs. The modelled discontinuities inside the limestone block body were visualized in the same colors as in the model presented in Section 4.2.2. The consideration of the cutting saw thickness is clearly visible (Figure 69g).

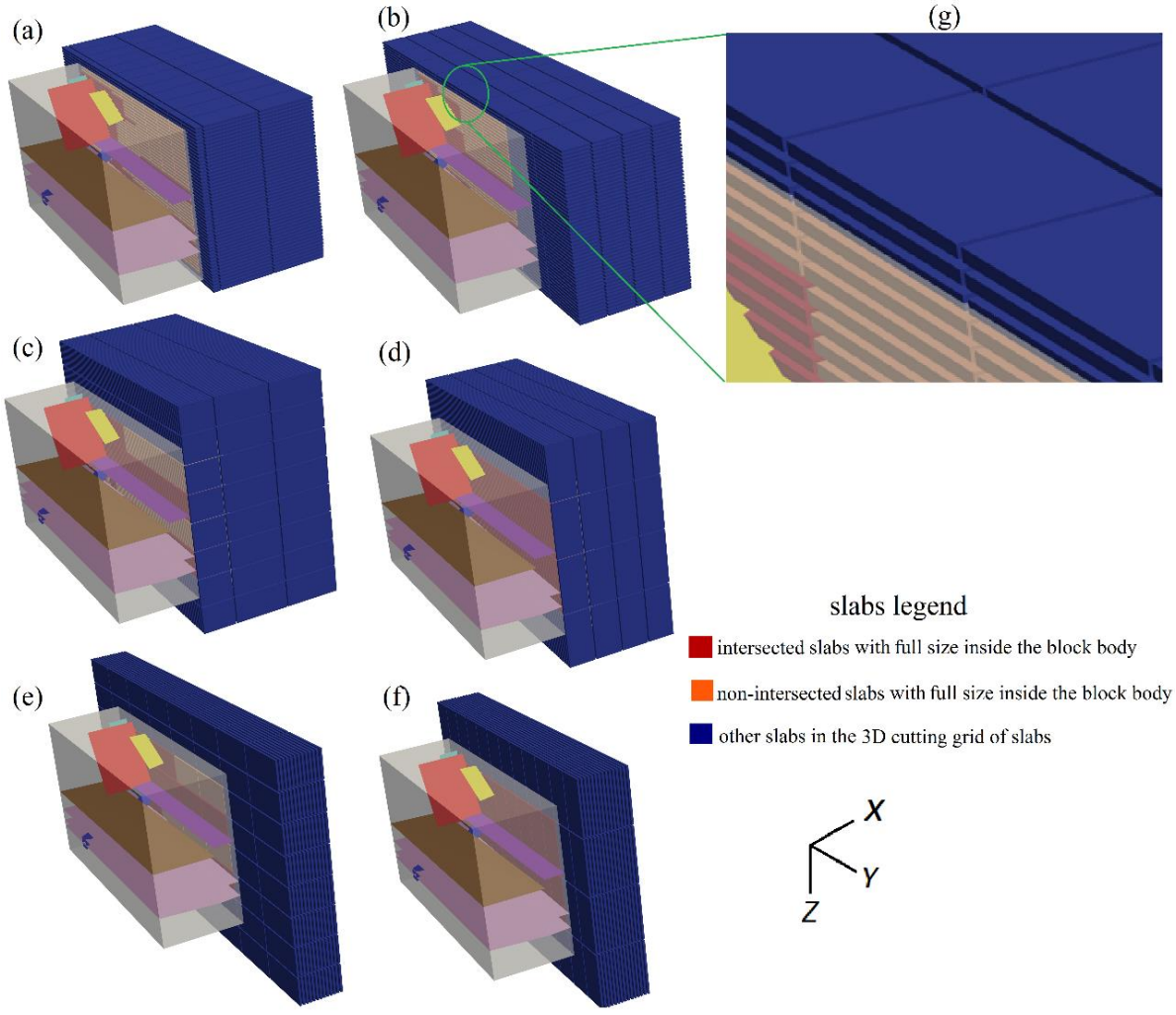

Figure 69: The visualized six orientations-rotations of the 3D cutting grid of slabs in ParaView within the results of the slab size No. 1, details of the sub-figures are in Table 19.

Table 19: Details of the sub-figures presented in Figure 69.

sub-figure	cutting orientation of slabs	rotation of slabs
Figure 69a	XY plane	0°
Figure 69b	XY plane	90°
Figure 69c	XZ plane	0°
Figure 69d	XZ plane	90°
Figure 69e	YZ plane	0°
Figure 69f	YZ plane	90°

By way of example, the results of the slab size No. 1 (40.0 cm, 20.0 cm, 1.50 cm) are given in Figure 70. For this size, the optimum recovery was 35.7 %, found in the cutting orientation parallel to plane XY – slab rotation 0.0° at a displacement of (dx = -0.01 m, dy = 0.1 m, dz = -0.01 m). It can be observed, from Figure 70, that the recovery ratio can vary within each single orientation-rotation as well as between the six orientations-rotations. A video presents a visualized run of SlabCutOpt for the slab size No. 1 can be viewed through this link (https://www.youtube.com/watch?v=SR_ZeToq4FQ&feature=youtu.be).

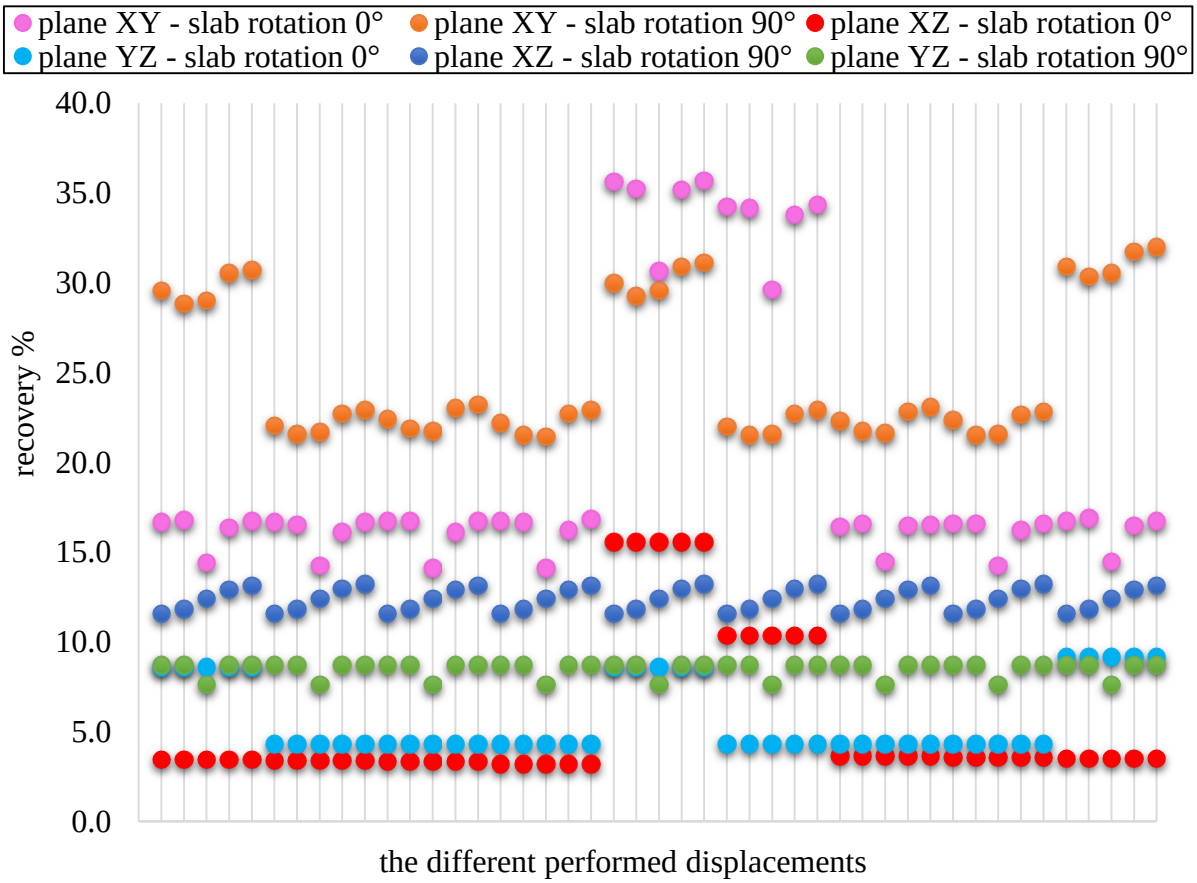

Figure 70: The graphical representation of the optimization results for the slab size No. 1.

The maximum number of non-intersected slabs and the maximum recovery ratio for each tested slab size are graphically represented in Figure 71. The optimum recovery ratio of 44.91 % was found in slab size No. 23, within the cutting orientation parallel to plane XY – slab rotation 90.0° at a displacement of (dx = -0.01 m, dy = 0.05 m, dz = -0.02 m), which can be considered the most environmental friendly solution. As can be seen from Figure 71, the graphical histogram representation of the maximum recovery is not fully compatible with the representation of the maximum number of non-intersected slabs. For example, the maximum recovery ratio for slab size No. 13 is higher than for slab size No. 12; however, the maximum number of non-intersected slabs for slab size No. 13 is lower than for slab size No. 12.

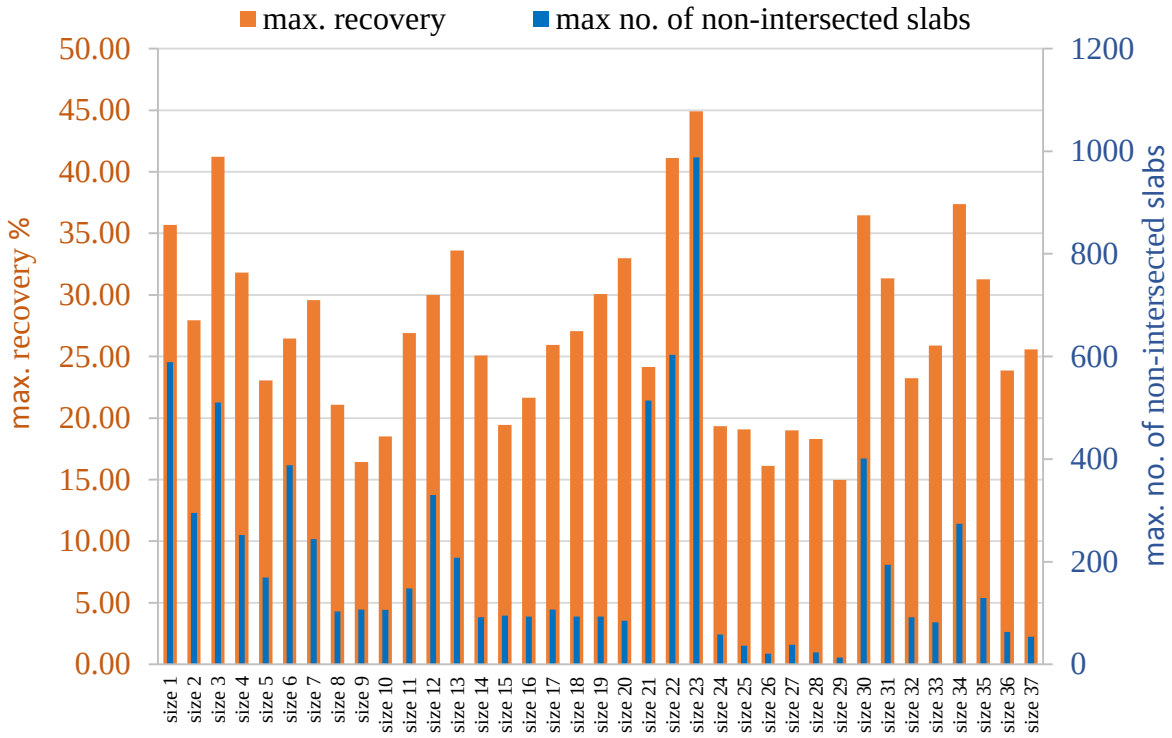

Figure 71: Graphical representation of the maximum recovery and maximum number of non-intersected slabs within all the sizes tested in SlabCutOpt.

Economically, neither the maximum recovery nor the maximum number of non-intersected slabs can be the most useful comparison indicator for the optimization results within a range of different sizes. When several sizes are considered, the total revenue calculated by Eq. (10) is a more effective comparison indicator to assess the optimum solution.

$$revenue = number\ of\ nonintersected\ slabs\ \times RMV\ per\ unit \quad (10)$$

Interestingly, as shown in Figure 72, the optimal (maximum) revenue was obtained from slab size No. 21 with a total value of 55.0 RMV. However, neither the maximum number of non-intersected slabs nor the maximum recovery ratio could be found in this slab size. Therefore, the final optimal economical solution (optimal maximum RMV), given by SlabCutOpt, for this block, was identified in slab size No. 21, at the cutting orientation parallel to plane XY – slab rotation 0° with a displacement: (dx = -0.11 m, dy = 0.04 m, dz = -0.01), and equally at the cutting orientation parallel to plane XY – slab rotation 90° with a displacement: (dx = -0.11 m, dy = 0.04 m, dz = -0.01). Logically, this was expected since said slab is square-shaped (30.5 cm x 30.5 cm), therefore, the slab rotation had no effect on the results. Figure 73 shows a 3D clip visualization of the final optimal economical solution (slab size No. 21).

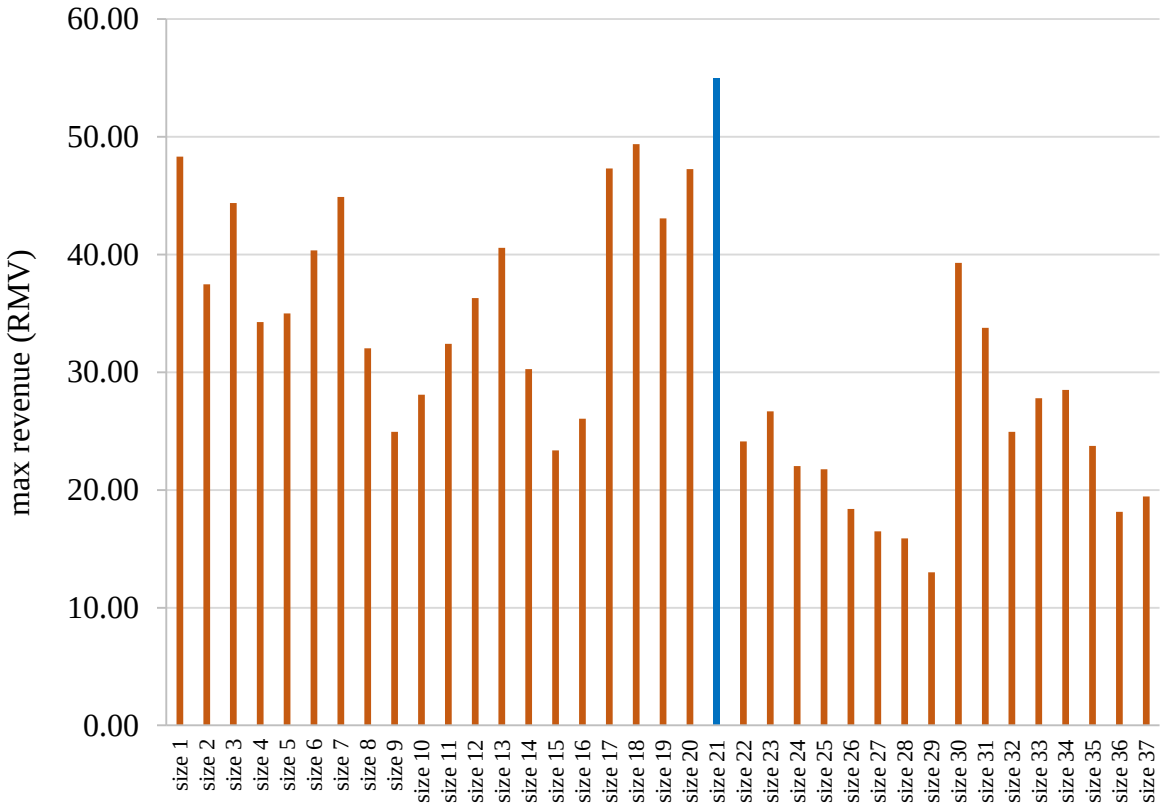

Figure 72: Graphical representation of the maximum revenue obtained for each slab size.

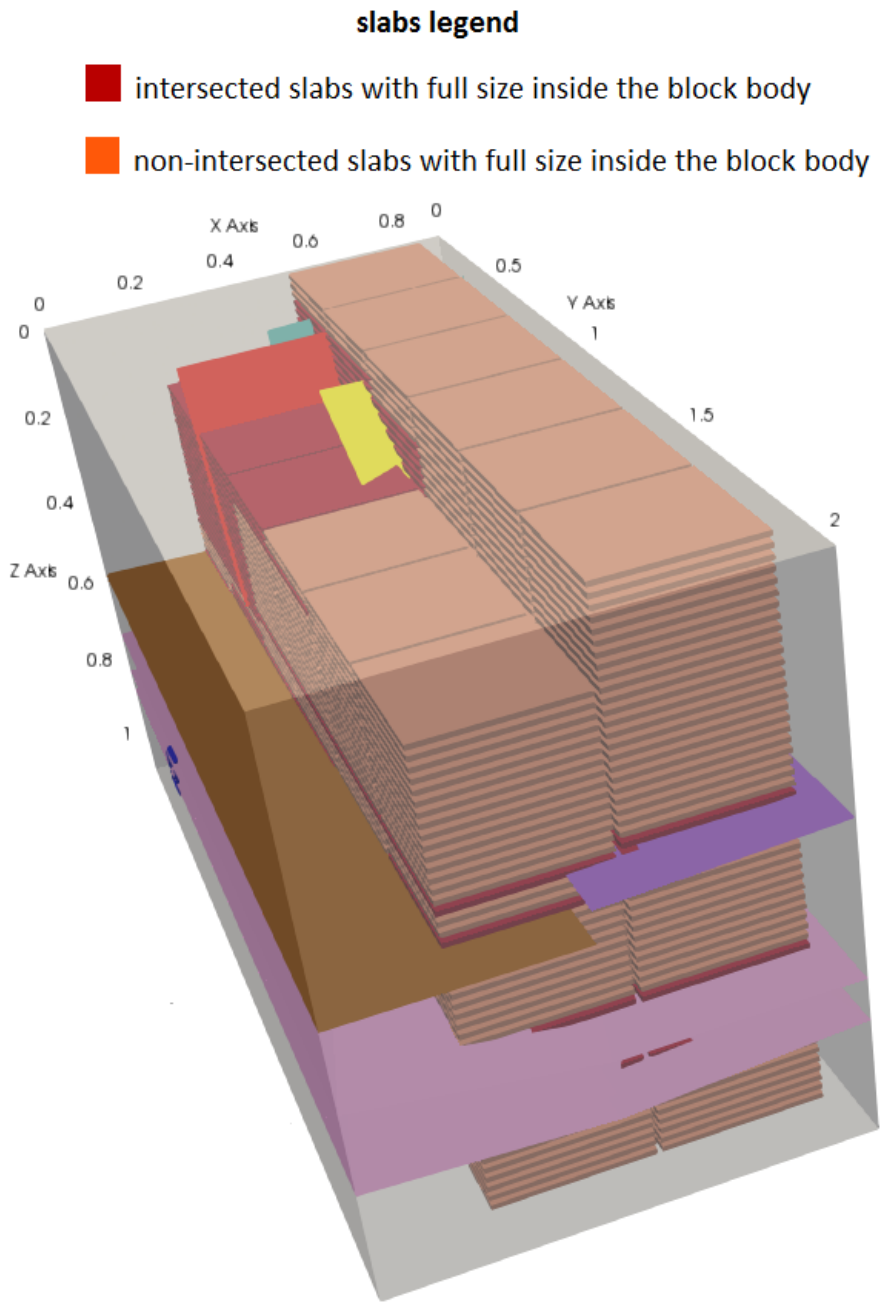

Figure 73: A 3D clip visualization of the final optimal economical solution, of SlabCutOpt, for the limestone block, by ParaView.

The surface area of tested slabs played a leading role in the run of SlabCutOpt. A strong positive linear correlation was found in the relationship between the surface area of slabs and the relative number of tested solutions output from SlabCutOpt (Figure 74). This is because the displacement domain is a function of the slab dimensions. The larger the size of slabs, the higher the number of tested displacements is.

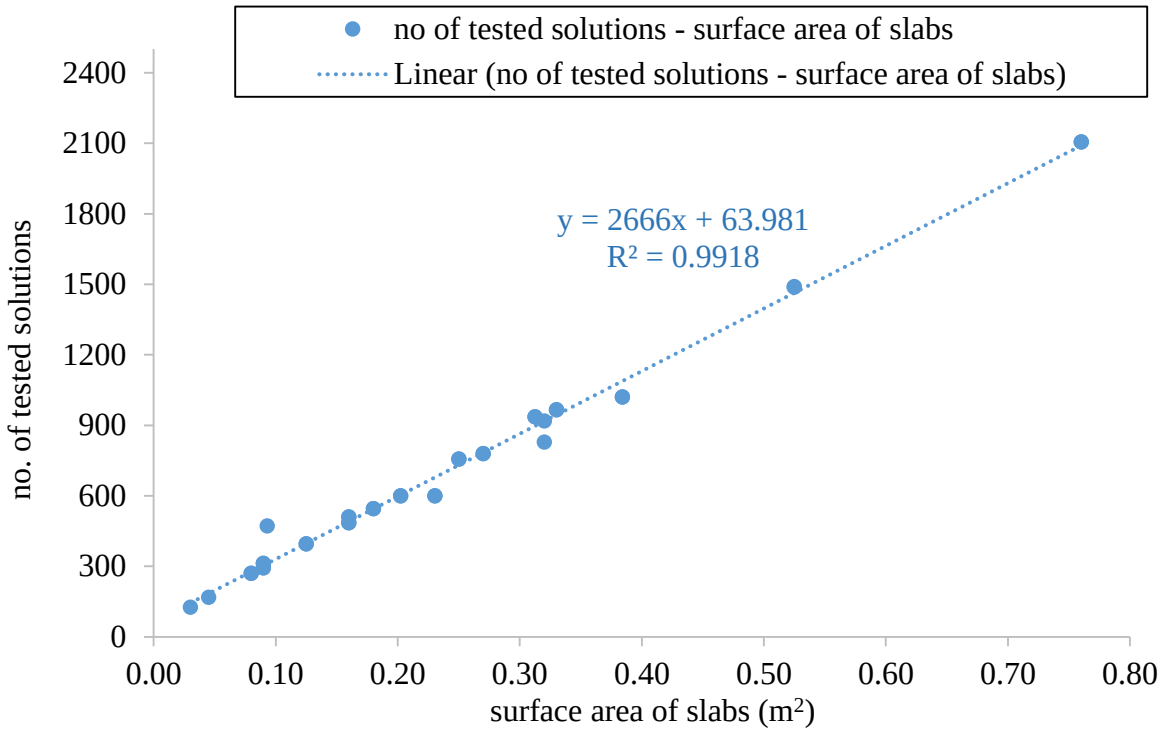

Figure 74: The strong linear correlation between the number of tested solutions and the surface area of slabs.

The surface area of the slabs tested played a leading role in the run of SlabCutOpt. The maximum number of non-intersected slabs for each slab size was strongly correlated in a negative power relation with the surface area of the slabs (Figure 75). Knowing the selling price for other non-tested slab sizes in SlabCutOpt, the chart or the correlation formula, in Figure 75, can be used to estimate their relative revenue. However, SlabCutOpt will still be needed in order to know the relative geometric design of the optimum cutting orientation-rotation of slabs.

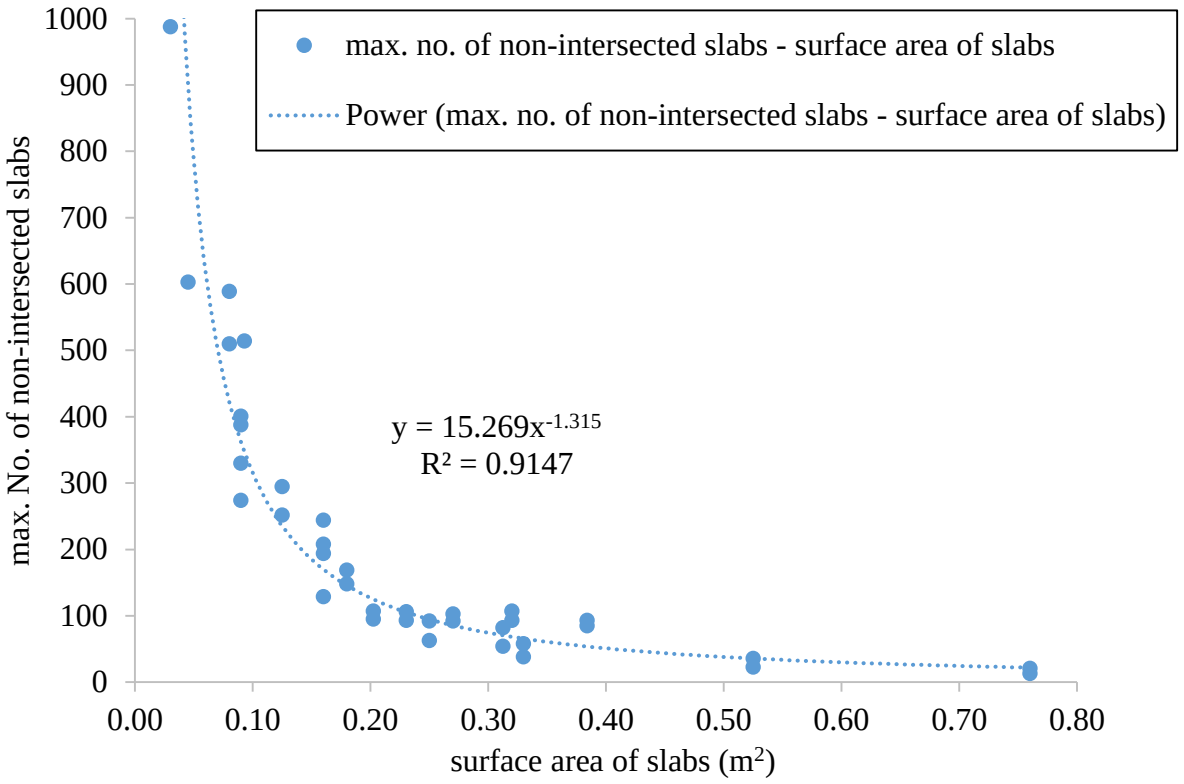

Figure 75: The correlation between the number of non-intersected slabs obtained for each size and the surface area of slabs.

The computation time of the SlabCutOpt run in this study to output the results (considering parameter write_vtu=1, see Appendix B), on a personal computer equipped with a 64-bit operative system Windows 10, a processor Intel i7-3770K CPU @ 3.5 GHz , and an installed memory (RAM) of 8.00 GB, was 23.0 minutes. The computation time strongly depends on Input/Output operations. Avoiding heavy operation of producing vtu files for each simulated cutting grid, the computation time was reduced to 37.0 seconds (considering parameter write_vtu=2, see Appendix B).

The use of the OpenMP library allowed to decrease the computation time by performing the computation simultaneously using several threads. To evaluate the performance of SlabCutOpt when using the OpenMP library, the computation of the optimization results in the case study was repeated, on the mentioned personal computer, using a number of threads between 1 (no multi-threading) and 8 with no VTU file writing (considering parameter write_vtu=0, see Appendix B), including the time of results printing (Figure 76). The computation performance of SlabCutOpt when using OpenMP was noticeable: the computation time halved when four

threads were used, followed by a slight decrease up to using eight threads. This is due to the fact that the hardware architecture is unable to execute more than four simultaneous threads at the same time. This is mainly because long-time execution functions, such as input/output file operations, are not called during the intersection computation of slabs, not activating hyper threading capabilities.

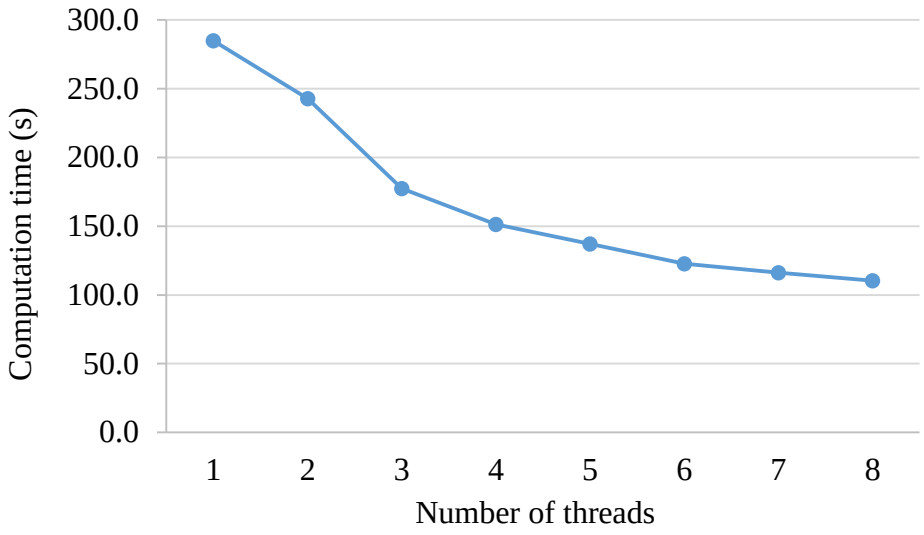

Figure 76: The performance of SlabCutOpt through a multi-threading computation of the optimization results in the case study.

6.5. Conclusions

When using a 3D deterministic model of discontinuities in an ornamental stone block (as presented in Chapter 4), several cutting scenarios (3D cutting grid patterns) of slabs can be tested to optimize the recovery ratio or the revenue of the block. We developed a 3D optimization algorithm to simulate several 3D cutting scenarios of slabs when discontinuities are modeled deterministically in an ornamental stone block. For each 3D cutting scenario simulated, the algorithm computed the number of non-intersected slabs - with discontinuities or the block body borders - which allowed calculating the recovery ratio. The optimization algorithm developed was successfully coded in the C++ programming language (the program named SlabCutOpt) with the possibility to visualize the results in 3D using a data visualization software package, such as ParaView.

For the investigated limestone block, among 37 different commercial-sizes of slabs tested, slab size No. 23 of dimensions 30.0 cm x 10.0 cm x 3.0 cm provided the optimum production

recovery solution. However, economic factors have to be considered to evaluate the optimal solution of the cutting grid pattern. For the investigated lime stone block, the slab size No. 21 of dimensions 30.5 cm x 30.5 cm x 1.0 cm provided the final optimal economical solution.

A negative power correlation was found between the maximum number of non-intersected slabs and the surface area of slabs. This negative power formula can be used to estimate the maximum number of non-intersected slabs for non-tested sizes of slabs in the block studied.

CHAPTER 7

Quarry Scale Optimization

7.1. Introduction and review

Fractures play a significant role in the exploitability of ornamental stone quarries. In particular, the increase of fracture sets number and the small the spacing of fracture sets, the exploitability of deposits are adversely affected. The exploitability of an ornamental stone deposit refers to the possibility of cutting non-fractured commercial-size blocks.

Rock mass fractures control the feasible exploitation and stability of benches of quarries. Fractures provide natural rock-break surfaces which consequently form natural rock blocks that cause production waste during exploitation. These blocks are named also by (Lu and Latham, 1999) as in-situ blocks and were defined as the resulting blocks from the intersection of discontinuity sets with different characteristics of spacing and orientation. The size of the in-situ block is mainly controlled by the spacing and number of discontinuities (ISRM, 1979). The profitability of an ornamental stone quarry can be increased by the reduction of waste and maximizing the bulk extraction volume of a fit commercial size block, which is the objective of this chapter. A fit block of ornamental stone can be defined as an extracted block without surfaces of fractures that may lead to disintegrating the extracted block during the handling or processing phases.

Several previous works presented geometric or stochastic methods to identify the geometry and quantify the volume of natural blocks for mining and geoengineering purposes (e.g. Cho et al., 2012; Elmouttie and Poropat, 2012; Turanboy, 2010; Turanboy and Ülker, 2008; Yarahmadi et al., 2015, 2014). The majority of these previous works were based on the traditional manual method of fracture detection which has well-known drawbacks (Assali et al., 2014; Kemeny and Post, 2003). It is worth mentioning that any 3D modeling of fractures from the manual method data assumes that fractures are infinite linear planes: deterministically this is not true.

The identification of natural rock blocks geometry can be useful for preliminary reserves estimation quantification in quarries particularly when calculation of the maximum largest cuboid (Ülker and Turanboy, 2009) or of the marketable block size (Mutlutürk, 2007) fit into natural rock blocks can be done. Mosch et al., 2011, developed a software package, named 3D-BlockExpert, which can identify the volumes of the natural blocks. 3D-BlockExpert can

generate a derived 2D section inside the rock body, from selected parallel two sections, to visualize the natural blocks geometry. This helps the program operator to optically determine the most suitable arrangement of different block sizes (Mosch et al., 2011; Sousa et al., 2017), inside a derived 2D section, to optimize the production which can be promising in cutting commercial block sizes from a large quarried block when economical and labor factors are considered. However, for bench scale quarrying, these approaches of natural blocks identification do not follow, in somehow, the quarrying logic, since the orientation of the quantified/ identified blocks may or may not be consistent with the usual cutting sequence/ strategy (continuous cutting direction for the same size of blocks quarried) in benches which is practically non-changeable for quite large areas. Moreover, these approaches model fractures as planes with finite persistence based on the data of the main fractures sets surveyed by the manual method which entails errors in identifying the natural blocks.

For production planning, the quality of the deposit needs to be assessed. Geostatistical methods could give evaluation indices for ornamental stone deposits (e.g. Taboada et al., 1999, 1997; Tercan and Özçelik, 2000), however, the geostatistical methods are still far from the production optimization point of view in this chapter.

Production optimization of ornamental stone deposits, in this chapter, considers finding the optimum cutting direction of blocks from benches of quarries, based on 3D deterministic fracture modeling or fracture mapping as well, aiming at maximizing the production recovery ratio and/or revenue when economic data are available. The approach in this chapter is different than those which find the optimal cutting direction based on geo-mechanical parameters of the deposit (Deliormanli and Maerz, 2016; Yarahmadi et al., 2017a). The referred production recovery in this chapter is derived from the concept in Eq. 9 and defined in Eq. 11. Production optimization requires deterministic-based optimization methods based on 3D deterministic fracture modeling or mapping. Stochastic data cannot give highly trusted results due to uncertainty.

$$recovery\ (\%) = \frac{volume\ of\ non-intersected\ blocks\ with\ full\ dimension\ inside\ the\ rock\ body\ studied\ x\ 100}{total\ volume\ of\ the\ rock\ body\ studied} \quad (11)$$

Optimization of ornamental stones production recovery was introduced in 2D, for the first time, graphically, by (Tomasic, 1994) who illustrated that the production recovery is controlled by the block size, the spacing of fractures, and the orientation of blocks. However, the graphical 2D application in the work of (Tomasic, 1994) was on a perpendicular profile along a working

bench and with considering different block sizes, which is not coherent with the actual quarrying applicability.

Regarding the previous 3D production optimization methods, the most noticeable contributions are the work done by (Fernández-de Arriba et al., 2013) and (Yarahmadi et al., 2017b). Fernández-de Arriba et al., 2013, developed a numerical optimization algorithm programmed in a software package using the C# programming language and named CUTROCK. This method is based on using the data (dip angle, dip direction, and spacing) of three fracture families, assumed persistent and continuous planes, to identify the volume of maximum block bounded in the natural block inside the spatial data of the three fractures families. A mesh of blocks with the desired dimensions is then generated in a parallelepiped form and inside the maximum block. The final aim of this method was to find the cutting direction of blocks, just inside the generated mesh, which optimizes the yield. Field studies of several works have shown that fracture families often occur in two or three prominent families and one or more minor families; in addition random joints may be present (Palmström, 1995). This refers to an expected error in the optimization result of this method with a limitation of non-workability in a case different than only three fracture families.

Yarahmadi et al., 2017b, improved the previous methods within two directions: (i) natural blocks identification and classification numerically and (ii) production optimization. Since this is the most recent and improved work, it will be briefly discussed in more details. This work was programmed in a software package, using the MATLAB environment, and named 3D-QuarryOptimizer. Firstly, natural block identification was improved by considering random discontinuities with finite persistence and fracture families while considering block shape factor. The block shape factor is a classification measure of the shape quality and was defined as the ratio of the surface area of a representative rectangular block (with the same volume as the given natural block) to the surface area of the natural block. This factor shows how much an irregularly shaped block is similar to a representative rectangular block but no indications to the 3D orientation/ inclination of the representative rectangular block was referred in the shape factor which is important for the quarrying suitability.

Regarding the optimization, 3D-QuarryOptimizer performs optimization within two scales: (i) analysis of quarrying direction on a large scale, based on the main fracture families' data, and (ii) cutting the interval in a bench face on a small scale (Large Volume Block, LVB). LVB

(named in Italian language: *bancata*), is loosened by means of primary cuts, from which commercial sizes of blocks are cut. On the small scale optimization, a genetic algorithm was used, in 3D-QuarryOptimizer, to find the best variable cutting intervals to cut blocks from a large block. This is theoretically an innovative optimization, however, practically the cutting intervals in a large block and in a large bench scale usually occur with fixed distances.

On the other hand, the objective of the large-scale optimization algorithm, in 3D-QuarryOptimizer, is to maximize the volume of the extracted blocks bounded in a mesh of blocks. Accordingly, several blocks' classes of different volumes and shapes can be analyzed to calculate the beneficial value of each class. However, the developed optimization algorithm, presented in this chapter, can find the optimum commercial-size of block, directly extracted from a bench, which maximizes the recovery concept in Eq. 11 and the revenue respecting the selling prices of several tested sizes when economic data are available. As shown in Chapter 6, the economical optimization is a function of the selling price of a commercial-size product. As given by (Reina and Loi, 2015) the blocks are classified into three classes, based on the rock material and the geometric shape: (i) first grade blocks that have commercial dimensions with six very regularly-shaped sides (known as blocks); (ii) second grade blocks whose one or more faces are not regular (called "half blocks"), (iii) and third grade blocks which do not have a regular shape (known as "unformed"). Hereby, in this chapter, the optimization targets the first grade blocks. And moreover, the final result of the quarrying optimization approach, in this chapter, can be applicable following the current quarrying routine.

The presented quarrying optimization algorithm, in this chapter, aims at decreasing the gap between the previous methods and improving the optimization results considering the practical aspects. The main features of the presented optimization algorithm are listed as follows:

- The algorithm can work using any source of fracture data survey (GPR, manual method, laser scanner, aerial photogrammetry...etc.) just after describing the modeled fractures in PLY files, however, the results uncertainty can be minimized when using 3D deterministic fracture model from GPR data (recommended).
- No natural block identification algorithms is required, consequently, there is no limitation to the number of the fracture families.
- The algorithm can be applied to a large scale bench or to a small scale of LVB.
- The wasted material caused by the cutting (quarrying) method is considered in the algorithm.
- Providing an option of dividing the tested area into several sub-divisions of quarrying zones where the optimum cutting directions may vary.

- Introducing the horizontal displacements of the cutting grid of blocks as an optimization parameter.

7.2. Method

7.2.1. Development of a 3D brute force attack quarrying-logic algorithm

Identification and optimization of the cutting zone of non-fractured blocks in a bench can be optimally carried out after accurate deterministic modelling of fractures. Planning the cutting zones of non-fractured blocks can sustainably decrease the amount of waste. If fractures are typically modelled as three dimensional planes, there will be a potential risk of wasting material during the quarrying operation. While modelling fractures as irregular 3D surfaces as close as possible to reality, as presented in Chapter 4, can lead to decreasing waste. Then, an optimization algorithm can be used to find the optimum cutting direction that maximizes the number of non-fractured blocks and or production recovery, with the required block size.

Geo-structurally, the most dangerous parameter for quarrying is not the orientations of fractures or number of sets but the spacing between fractures of each set. The larger the spacing of a fracture set is it, the larger is the amount of extracted commercial-size non-fractured blocks.

The quarry scale optimization algorithm, presented in this chapter, is a modification to the block scale optimization algorithm, having adapted it to the quarrying logic. It contains the same concept of the 3D cutting grid domain. The slabs dimensions is the blocks dimensions and the surveyed block body is the bench body herein. The thickness of the saw is replaced herein by the volume of the lost material due to quarrying named in the algorithm material-lost-by-quarrying.

The main adaptions or modifications on the block scale optimization algorithm done for the quarry scale optimization algorithm are:

- Only the horizontal rotation is considered (ψ) which is the cutting/ quarrying direction in the range from 0.0° to 180°, see Figure 67.
- No vertical displacement of the 3D cutting grid of blocks is considered (dz).
- The tested quarrying area can be concave or convex polygons or with regular geometric shape.
- As an option, in case of large scale optimization, the main tested quarrying area can be divided into sub-divisions of quarrying zones with equal areas. The sub-divisions are identified in the algorithm by (m_x=i,m_y=j), where i is the number of the sub-divisions in the X direction and j is the number of the sub-divisions in the Y direction. For example, if a tested area is solved in the algorithm using (m_x=2,m_y=2), this means that

the area contains four sub-divisions of quarrying zones defined by (i=1,j=1), (i=2,j=1), (i=1,j=2), and (i=2,j=2). If (m_x=1,m_y=1), the algorithm will work on a single tested area without sub-divisions.

7.2.2. Software development (BlockCutOpt)

Similarly to SlabCutOpt, the algorithm was coded using the C++ programming language with workability in the environment of parallel processors to speed the computation process. The developed software package was named "BlockCutOpt" derived from the aim of the program which is "Block Cutting Optimization". The input and output files of BlockCutOpt have the same features of the input and output files in SlabCutOpt, considering some differences in the file containing the input parameters, named BlockCutOpt.par. In addition, in case of using the sub-division of the tested area option, the Results.log file of BlockCutOpt list the results separately for each sub-division zone.

7.3. Case studies and results

7.3.1. Limestone quarry, Italy - GPR data

7.3.1.1. Input data

BlockCutOpt was applied to the bench of the limestone quarry where fractures were modeled based on the developed fracture modeling approach, as presented in Section 4.2.1. The objective of this case study was to investigate the effect of modeling fractures as 3D surfaces on the production optimization results. In this case study, only one commercial size of block will be tested in BlockCutOpt. The revenue optimization was not considered in this case study because of confidentiality of the prices of commercial sizes blocks. By personal communication with the quarry technical manager, he reported that the preferred quarried block dimensions, from this quarry, are 3.0 m length, 2.0 m width and the thickness of the block is limited to the thickness of the strata. In this case study, the surveyed bench had four strata (a, b, c, and d), see Section 4.2.1.4. For each stratum, the referred block size with its relevant thickness was tested in BlockCutOpt to find the solutions for optimum recovery and maximum number of non-intersected blocks.

In this case study, the cutting direction will be tested within angles interval of 3.0° and using a horizontal displacements of 0.5 m in the X direction and the Y direction for the 3D cutting grid of blocks. The thickness of the material-lost-by-quarrying was used as 5.0 cm. See Appendix H as an example for an input file for this case study considering the non-division of the tested area.

7.3.1.2. Optimization results

The results of applying BlockCutOpt to the tested commercial size block provided that the maximum number of non-intersected blocks were found variable with the cutting direction, and within the displacements of each cutting direction tested as well. This is mainly due to the modeled 3D surfaces of fractures which change the results between strata. A graphical representation for the results of strata a, and d is shown in Figure 77 and visualized in Figure 78. The consideration of the material-lost-by-quarrying can be also observed in the zooming part of Figure 78. The intersected blocks of stratum a were not visualized in Figure 78 for better visualization of stratum d. The time taken by BlockCutOpt to output these results, for the four strata, was 11 minutes, considering write_vtu=2 in the PAR file, using a computer of the following specifications: 64-bit operating system Windows 7, processor Intel(R) Core (TM) i5-4460 CPU @ 3.20 GHz, and installed memory (RAM) 8.00 GB.

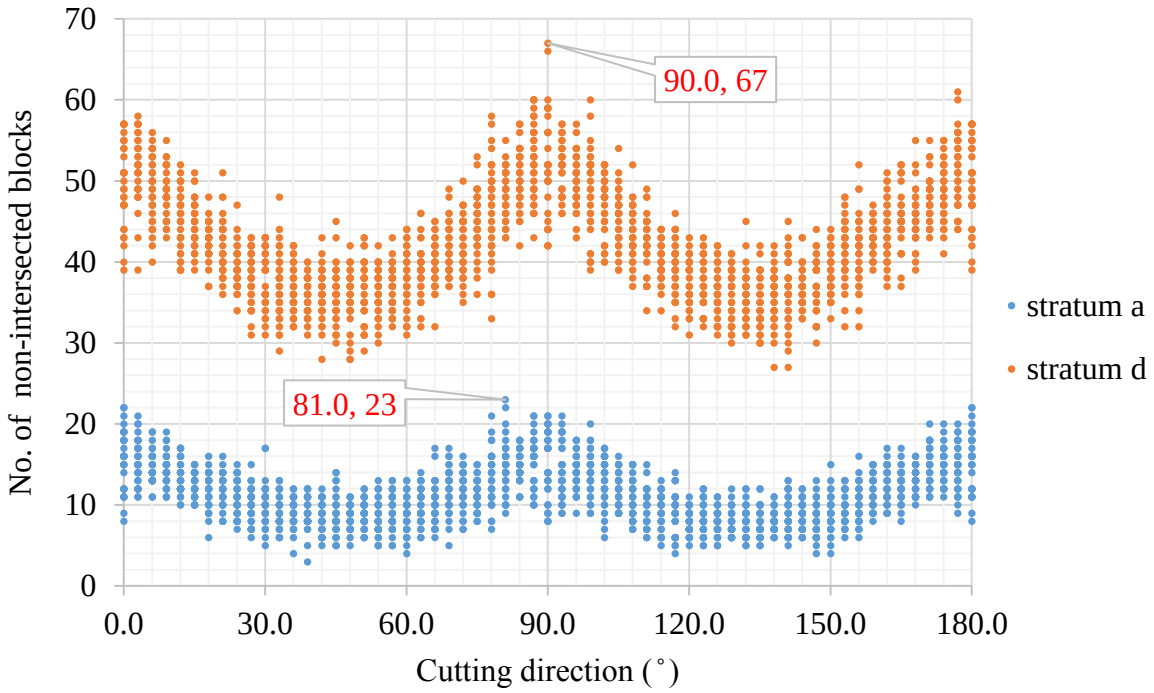

Figure 77: The optimization results of Stratum a and Stratum c.

Considering the final optimum solution of the maximum number of non-intersected blocks require the comparison with another sizes and selling prices, as presented in Chapter 6, when data is available. Table 20 summarizes the optimization results of this case study. Following the optimization results provided in Table 20, the total number of non-intersected blocks in the bulk volume of the bench is 150 blocks leading to a bulk recovery ratio of 11.4 %. It is worth

mentioning that the cutting direction used in this bench was 0.0 ° (traditionally fixed for all the strata) which is not consistent with the optimization results.

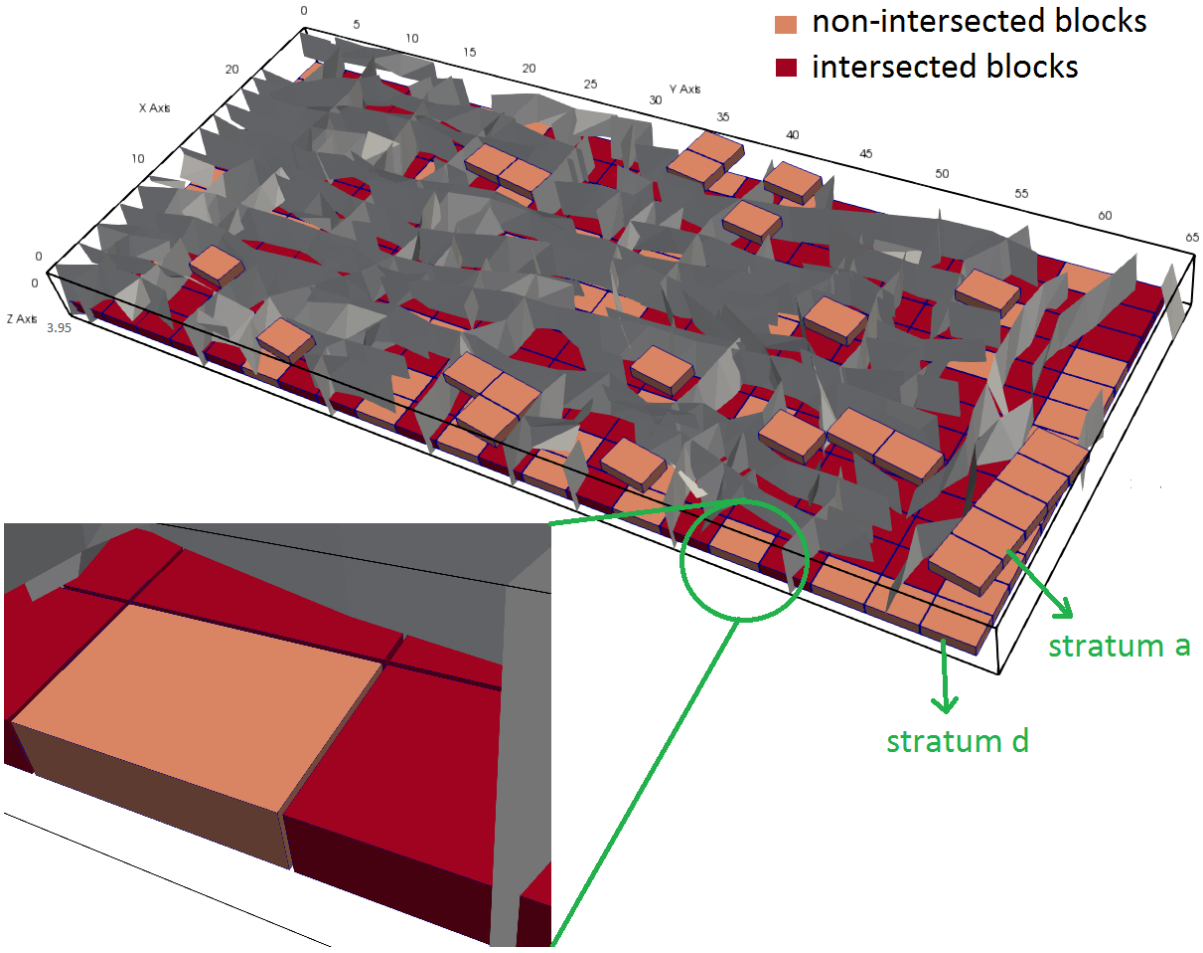

Figure 78: 3D visualization of the optimum solutions, for strata a and c, visualized by ParaView.

Table 20: The summarized optimization results for each stratum.

stratum	max. No. of non-intersected blocks	max. recovery (%)	dx (m)	dy (m)	cutting direction (˚)
a	23	7.86	-0.51	-1.01	81.0
b	23	7.68	-1.01	0.99	90.0
c	37	12.65	-1.01	0.99	90.0
d	67	22.91	0.99	0.99	90.0

7.3.2. Granite quarrying area, Portugal - aerial photogrammetry data

7.3.2.1. Input data

The objective of this case study was to investigate the applicability and workability of BockCutOpt in a very large scale quarrying area of huge amount of data for the target of long term optimization. In particular, when dividing the main area of exploitation into sub-zones, that may have different cutting directions, can be possible and feasible.

The author obtained a written approval from the main author of (Sousa et al., 2016) to use the presented fracture map (Figure 79) of a granite quarrying zone in the referred paper. This map represents a regional fracturing mapping, obtained by aerial photogrammetry interpretation, of a granite quarrying zone. The granite of the studied zone is medium-grained, named Mondim de Basto granite, and sometimes with feldspar mega-crystals. This granite intruded metasedimentary rocks presumably of Lower Silurian to Lower Devonian age (Sousa et al., 2016).

The total area under study is 5650.6 X (m) *x* 5675.8 Y (m). The main border of the studied zone was assumed to be the same border of the map in Figure 79. The revenue optimization could not be considered in this case study because revenue optimization requires the selling prices of the final products: commercial-sizes blocks. Since this case study is a very large scale area, the optimization results could be provided within the two possible options: finding the optimum solutions with and without dividing the tested area.

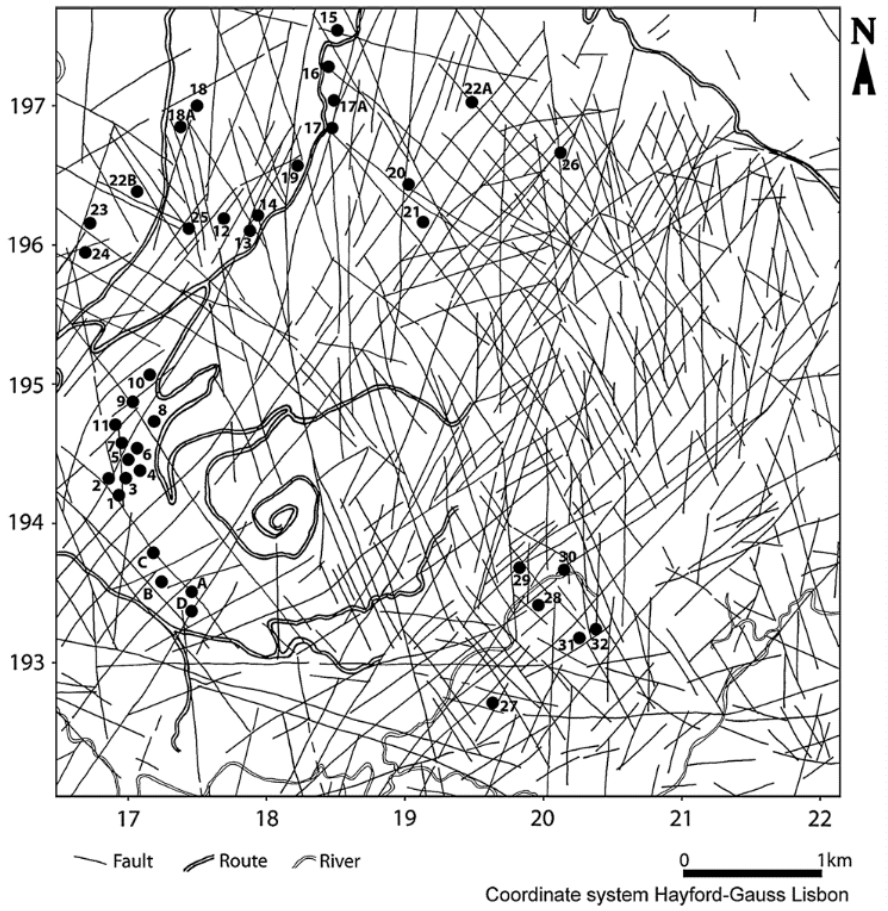

Figure 79: Regional fracturing pattern in the studied area (the black dots represent the locations of the acquired data). The figure and the caption were copied – with a permission – from (Sousa et al., 2016).

To adapt the fracture data of this map to be readable by BlockCutOpt, the fracture traces were picked and exported automatically to an excel sheet using the AutoCad add-on utility "click2xls" which facilitated the transformation of the fracture data to a PLY file, in different local coordinates. The resulting 3D map is visualized in Figure 80. It is assumed that the whole fractures are vertical, persistent and continuous planes. It is worth mentioning that no horizontal fractures data were detected or considered for the map of the tested quarrying zone. The fractures data were transformed to a PLY file keeping their original coordinate system.

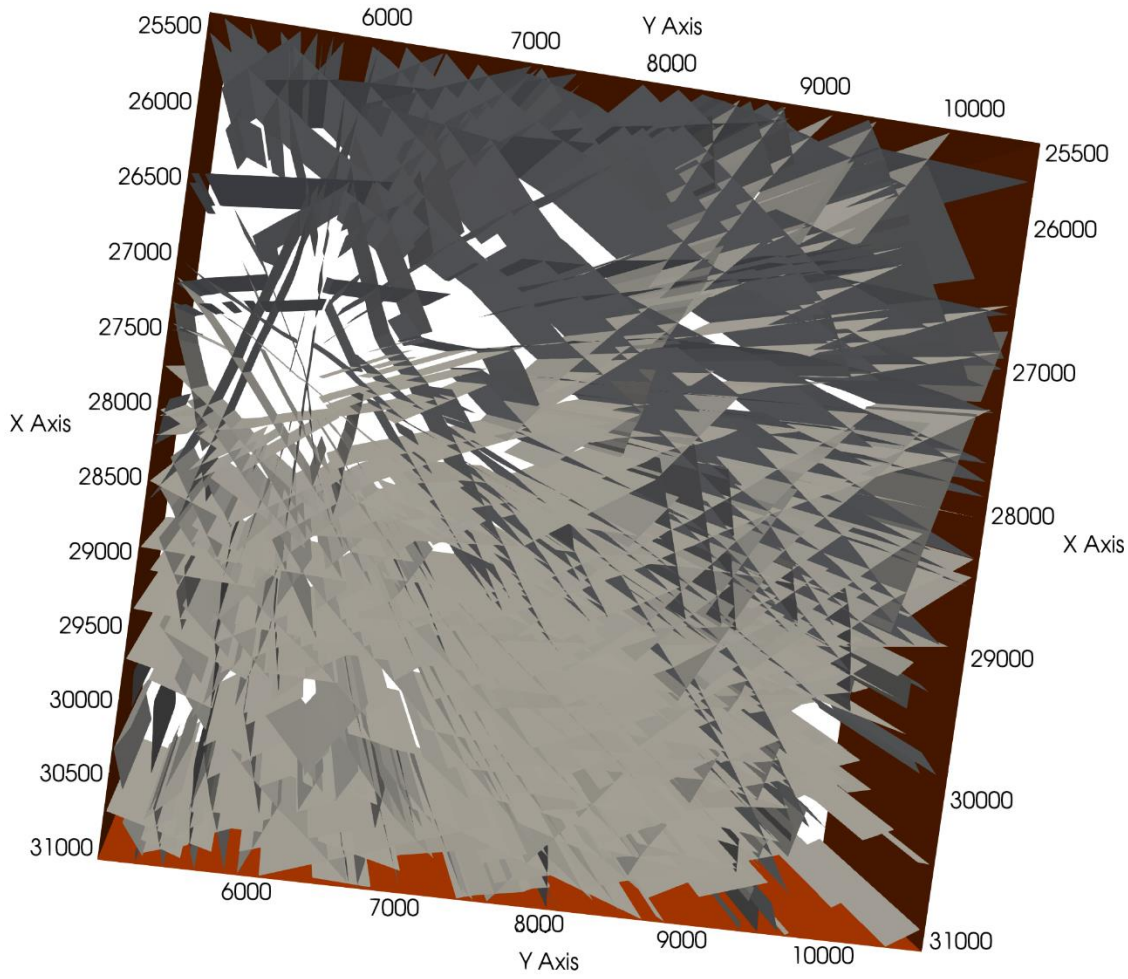

Figure 80: The 3D oriented top-view fracture model of the map in Figure 79, visualized by ParaView.

For the application of BlockCutOpt in this case study, the tested size of block was the LVB. This is the most common size cut particularly in marble and granite quarries. The volume of LVB is usually in the 1000s of m^3 range: length of 20.0-30.0 m, width of 9.0-12.0 m, and height of 6.0-7.0 m (Ashmole and Motloung, 2008). The dimensions of a large block are generally determined considering the machinery limitations. However, in this case study, and since there are no more available data, the author simulated a size of LVB that satisfies the referred dimensions and volumes given by (Ashmole and Motloung, 2008). The simulated tested size of LVB has a length of 21.0 X(m), a width of 9.0 Y(m), and a height of 6.0 Z(m), providing a volume of 1080.0 m^3.

In this case study, the cutting direction will be tested within angles interval of 3.0° and using a horizontal displacements of 7.0 m in the X direction and 5.0 m in the Y direction for the 3D

cutting grid of blocks. The thickness of the material-lost-by-quarrying was used as 5.0 cm. See Appendix I as an example for an input file for this case study considering the sub-division of the tested area.

7.3.2.2. Optimization results

Firstly, the results will be presented herein considering the non-division of the tested area. The results of applying BlockCutOpt to the tested size of LVB is graphically presented in Figure 81. Consequently, the recovery ratio was found variable with the cutting direction. For each angle of cutting direction the algorithm simulated solutions considering different displacements of the 3D cutting grid. The variability range of recovery ratio was limited (80.40-83.29 %). The high recovery ratio was expected, in this case study due to the small surface area of LVB tested compared to the area of the quarrying zone and the limitation of the fracture detection method used which provided the main regional fracturing. However, the maximum number of non-intersected LVBs was found at the cutting direction of 93.0˚, at a displacement of dx = -10.01 m and dy = 0.49 m, providing the maximum recovery of 83.29 %. A visualization of the maximum number of non-intersected LVBs solution is given in Figure 82. As shown in Figure 82, the 3D cutting grid of LVBs is orientated towards the related cutting direction of the optimum solution (93.0˚). In this case study, the number of the modeled triangles of fractures was 2924 and the number of the LVBs in the 3D cutting grid was 363776. The time taken by BlockCutOpt to output these results was 26 hours, considering write_vtu=2 in the PAR file, using a computer of the following specifications: 64-bit operating system Windows 10, a processor Intel i7-3770K CPU @ 3.7 GHz , and an installed memory (RAM) of 8.00 GB.

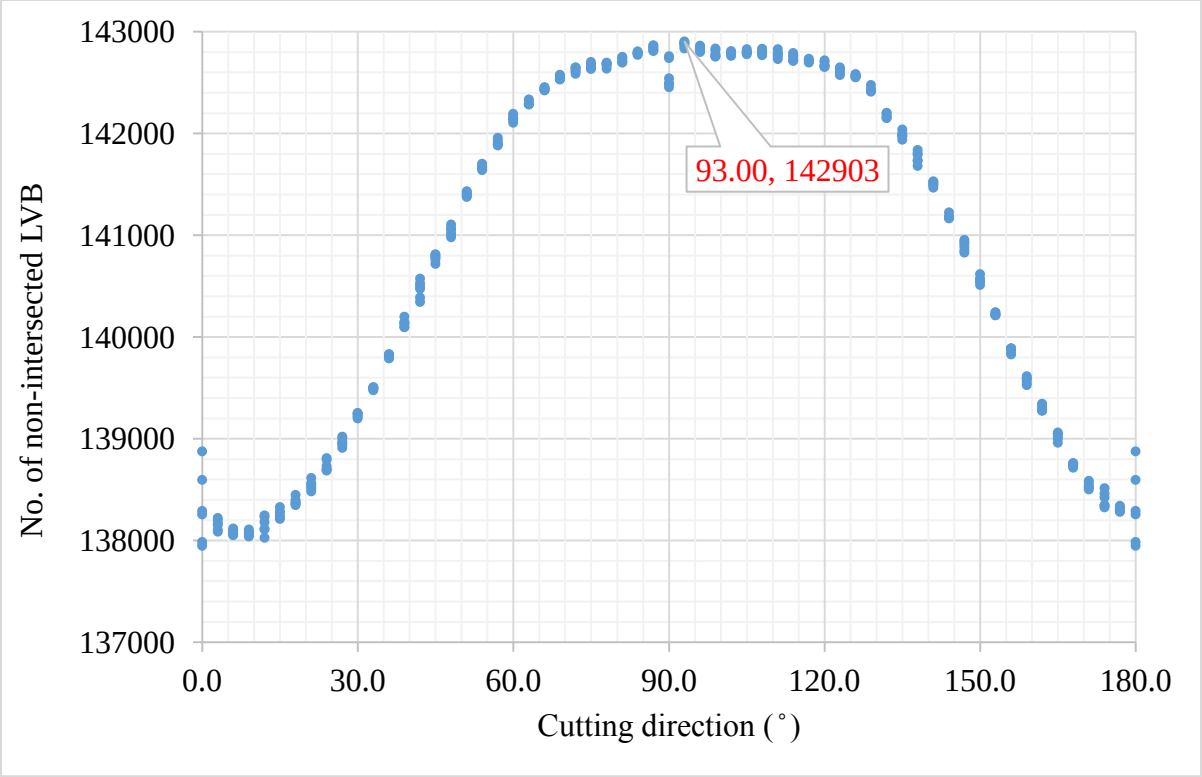

Figure 81: The optimization results of the tested size of LVB, without sub-division, highlighting the optimum solution.

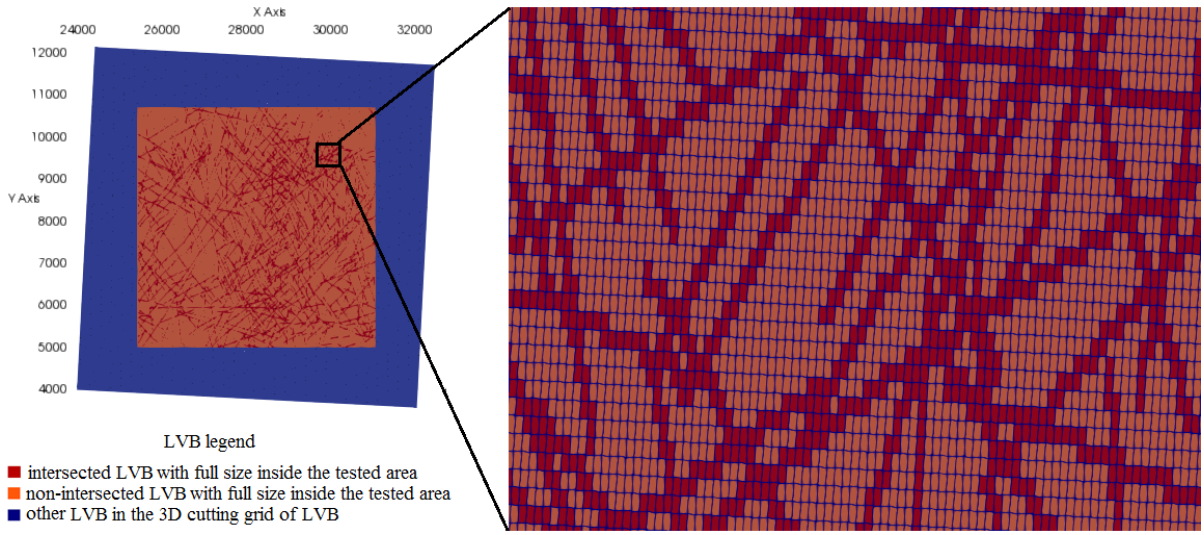

Figure 82: 2D visualization of the optimum number of non-intersected LVBs solution, without sub-division, visualized by ParaView.

Considering the sub-division of the tested area, firstly, the whole tested area was divided into 3 sub-divisions of quarrying zones in the X direction and 2 sub-divisions of quarrying zones in the Y direction (m_x=3,m_y=2), leading to a total of 6 sub-divisions of quarrying zones. The

results are summerized in Table 21 for the 6 sub-divisions of quarrying zones. From the results in Table 21, it can be shown that the maximum number of non-intersected blocks for the sub-division zones are found at different displacements, even if the optimum cutting direction of 90.0 is almost the predominant one. The total number of maximum non-intersected LVBs, in all the sub-division zones, was 142701: less than in the without division test, providing a total optimum recovery, in all the sub-division zones, of 83.17 %. It is worth referring that the optimum cutting direction without sub-division (93.0˚) was not found in any optimum solution of the sub-division zones.

Table 21: The optimization results for each sub-division quarrying zone (m_x=3,m_y=2).

i	j	max. No. of non-intersected LVBs	dx (m)	dy (m)	cutting direction (˚)
1	1	25104	-3.01	-4.51	129.0
1	2	24718	-3.01	-4.51	90.0
2	1	21840	3.99	-4.51	90.0
2	2	22713	3.99	0.49	90.0
3	1	23744	-3.01	-4.51	90.0
3	2	24582	-3.01	0.49	90.0

Increasing the number of the sub-division zones can decrease the maximum number of non-intersected blocks since the borders of the sub-division zones were acting as fractures. However, a noticeable variation of the optimum cutting direction for each sub-division quarrying zone is expected. This is logically obvious, however, BlockCutOpt can quantify and graphically visualize the results (using ParaView). A further test of increasing the sub-division zones was performed for (m_x=6,m_y=3). The results are visualized in Figure 83 and summarized for each sub-division quarrying zone in Table 22.

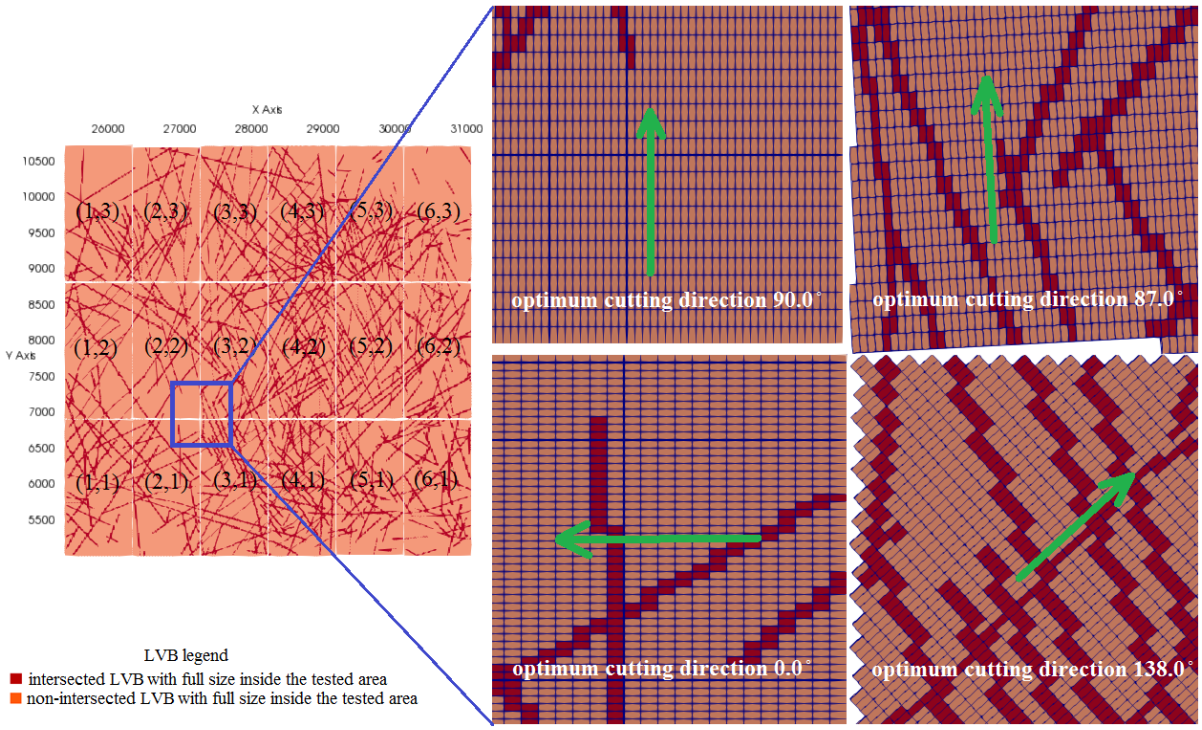

Figure 83: 2D visualization of the optimum number of non-intersected LVBs solution, with sub-divisions of (mx=6,my=3), visualized by ParaView.

Table 22: The optimization results for each sub-division quarrying zone (m_x=6,m_y=3).

i	j	max. No. of non-intersected LVBs	dx (m)	dy (m)	cutting direction (°)
1	1	8123	-10.01	-4.51	0.0
1	2	8219	-10.01	-4.51	132.0
1	3	8514	-10.01	-4.51	0.0
2	1	8294	-10.01	-4.51	0.0
2	2	8374	-3.01	0.49	90.0
2	3	8076	-3.01	-4.51	90.0
3	1	7403	-3.01	0.49	138.0
3	2	7672	-3.01	-4.51	87.0
3	3	7971	-3.01	0.49	90.0
4	1	6956	-10.01	0.49	138.0
4	2	6970	-3.01	0.49	90.0
4	3	7295	-3.01	0.49	132.0
5	1	7870	-10.01	-4.51	90.0
5	2	7515	-10.01	0.49	90.0
5	3	7761	-10.01	0.49	90.0
6	1	8008	-10.01	-4.51	0.0
6	2	7837	-3.01	0.49	90.0
6	3	8854	-10.01	0.49	90.0

It was noticed that the total number of non-intersected LVBs decreased (Table 23) with increasing the subdivision zones. This is because the borders of the sub-division zones acted as additional synthetic fractures. The sub-division technique can provide better bulk recovery impact, in case a large area of quarrying shall be divided into independent sub-zones for business or geographic reasons. Given that, the optimum solution found for each sub-division zone is the one providing the optimum recovery for that zone.

Table 23: The variation of the total optimization results with and without sub-division.

	without sub-division	sub-division (mx=3,my=2)	sub-division (mx=6,my=3)	sub-division (mx=9,my=4)
optimum recovery (%)	83.29	83.17	82.60	82.04
optimum No. of non-intersected LVBs	142903	142701	141712	140767

7.4. Conclusions

The developed quarry scale optimization algorithm allowed to find the optimum cutting direction in benches that maximized recovery ratio or the number of non-fractured blocks or LVBs. The developed algorithm was successfully coded in the C++ programming language with the possibility to visualize the results in 3D using ParaView. The programed algorithm was named BlockCutOpt.

BlockCutOpt was implemented into two case studies. The first one was a limestone bench where fracture were modeled using GPR and the developed approach. The results showed that modeling fractures as 3D surfaces plays a significant rule in the optimization results. The optimum cutting direction of blocks as well as the displacement of the cutting grid of blocks were found variable within the different strata of the bench in this case study.

The second case study was a large scale area of granite quarrying area where fractures were mapped by aerial photogrammetry. BlockCutOpt showed its ability to work within a huge amount of data in large scale. In this case study, the optimization was performed for testing a a Large Volume Block (LVB) from which commercial-size blocks cut. Therefore, the results in this case study is limited to a LVB size and further detailed mapping or modeling of fractures is required for more accurate results. In this case study, the results showed that, the option of sub-division of the tested area is quite useful, in case a large quarrying area, shall be divided to sub-divisions, for business or geographic reasons. The optimum cutting direction was found

variable within the sub-divided zones. Increasing the number of the sub-divided zones can increase the variability of the optimum cutting directions and the cutting grid displacements that maximize the recovery for independent sub-division zones.

The final optimal economical solutions could not be provided in the results due to lack of the selling prices data of blocks particularly for the case study of the limestone quarry. However, as presented in Chapter 6, it is believed that knowing the selling prices of different commercial-sizes of blocks, the optimization results will interestingly behave.

CHAPTER 8

Conclusions and Recommendations

The thesis presented an integrated work between fracture detection and modeling using GPR and their application to quarrying. In Chapter 3, the investigation of the use of a low frequency GPR antenna was presented leading to promising results for the preliminary evaluation of a sandstone deposit. The low frequency antenna could detect large-aperture size of fractures at a relatively large depth which was useful for large scale deposit evaluation. From the field experience of the use of a low frequency GPR antenna, it is highly recommended to design a 3D intensive survey grid to, in somehow, compensate the subsurface details. A combination between the rock laboratory tests and the GPR results allowed the author to validate the GPR interpretations, and moreover, to classify the deposit into different quality categories based on the physico-mechanical properties and the fracture status obtained from the GPR survey.

In Chapter 4, a new 3D deterministic fracture modeling approach was developed to model fractures either as 3D planes (FISA) or 3D surfaces (FITA) based on fracture detection from GPR survey. The presented fracture modeling approach enhanced the previous deterministic methods of modeling fractures based on GPR survey through improving the deterministic accuracy level. Modeling fractures as 3D surfaces as close as possible to reality is quite significant for the objective of production optimization as presented in Chapters 6 and 7. Moreover, a preliminary quantitative evaluation-based fracture index, based on GPR data, was proposed in the thesis. The fracture index can be used in evaluation the quality of the rock mass and for scheduling the production. However, further improvements such as extending the index in more detailed 3D portions of the rock body and including geologic and economic factors are recommended for future development of the fracture index.

The developed fracture modeling approach was successfully implemented in further two case studies. The first one was in a large scale bench of a limestone quarry where a 3D deterministic model of fractures was obtained. The second one was a commercial-size ornamental limestone block in which a 3D deterministic model of fractures, based on GPR survey, was developed as the first application of this kind, up to the best of the author's knowledge. In this limestone block, small-size aperture out-cropping and hidden discontinuities could be detected using a 700 MHz GPR antenna. The fracture models obtained from these two case studies were used as input data for quarrying optimization, as presented in Chapters 6 and 7.

The limitations of the proposed fracture modeling approach are mostly the common limitations of GPR. The limitations of the proposed method can be listed as follows: (1) the surveying area should be suitable for the GPR survey: accessible, flat, with a reasonable inclination angle of the surveyed surface; (2) the size of the detected fractures is controlled by the antenna frequency, since with low frequency antennas, small or closed fractures do not show up in radargrams well; (3) antenna frequency also controls the penetration depth, closed or small fractures can be detected with the use of high frequency antennas but with limited penetration depth; (4) the operator's experience and skill control the quality of the GPR signal processing and data interpretation; (5) GPR survey is fast, but other elements in the methodology consume time such as fracture modeling formulations, for this point, specifically, it is recommended to automate the phase between detection and coding fractures in PLY files directly in the GPR programs of signal processing.

Using a wide range of GPR antenna frequencies can give a compromise solution for the problem of penetration depth and resolution: nowadays, for example, dual-frequency antennas are available. The time consuming issue of GPR survey can be tackled by surveying large areas, since it is expected to consume almost the same amount of time, as presented in Section 4.2.1. To increase the deterministic accuracy level of fracture modeling, minimizing the spacing between parallel survey lines is recommended. The developed fracture modeling approach can be used in different rock engineering applications, when suitable GPR surveying conditions exist, not only for the purpose of evaluating and production optimization of quarries, but also, for example, to collect structural data to be used in rock slope stability analyses and the design of underground structures.

The accurate estimation of the dielectric constant is an important parameter for accurate detection of subsurface anomalies at true depth and consequently for a high deterministic accuracy level of a fracture model. Currently, the "depth to a known reflector" method is the most recommend method when it is applicable in-situ, particularly for rock mass media, as done in Sections 4.1.2.3 and 4.2.2.3. However, even the "depth to a known reflector" method can only provide a single representative bulk value of the dielectric constant for the rock mass. This is not consistent with the typical heterogeneous discontinuous nature of rock masses which are characterized by random behavior of dielectric properties that entails errors in the detected depth of anomalies (such as fractures) when a single bulk dielectric constant value is

used. This viewpoint was validated by the developed in-situ GPR test and propagation velocity model applied to a bench of a sandstone quarry, as presented in Chapter 5. The results showed that the dielectric constant varies within wither a macro or micro scale in 3D or even in 2D. Currently, almost all the programs of GPR signal processing provide the use of a single dielectric constant value for the surveyed body, when it is known. Therefore, it is recommended to set up the developed method in the programs of GPR signal processing which can be useful for GPR applications that require high accuracy of detecting anomalies at true subsurface depth.

For quarrying production optimization, the thesis presented two algorithms to optimize the production/ revenue within two scales: the quarry scale and the block scale. The quarry scale algorithm aimed to optimize the production of blocks cut from benches of quarries, whilst, the block scale optimization aimed to optimize the production of slabs/ tiles cut from commercial size blocks. The optimization algorithms are based on 3D modeling of fractures. The optimization algorithms work with input data of fractures, stored in the PLY file format, detected by any method.

On the block scale, an innovative 3D geometric optimization algorithm was developed and programmed in a software package named SlabCutOpt, as presented in Chapter 6. The developed algorithm was applied on a commercial-size limestone block where fractures were modeled by the developed fracture modeling approach. SlabCutOpt could give the optimum design of 3D cutting grid for each slab size of different 37 sizes tested, considering the environmental (maximum recovery) and economical (maximum revenue) aspects. The results showed that for each slab size the recovery ratio highly varies with the change of the cutting orientation and slab rotation and within the displacements. It was found that the final optimal solution has to mainly consider the slab size which provides the maximum revenue, based on the selling prices data of the different slab sizes tested. For the tested limestone block, it is worth mentioning that the slab size of (30.5 cm x 30.5 cm x 1.0 cm), which provided the optimum revenue, didn’t provide the maximum production recovery solution. The results showed numerically and graphically that there was a strong correlation between the maximum number of non-intersected slabs and the surface area of slabs. For future work, it is recommended to perform a field comparison study between the results obtained from SlabCutOpt and the results of cutting slabs in a processing plant.

On the other hand, on the quarry scale, a 3D quarrying optimization algorithm was developed and programmed in a software package named BlockCutOpt, as presented in Chapter 7. The developed algorithm improved the previous optimization methods in literature through providing new features, for finding the optimum cutting direction of blocks, such as the horizontal displacement of the cutting grid, considering the material lost due to quarrying, and the sub-division of a tested area. BlockCutOpt was applied to two case studies. Firstly, in a limestone bench (Section 4.2.1) where fractures were modeled by the developed fracture modeling approach. The results of BlockCutOpt showed that the optimum cutting direction may vary from a strata to another deposited in the same bench providing different displacements for the cutting grid and consequently different recovery ratios for each strata. For future work, it is recommended to perform a field comparison study between the results obtained from BlockCutOpt and the results of cutting blocks in a bench since it could not be planned with the quarry management.

Secondly, BlockCutOpt was applied to a large scale quarrying area of granite where the regional fracturing were mapped by aerial photogrammetry (literature data). BlockCutOpt was used to test several scenarios of production optimization, to cut large volume blocks (LVBs) with and without the subdivision option of the large area. Considering the non-division option, the number of non-intersected LVBs was found variable with changing the cutting direction, and even within the horizontal displacements related to each cutting direction tested. Considering the sub-division option, the results showed that the optimum cutting direction, calculated by BlockCutOpt, was variable between the sub-divisions of quarrying zones. The total optimum recovery slightly decreased, as compared to the non-division solution, when the number of sub-divisions of quarrying zones increased (the borders acted as synthetic fractures). However, the maximum recovery ratio found for each sub-division zone can be considered the optimum one when the sub-division zones are independent for geographic or business reasons. The results in such large scale areas can be useful for long term production optimization (considering cutting of LVBs) and more detailed fracture data are required for cutting optimization of commercial-size blocks.

Dissemination of Results

A list of publications from the Ph.D. thesis is presented below:

[1] Elkarmoty M., Colla C., Gabrielli E., Bonduà S., Bruno R., 2016. Application of low frequency GPR antenna to fractures detection and 3D visualization in a new quarry bench (poster), in: The International Conference on Geosciences and Geophysics. 6-7 October 2016, Orlando, USA, and published abstract in Journal of Geology and Geophysics, Vol. 5, No. 5 (suppl.), p. 47. DOI:10.4172/2381-8719.C1.006

[2] Elkarmoty M., Colla C., Gabrielli E., Bonduà S., Bruno R., 2016. Three dimensional fractures detection by geo-radar for sustainable production of ornamental stones (abstract and presentation), in: The 1St International Sustainable Stone Conference, 20 May, Carrara, Italy.

[3] Elkarmoty M., Colla C., Gabrielli E., Bonduà S., Bruno R., 2017. Deterministic three-dimensional rock mass fracture modeling from geo-radar survey: A case study in a sandstone quarry in Italy. Environmental and Engineering Geoscience, Vol. 23, No. 4, Pp. 314-331. DOI: 10.2113/gseegeosci.23.4.314

[4] Elkarmoty M., Colla C., Gabrielli E., Papeschi P., Bonduà S., Bruno R., 2017. In-situ GPR test for three-dimensional mapping of the dielectric constant in a rock mass. Journal of Applied Geophysics, Vol. 146, Pp. 1-15. DOI:10.1016/j.jappgeo.2017.08.010

[5] Elkarmoty M., Colla C., Gabrielli E., Bonduà S., Bruno R., 2017. A combination of GPR survey and laboratory rock tests for evaluating an ornamental stone deposit in a quarry bench. Procedia Engineering, Vol. 191 (ISRM European Rock Mechanics Symposium EUROCK 2017), Pp. 999-1007. DOI: 10.1016/j.proeng.2017.05.272

[6] Elkarmoty M., Colla C., Gabrielli E., Bonduà S., Kasmaeeyazdi S.; Tinti F.; Bruno R., 2017. Mapping and modelling fractures using ground penetrating radar for ornamental stone assessment and recovery optimization: Two case studies. Rudarsko-Geološko-Naftni Zbornik (The Mining-Geology-Petroleum Engineering Bulletin). Vol. 32, No. 4, Pp. 63-76. DOI: 10.17794/rgn.2017.4.7

[7] Elkarmoty M., Bonduà S., Bruno R., 2017. Nuovi utilizzi del georadar nella valutazione di depositi di rocce ornamentali / GPR for ornamental stone deposits evaluation. Diamante A&T, Vol. 90, September 2017. ISSN: 1824-5765.

[8] Elkarmoty M., Tinti F., Kasmaeeyazdi S., Bonduà S., Bruno R., 2018. 3D modeling of discontinuities using GPR in a commercial size ornamental limestone block. Construction and Building Materials, Vol. 166, Pp. 81-86. DOI: 10.1016/j.conbuildmat.2018.01.091

[9] Elkarmoty M., Tinti F., Kasmaeeyazdi S., Bonduà S., Bruno R., 2018. A large-scale implementation of a fracture modeling approach-based georadar in a case study of limestone quarry. Engineering Geology, submitted in March 2018.

[10] Elkarmoty M., Bonduà S., Bruno R., 2018. An innovative 3D algorithm for an optimized cutting of slabs from ornamental stone blocks. Engineering Geology, submitted in March 2018.

[11] Elkarmoty M., Bonduà S., Bruno R., 2018. A 3D brute-force search algorithm for the optimum cutting direction in ornamental stone quarries. In submission phase.

References

Abdollahisharif J., Bakhtavar E., 2009. An intelligent algorithm of minimum cutting plane to find the optimal size of extractable-blocks in dimension stone quarries. Arch. Min. Sci. 54, 641–656.

Abu Hanieh, A., AbdElall, S., Hasan, A., 2014. Sustainable development of stone and marble sector in Palestine. J. Clean. Prod. 84, 581–588. doi:10.1016/j.jclepro.2013.10.045

Al-Nuaimy, W., Huang, Y., Nakhkash, M., Fang, M.T.C., Nguyen, V.T., Eriksen, A., 2000. Automatic detection of buried utilities and solid objects with GPR using neural networks and pattern recognition. J. Appl. Geophys. 43, 157–165. doi:10.1016/S0926-9851(99)00055-5

Annan, A.P., 2003. Ground penetrating radar principles, procedures, and applications. Sensors & Software Inc. doi:10.1016/B978-0-444-53348-7.00016-8

Annan, A.P., 2001. Ground penetrating radar: worshop notes. Sensors & Software Inc., Mississauga, Ontorio.

Annavarapu, S., Kemeny, J., Dessureault, S., 2012. Joint spacing distributions from oriented core data. Int. J. Rock Mech. Min. Sci. 52, 40–45. doi:10.1016/j.ijrmms.2012.02.003

Anthony, M., 2008. Rock mass slope stability analysis based on 3D terrestrial laser scanning and ground penetrating radar. Faculty of Geo-Information Science and Earth Observation, University of Twente, 112 pp.

Aqeel, A., Anderson, N., Maerz, N., 2013. Mapping subvertical discontinuities in rock cuts using a 400-MHz ground penetrating radar antenna. Arab. J. Geosci. 7, 2093–2105. doi:10.1007/s12517-013-0937-y

Arosio, D., 2016. Rock fracture characterization with GPR by means of deterministic deconvolution. J. Appl. Geophys. 126, 27–34. doi:10.1016/j.jappgeo.2016.01.006

Arosio, D., Munda, S., Zanzi, L., 2012. Quality control of stone blocks during quarrying activities, in: The 14th International Conference on Ground Penetrating Radar. 4-8 June 2012, Shanghai, China, pp. 822–826. doi:10.1109/ICGPR.2012.6254975

Artagan, S.S., Borecký, V., 2015. Estimation methods for obtaining GPR signal velocity, in: The Third Intl. Conf. on Advances in Civil, Structural and Environmental Engineering. Zurich, Switzerland, 10-11 October 2015. doi:10.15224/978-1-63248-065-1-40

Ashmole, I., Motloung, M., 2008. Dimension stone: the latest trends in exploration and

production technology., in: The International Conference on Surface Mining 2008 – Challenges, Technology, Systems and Solutions – Papers. The Southern African Institute of Mining and Metallurgy, Johannesburg, Republic of South Africa, pp. 35–70.

Assali, P., Grussenmeyer, P., Villemin, T., Pollet, N., Viguier, F., 2014. Surveying and modeling of rock discontinuities by terrestrial laser scanning and photogrammetry: Semi-automatic approaches for linear outcrop inspection. J. Struct. Geol. 66, 102–114. doi:10.1016/j.jsg.2014.05.014

ASTM International: D6432-11, 2011. Standard guide for using the surface ground penetrating radar method for subsurface investigation. doi:10.1520/D6432-11.2

Bargossi, G., Gamberini, F., Gasparotto, G., Grillini, G.C., Marocchi, M., 2004. Dimension and ornamental stones from the Tosco-Romagnolo and Bolognese Apennine. Period. di Mineral. 73, 171–195.

Bargossi, G.M., Gamberini, F., Marocchi, M., Fabbri, S., Peddis, F., Ravaglia, B., Vescogni, C., Marini, P., Bellopede, R., 2008. Mineralogical-petrographic and physical-mechanical characterization, in: Bartolomei, A., Montanari, F. (Eds.), Pietra Serena, Materia Della Citta. Edizioni AIDA Firenze, pp. 57–84.

Botelho, M.A.B., Mufti, I.R., 1998. Exploitation of limestone quarries in Brazil with depth migrated ground-penetrating radar data. Soc. Explor. Geophys. Expand. Abstr. 836–839.

Bourke P., 2011. PLY - Polygon File Format [WWW Document]. URL http://paulbourke.net/dataformats/ply/ (accessed 1.25.18).

Carvalho, J.F., Henriques, P., Falé, P., Luís, G., 2008. Decision criteria for the exploration of ornamental-stone deposits: Application to the marbles of the Portuguese Estremoz Anticline. Int. J. Rock Mech. Min. Sci. 45, 1306–1319. doi:10.1016/j.ijrmms.2008.01.005

Cassidy, N.J., 2009. Electrical and magnetic properties of rocks, soils and fluids, in: Ground Penetrating Radar: Theory and Applications. Elsevier, Amsterdam, Netherlands, pp. 41–72. doi:10.1016/B978-0-444-53348-7.00002-8

Cho, T.F., Lee, S.B., Won, K.S., 2012. Three-dimensional deterministic block analysis model for information-oriented excavation design. Int. J. Rock Mech. Min. Sci. 55, 63–70. doi:10.1016/j.ijrmms.2012.05.003

Coli, M., Livi, E., Pandeli, E., Tanini, C., 2012. Pietra Serena mining in Fiesole. Part II: geological situation. J. Min. Sci. XXXIII, 81–87. doi:10.1023/A:1025761227284

Colla, C., 1997. Non-destructive testing of masonry arch bridges. Ph.D. thesis, Dept. of Civil and Environmental Engineering, Faculty of Science and Engineering, The University of Edinburgh, Edinburgh, Scotland, UK, 1 vol., 272 pp.

Colla, C., Burnside, C.D., Clark, M.R., Broughton, K.J., Forde, M.C., 1998. Comparison of laboratory and simulated data for radar image interpretation. NDT E Int. 31, 439–444. doi:10.1016/S0963-8695(98)00043-7

Daniels, D.J., 2004. Ground penetrating radar. The Institute of Electrical Engineers, London, UK.

Dannowski, G., Yaramanci, U., 1999. Estimation of water content and porosity using combined radar and geoelectrical measurements. Eur. J. Environ. Eng. Geophys. 4, 74–85.

Davis, J.L., Annan, A.P., 1989. Ground-penetrating radar for high resolution mapping of soil and rock stratigraphy. Geophys. Prospect. 37, 531–551. doi:10.1111/j.1365-2478.1989.tb02221.x

Dekeyser, L., Brunton, F.R., Endres, A.L., Armstrong, D.K., Coniglio, M., Tetreault, D.K., 2007. Ground-penetrating radar as a resource assessment tool for silurian-age carbonate building stone quarries on the Bruce Peninsula, Southern Ontario. Ontario, Ontario Geological Survey, Open File Report 6212, p. 54.

Deliormanli, A.H., Maerz, N.H., 2016. Stress related fracturing in dimension stone quarries. IOP Conf. Ser. Earth Environ. Sci. 44, 1–6. doi:10.1088/1755-1315/44/5/052020

Deliormanli, A.H., Maerz, N.H., Otoo, J., 2014. Using terrestrial 3D laser scanning and optical methods to determine orientations of discontinuities at a granite quarry. Int. J. Rock Mech. Min. Sci. 66, 41–48. doi:10.1016/j.ijrmms.2013.12.007

Dérobert, X., Abraham, O., 2000. GPR and seismic imaging in a gypsum quarry. J. Appl. Geophys. 45, 157–169. doi:10.1016/S0926-9851(00)00025-2

Dezayes, C., Villemin, T., Pêcher, A., 2000. Microfracture pattern compared to core-scale fractures in the borehole of Soultz-sous-Forêts granite, Rhine graben, France. J. Struct. Geol. 22, 723–733. doi:10.1016/S0191-8141(00)00003-1

Elmouttie, M.K., Poropat, G. V., 2012. A method to estimate in situ block size distribution. Rock Mech. Rock Eng. 45, 401–407. doi:10.1007/s00603-011-0175-0

Elshafie, A., Heggy, E., 2013. Dielectric and hardness measurements of planetary analog rocks

in support of in-situ subsurface sampling. Planet. Space Sci. 86, 150–154. doi:10.1016/j.pss.2013.02.003

Fernández-de Arriba, M., Díaz-Fernández, M.E., González-Nicieza, C., Álvarez-Fernández, M.I., Álvarez-Vigil, A.E., 2013. A computational algorithm for rock cutting optimisation from primary blocks. Comput. Geotech. 50, 29–40. doi:10.1016/j.compgeo.2012.11.010

Fisher, J.E., Shakoor, A., Watts, C.F., 2014. Comparing discontinuity orientation data collected by terrestrial LiDAR and transit compass methods. Eng. Geol. 181, 78–92. doi:10.1016/j.enggeo.2014.08.014

Forte, E., Pipan, M., 2007. GPR rock mass imaging and characterization by attenuation analysis, in: The 26th National Meeting of Gruppo Nazionale Di Geofisica Della Terra Solida GNGTS. 13-15 November 2007, Rome, Italy., pp. 426–430.

Gacitúa, G., Peter, M., Munch, S., Andrés, J., 2012. Estimations of moisture content in the active layer in an Arctic ecosystem by using ground-penetrating radar pro fi ling. J. Appl. Geophys. 79, 100–106. doi:10.1016/j.jappgeo.2011.12.003

Gao, M., Jin, W., Zhang, R., Xie, J., Yu, B., Duan, H., 2016. Fracture size estimation using data from multiple boreholes. Int. J. Rock Mech. Min. Sci. 86, 29–41. doi:10.1016/j.ijrmms.2016.04.005

Geophysical Survey systems Inc., 2006. GSSI Handbook For RADAR Inspection of Concrete. Geophysical Survey Systems, Inc.

Gillespie, M.R., Barnes, R.P., Milodowski, A.E., 2011. British Geological Survey scheme for classifying discontinuities and filings, British Geological Survey. Keyworth, Nottingham, England.

Golden Software LLC, 2017. Webpage of Voxler [WWW Document]. URL http://www.goldensoftware.com/products/voxler (accessed 12.13.17).

Grandjean, G., Gourry, J.C., 1996. GPR data processing for 3D fracture mapping in a marble quarry (Thassos, Greece). J. Appl. Geophys. 36, 19–30. doi:10.1016/S0926-9851(96)00029-8

Grasmueck, M., 1996. 3-D ground-penetrating radar applied to fracture imaging in gneiss. Geophysics 61, 1050. doi:10.1190/1.1444026

Grasmueck, M., Quintà, M.C., Pomar, K., Eberli, G.P., 2013. Diffraction imaging of sub-vertical fractures and karst with full-resolution 3D Ground-Penetrating Radar. Geophys.

Prospect. 61, 907–918. doi:10.1111/1365-2478.12004

Grasmueck, M., Weger, R., Horstmeyer, H., 2004. Three-dimensional ground-penetrating radar imaging of sedimentary structures, fractures, and archaeological features at submeter resolution. Geology 32, 933. doi:10.1130/G20776.1

Greaves, R.J., Lesmes, D.P., Lee, J.M., Tosksoz, M.N., 1996. Velocity variations and water content estimated from multi-offset, ground-penetrating radar. GEOPHYSICS 61, 683–695. doi:10.1190/1.1443996

Gudmundsson, A., Kusumoto, S., Simmenes, T.H., Philipp, S.L., Larsen, B., 2009. Effects of rock stiffness and loading conditions on aperture variations of rock fractures and associated fluid flow rates, in: European Geosciences Union General Assembly. 19-24 April 2009, Vienna, Austria, p. 6347.

Guigue, P., Devillers, O., 2003. Fast and robust triangle-triangle overlap test using orientation predicates. J. Graph. Tools 8, 25–32. doi:10.1080/10867651.2003.10487580

He, X., Zhu, Z., Liu, Q., Lu, G., 2009. Review of GPR rebar detection, in: PIERS Proceedings. Beijing, China, March 23-23, 2009., pp. 804–813.

Hoegh, K., Khazanovich, L., Dai, S., Yu, T., 2015. Evaluating asphalt concrete air void variation via GPR antenna array data. Case Stud. Nondestruct. Test. Eval. 3, 27–33. doi:10.1016/j.csndt.2015.03.002

Huisman, J.A., Hubbard, S.S., Redman, J.D., Annan, A.P., 2003. Measuring Soil Water Content with Ground Penetrating Radar: A Review. Vadose Zo. J. 2, 476–491. doi:10.2113/2.4.476

International Society for Rock Mechanics (ISRM), 2007. The Blue Book: The complete ISRM suggested methods for rock characterization, testing and monitoring: 1974–2006. Compilation arranged by the ISRM Turkish National Group, Ankara, Turkey. Kazan Offset Press, Ankara.

ISRM, 1979. Suggested methods for the quantitative description of discontinuities in rock masses. Int. J. Rock Mech. Min. Sci. Geomech. Abstr. 15, 319–368. doi:10.1016/0148-9062(78)91472-9

ISRM, 1978. International society for rock mechanics commission on standardization of laboratory and field tests. Int. J. Rock Mech. Min. Sci. Geomech. Abstr. 15, 319–368. doi:10.1016/0148-9062(78)91472-9

Jeannin, M., Garambois, S., Grégoire, C., Jongmans, D., 2006. Multiconfiguration GPR measurements for geometric fracture characterization in limestone cliffs (Alps). Geophysics 71, B85. doi:10.1190/1.2194526

Kadioglu, S., 2008. Photographing layer thicknesses and discontinuities in a marble quarry with 3D GPR visualisation. J. Appl. Geophys. 64, 109–114. doi:10.1016/j.jappgeo.2008.01.001

Kemeny, J., Post, R., 2003. Estimating three-dimensional rock discontinuity orientation from digital images of fracture traces. Comput. Geosci. 29, 65–77. doi:10.1016/S0098-3004(02)00106-1

Koster, B., Kruse, F., 2016. The use of ground penetrating radar (GPR) in the investigation of historical quarry abandonment in Svalbard. Polar Rec. (Gr. Brit). 52, 330–344. doi:10.1017/S0032247415000844

La Borghigiana Srl website, 2017. Pietra Serena. [WWW Document]. URL www.laborghigiana.com/gamma/

Lai, P., Samson, C., Bose, P., 2014. Visual enhancement of 3D images of rock faces for fracture mapping. Int. J. Rock Mech. Min. Sci. 72, 325–335. doi:10.1016/j.ijrmms.2014.09.016

Lau, J.S.O., Auger, L.F., Bisson, J.G., 1987. Subsurface fracture surveys using a borehole television camera and acoustic televiewer. Can. Geotech. J. 24, 499–508.

Lu, P., Latham, J.-P., 1999. Developments in the assessment of in-situ block size distributions of rock masses. Rock Mech. Rock Eng. 32, 29–49. doi:10.1007/s006030050042

Lualdi, M., Zanzi, L., 2004. 2D and 3D experiments to explore the potential benefit of GPR investigations in planning the mining activity of a limestone quarry, in: The Tenth International Conference Ground Penetrating Radar, GPR2004. pp. 613–616.

Luodes, H., 2008. Natural stone assessment with ground penetrating radar. Est. J. Earth Sci. 57, 149–155. doi:10.3176/earth.2008.3.03

Luodes, H., Selonen, O., Pääkkönen, K., 2000. Evaluation of dimension stone in gneissic rocks - a case history from southern Finland. Eng. Geol. 52, 209–223. doi:10.1016/S0013-7952(00)00059-4

Luodes, H., Sutinen, H., 2011. Evaluation and modelling of natural stone rock quality using Ground Penetrating Radar (GPR), in: Nenonen, K., Nurmi P.A. (Eds.), Geoscience for Society. 125th Anniversary Volume. Geological Survey of Finland, Special Paper 49. pp.

83–90.

Luodes, H., Sutinen, H., Härmä, P., Pirinen, H., Selonen, O., 2015. Assessment of potential natural stone deposits, in: Lollino G., Manconi A., Guzzetti F., Culshaw M., Bobrowsky P., L.F. (Ed.), Engineering Geology for Society and Territory - Volume 5. Springer, Cham, pp. 243–246. doi:10.1007/978-3-319-09048-1_47

Maerz, N.H., Aqeel, A.M., Anderson, N., 2015. Measuring orientations of individual concealed sub-vertical discontinuities in sandstone rock cuts integrating ground penetrating radar and terrestrial LIDAR. Environ. Eng. Geosci. XXI, 293–309. doi:10.2113/gseegeosci.21.4.293

Maerz, N.H., Kim, W., 2000. Potential use of ground penetrating radar in highway rock cut stability, in: Geophysics 2000. St. Louis, Missouri, United States of America.

Marji, M.F., Pashapour, A., Gholamnejad, J., 2012. Relationship between fracture dip angle, aperture and fluid flow in the fractured rock masses. J. Min. Environ. 2, 136–145. doi:10.22044/JME.2012.65

Markovaara-Koivisto, M., Hokkanen, T., Huuskonen-Snicker, E., 2014. The effect of fracture aperture and filling material on GPR signal. Bull. Eng. Geol. Environ. 73, 815–823. doi:10.1007/s10064-013-0566-4

Martinez-Torres, L.P., 2002. Characterization of naturally fractured reservoirs using conventional well logs. Master thesis, Norman University, Oklahoma, 137p.

Mineo, S., Pappalardo, G., Rapisarda, F., Cubito, A., Di Maria, G., 2015. Integrated geostructural, seismic and infrared thermography surveys for the study of an unstable rock slope in the Peloritani Chain (NE Sicily). Eng. Geol. 195, 225–235. doi:10.1016/j.enggeo.2015.06.010

Molyneaux, T.C.K., Millard, S.G., Bungey, J.H., Zhou, J.Q., 1995. Radar assessment of structural concrete using neural networks. NDT&E Int. 28, 281–288. doi:10.1016/0963-8695(95)00027-U

Montani, C., 2008. Stone 2008—world marketing handbook. Faenza, Gruppo Editoriale Faenza Editice, Faenza.

Montani, C., 2003. Stone 2002—world marketing handbook. Gruppo Editoriale Faenza Editice., Faenza, Italy.

Mosch, S., Nikolayew, D., Ewiak, O., Siegesmund, S., 2011. Optimized extraction of

dimension stone blocks. Environ. Earth Sci. 63, 1911–1924. doi:10.1007/s12665-010-0825-7

Mubiayi, M.P., 2013. Characterisation of sandstones : mineralogy and physical properties, in: The World Congress on Engineering Vol III. July 3 - 5, 2013, London, UK.

Mukherjee, D., Heggy, E., Khan, S.D., 2010. Geoelectrical constraints on radar probing of shallow water-saturated zones within karstified carbonates in semi-arid environments. J. Appl. Geophys. 70, 181–191. doi:10.1016/j.jappgeo.2009.11.005

Mutlutürk, M., 2007. Determining the amount of marketable blocks of dimensional stone before actual extraction. J. Min. Sci. 43, 75–80. doi:10.1007/s10913-007-0008-4

Mysaiah, D., Maheswari, K., Srihari Rao, M., Senthil Kumar, P., Seshunarayana, T., 2011. Ground-penetrating radar applied to imaging sheet joints in granite bedrock. Curr. Sci. 100, 473–475.

Palmström, A., 1995. RMi – a rock mass characterization system for rock engineering purposes. PhD thesis, Oslo University, Norway.

ParaView website, 2017. ParaView software package [WWW Document]. URL http://www.paraview.org/ (accessed 1.25.18).

Park, H.J., West, T.R., 2002. Sampling bias of discontinuity orientation caused by linear sampling technique. Eng. Geol. 66, 99–110. doi:10.1016/s0013-7952(02)00034-0

Porsani, J.L., Sauck, W. a., Júnior, A.O.S., 2006. GPR for mapping fractures and as a guide for the extraction of ornamental granite from a quarry: A case study from southern Brazil. J. Appl. Geophys. 58, 177–187. doi:10.1016/j.jappgeo.2005.05.010

Priest, S.D., Hudson, J.A., 1981. Estimation of discontinuity spacing and trace length using scanline surveys. Int. J. Rock Mech. Min. Sci. Geomech. Abstr. 18, 82. doi:10.1016/0148-9062(81)90026-7

Qiao, L., Qin, Y., Ren, X., Wang, Q., 2015. Identification of buried objects in GPR using amplitude modulated signals extracted from multiresolution monogenic signal analysis. Sensors 15, 30340–30350. doi:10.3390/s151229801

Rafezi, H., Novo, A., Hassani, F.P., 2015. An investigation into application of Ground Penetrating Radar (GPR) in surface mining, in: Symposium on the Application of Geophysics to Engineering and Environmental Problems SAGEEP2015. 22-26 March 2015, Austin, Texas, USA, pp. 54–60. doi:10.4133/SAGEEP.28-006

Reina, A., Loi, M., 2015. Environmental background in Apricena quarries (Apulia, Southern Italy), in: Lollino, G., Manconi, A., Guzzetti, F., Culshaw, M., Bobrowsky, P., Luino, F. (Eds.), Engineering Geology for Society and Territory - Volume 5: Urban Geology, Sustainable Planning and Landscape Exploitation. Springer International Publishing, Switzerland, pp. 1–1400. doi:10.1007/978-3-319-09048-1_57

Rey, J., Martínez, J., Vera, P., Ruiz, N., Cañadas, F., Montiel, V., 2015. Ground-penetrating radar method used for the characterisation of ornamental stone quarries. Constr. Build. Mater. 77, 439–447. doi:10.1016/j.conbuildmat.2014.12.076

Reynolds, J.M., 2011. An introduction to applied and environmental geophysics. A John Wiley & Sons, Ltd., West Sussex, UK.

Rhazi, J., Dous, O., Kaveh, S., 2004. Detection of fractures in concrete by GPR technique, in: 16th World Conference on NDT 2004. Montreal, Canada, pp. 1–5.

Rutqvist, J., 2015. Fractured rock stress-permeability relationships from in situ data and effects of temperature and chemical-mechanical couplings. Geofluids 15, 48–66. doi:10.1111/gfl.12089

Saarenketo, T., Scullion, T., 2000. Road evaluation with ground penetrating radar. J. Appl. Geophys. 43, 119–138. doi:10.1016/S0926-9851(99)00052-X

Seol, S.J., Kim, J.-H., Song, Y., Chung, S.-H., 2001. Finding the strike direction of fractures using GPR. Geophys. Prospect. 49, 300–308. doi:10.1046/j.1365-2478.2001.00262.x

Seren, A., Acikgoz, A.D., 2012. Imaging fractures in a massive limestone with ground penetrating radar, Haymana, Turkey. Sci. Res. Essays 7, 3368–3381. doi:10.5897/SRE11.1877

Shihab, S., Al-Nuaimy, W., 2005. Radius estimation for cylindrical objects detected by ground penetrating radar. Subsurf. Sens. Technol. Appl. 6, 151–166. doi:10.1007/s11220-005-0004-1

Sohrabian, B., Ozcelik, Y., 2012. Determination of exploitable blocks in an andesite quarry using independent component kriging. Int. J. Rock Mech. Min. Sci. 55, 71–79. doi:10.1016/j.ijrmms.2012.06.009

Sonntag, R., Evans, J.P., Pointe, P.L.A., Deraps, M., Sisley, H., Richey, D., 2012. Sedimentological controls on the fracture distribution and network development in Mesaverde Group sandstone lithofacies , Uinta Basin , Utah , USA. Adv. Study Fract.

Reserv. Geol. Soc. London, Spec. Publ. 374. doi:10.1144/SP374.4

Sousa, L., Barabasch, J., Stein, K.J., Siegesmund, S., 2017. Characterization and quality assessment of granitic building stone deposits: A case study of two different Portuguese granites. Eng. Geol. 221, 29–40. doi:10.1016/j.enggeo.2017.01.030

Sousa, L.M.O., Oliveira, A.S., Alves, I.M.C., 2016. Influence of fracture system on the exploitation of building stones: the case of the Mondim de Basto granite (north Portugal). Environ. Earth Sci. 75, 39. doi:10.1007/s12665-015-4824-6

Stavropoulou, M., 2014. Discontinuity frequency and block volume distribution in rock masses. Int. J. Rock Mech. Min. Sci. 65, 62–74. doi:10.1016/j.ijrmms.2013.11.003

Taboada, J., Vaamonde, A., Saavedra, A., 1999. Evaluation of the quality of a granite quarry. Eng. Geol. 53, 1–11. doi:10.1016/s0013-7952(98)00074-x

Taboada, J., Vaamonde, a., Saavedra, a., Alejano, L., 1997. Application of geostatistical techniques to exploitation planning in slate quarries. Eng. Geol. 47, 269–277. doi:10.1016/S0013-7952(97)00024-0

Tercan, A.E., Özçelik, Y., 2000. Geostatistical evaluation of dimension-stone quarries. Eng. Geol. 58, 25–33. doi:10.1016/S0013-7952(00)00048-X

Theune, U., Rokosh, D., Sacchi, M.D., Schmitt, D.R., 2006. Mapping fractures with GPR: A case study from Turtle Mountain. Geophysics 71, 139–150. doi:10.1190/1.2335515

Tillard, S., Dubois, J., 1995. Analysis of GPR data : wave propagation velocity determination. J. Appl. Geophys. 33, 77–91. doi:10.1016/0926-9851(95)90031-4

Tomasic, I., 1994. The influence of discontinuity fabric and other factors on optimum exploitation of dimension stone. Rud. Zb. 6, 101–105.

Toshioka, T., Tsuchida, T., Sasahara, K., 1995. Application of GPR to detecting and mapping cracks in rock slopes. J. Appl. Geophys. 33, 119–124. doi:10.1016/0926-9851(95)90035-7

Tsoflias, G.P., Van Gestel, J., Stoffa, P.L., Blankenship, D.D., Sen, M., 2004. Vertical fracture detection by exploiting the polarization properties of ground-penetrating radar signals. Geophysics 69, 803–810. doi:10.1190/1.1759466

Turanboy, A., 2010. A geometric approach for natural rock blocks in engineering structures. Comput. Geosci. 14, 565–577. doi:10.1007/s10596-009-9171-9

Turanboy, A., Ülker, E., 2008. LIP-RM: An attempt at 3D visualization of in situ rock mass

structures. Comput. Geosci. 12, 181–192. doi:10.1007/s10596-007-9077-3

Ülker, E., Turanboy, A., 2009. Maximum volume cuboids for arbitrarily shaped in-situ rock blocks as determined by discontinuity analysis—A genetic algorithm approach. Comput. Geosci. 35, 1470–1480. doi:10.1016/j.cageo.2008.08.017

United Nations, 1976. The development potential of dimension stone. Department of Economic and Social Affairs, New York, USA.

Varela-ortiz, W., Cintrón, C.Y.L., Velázquez, G.I., Stanton, T.R., 2013. Load testing and GPR assessment for concrete bridges on military installations. Constr. Build. Mater. 38, 1255–1269. doi:10.1016/j.conbuildmat.2010.09.044

Vasuki, Y., Holden, E.-J., Kovesi, P., Micklethwaite, S., 2014. Semi-automatic mapping of geological Structures using UAV-based photogrammetric data: An image analysis approach. Comput. Geosci. 69, 22–32. doi:10.1016/j.cageo.2014.04.012

Wackernagel, H., 2003. Multivariate geostatistics: An introduction with applications. Springer-Verlag Berlin Heidelberg. doi:10.1007/978-3-662-05294-5

Walton, G., Lato, M., Anschütz, H., Perras, M.A., Diederichs, M.S., 2015. Non-invasive detection of fractures, fracture zones, and rock damage in a hard rock excavation — Experience from the Äspö Hard Rock Laboratory in Sweden. Eng. Geol. 196, 210–221. doi:10.1016/j.enggeo.2015.07.010

White, C.D., Willis, B.J., Dutton, S.P., Bhattacharya, J.P., Narayanan, K., 2004. Sedimentology, statistics, and flow behavior for a tide-influenced deltaic sandstone, Frontier Formation, Wyoming, United States, in: Grammer, G.M., Harris, P.M., Eberli, G.P. (Eds.), Integration of Outcrop and Modern Analogs in Reservoir Modeling: AAPG Memoir 80. The American Association of Petroleum Geologists, Tulsa, Oklahoma, pp. 129–152.

Widess, M.B., 1973. How thin is a thin bed? Geophysics 38, 1176–1180.

Yarahmadi, R., Bagherpour, R., Kakaie, R., Mirzaie, N.H., Yari, M., 2014. Development of 2D computer program to determine geometry of rock mass blocks. Int. J. Min. Sci. Technol. 24, 191–194. doi:10.1016/j.ijmst.2014.01.008

Yarahmadi, R., Bagherpour, R., Khademian, A., Mirzaie, H., Kakaie, R., 2015. Developing a Matlab code for determine geometry of rock mass blocks and its application in mining and rock mechanic engineering. J. Min. Metall. 51A, 41–49.

doi:10.5937/JMMA1501041Y

Yarahmadi, R., Bagherpour, R., Khademian, A., Sousa, L.M.O., Almasi, S.N., Esfahani, M.M., 2017a. Determining the optimum cutting direction in granite quarries through experimental studies: a case study of a granite quarry. Bull. Eng. Geol. Environ. in press article, pp 1-9. doi:10.1007/s10064-017-1158-5

Yarahmadi, R., Bagherpour, R., Taherian, S.-G., Sousa, L.M.O., 2017b. Discontinuity modelling and rock block geometry identification to optimize production in dimension stone quarries. Eng. Geol. in press article. doi:10.1016/j.enggeo.2017.11.006

Yarahmadi, R., Bagherpour, R., Taherian, S.G., Sousa, L.M.O., 2017c. A new quality factor for the building stone industry: a case study of stone blocks, slabs, and tiles. Bull. Eng. Geol. Environ. 1–10. doi:10.1007/s10064-017-1040-5

Yelfm, R.J., 2007. Application of ground penetrating radar to civil and geotechnical engineering. Electromagntic Phenom. 7, 103–117.

Yi, M., Kim, J., Cho, S., Sato, M., 2004. Integrated application of borehole radar reflection and resistivity tomography to delineate fractures in granite quarry mine, in: Tenth International Conference on Ground Penetrating Radar,. 21-24 June, Delft, The Netherlands, pp. 213–216.

Zajc, M., Gosar, A., Pogacnik, Z., 2013. Analysis of tectonic and karst formations as geological hazard for exploitation of flyschoid rocks by Ground Penetrating Radar, the case of Anhovo-Rodez quarry (W Slovenia)., in: 7th International Workshop on Advanced Ground Penetrating Radar. IEEE, Nantes, France., pp. 1–6. doi:10.1109/IWAGPR.2013.6601545

Zajc, M., Pogačnik, Ž., Gosar, A., 2014. Ground penetrating radar and structural geological mapping investigation of karst and tectonic features in flyschoid rocks as geological hazard for exploitation. Int. J. Rock Mech. Min. Sci. 67, 78–87. doi:10.1016/j.ijrmms.2014.01.011

Zanzi, L., Hojat, A., Ranjbar, H., Karimi-Nasab, S., Azadi, A., Arosio, D., 2017. GPR measurements to detect major discontinuities at Cheshmeh-Shirdoosh limestone quarry, Iran. Bull. Eng. Geol. Environ. doi:10.1007/s10064-017-1153-x

Zazoun, R.S., 2013. Fracture density estimation from core and conventional well logs data using artificial neural networks: The Cambro-Ordovician reservoir of Mesdar oil field,

Algeria. J. African Earth Sci. 83, 55–73. doi:10.1016/j.jafrearsci.2013.03.003

Zeeb, C., Gomez-rivas, E., Bons, P.D., 2013. Evaluation of sampling methods for fracture network characterization using outcrops. Bull. Am. Assoc. Pet. Geol. 97, 1545–1566. doi:10.1306/02131312042

Zhan, R., Xie, H., 2009. GPR measurement of the diameter of steel bars in concrete specimens based on the stationary wavelet transform. Insight Non-Destructive Test. Cond. Monit. 51, 151–155. doi:10.1784/insi.2009.51.3.151

Zimmer, V.L., Sitar, N., 2015. Detection and Location of Rock Falls Using Seismic and Infrasound Sensors. Eng. Geol. 193, 49–60. doi:10.1016/j.enggeo.2015.04.007

Zou, D.H., Wu, Y.K., 2001. Investigation of blast-induced fracture in rock mass using reversed vertical seismic profiling. J. Appl. Geophys. 48, 153–162. doi:10.1016/S0926-9851(01)00079-9

Appendix A

The interpretation of fractures in the radargrams of 700 MHz antenna within the divided volumes are given below.

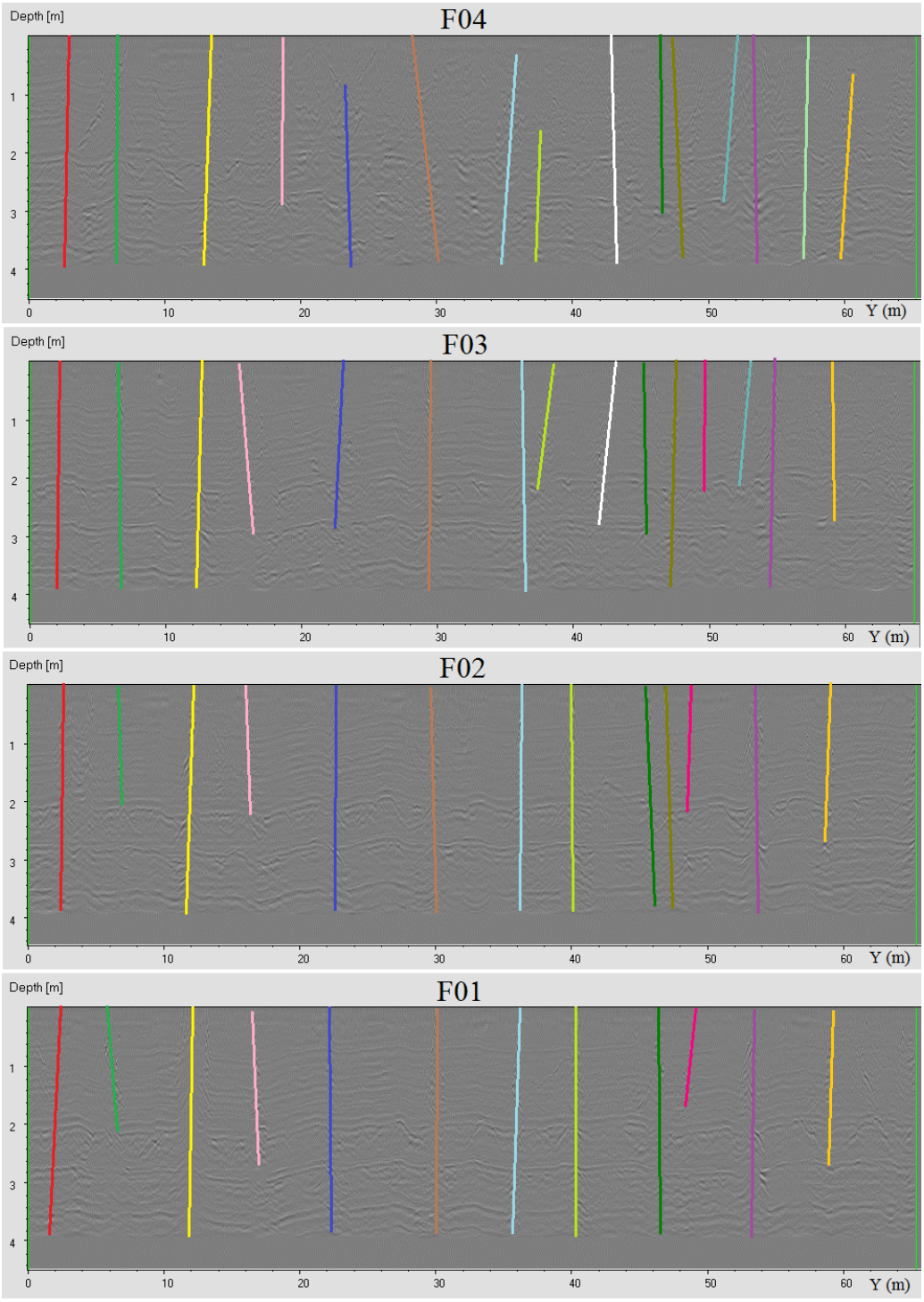

Volume 1: the interpreted radargrams F01, F02, F03, and F04.

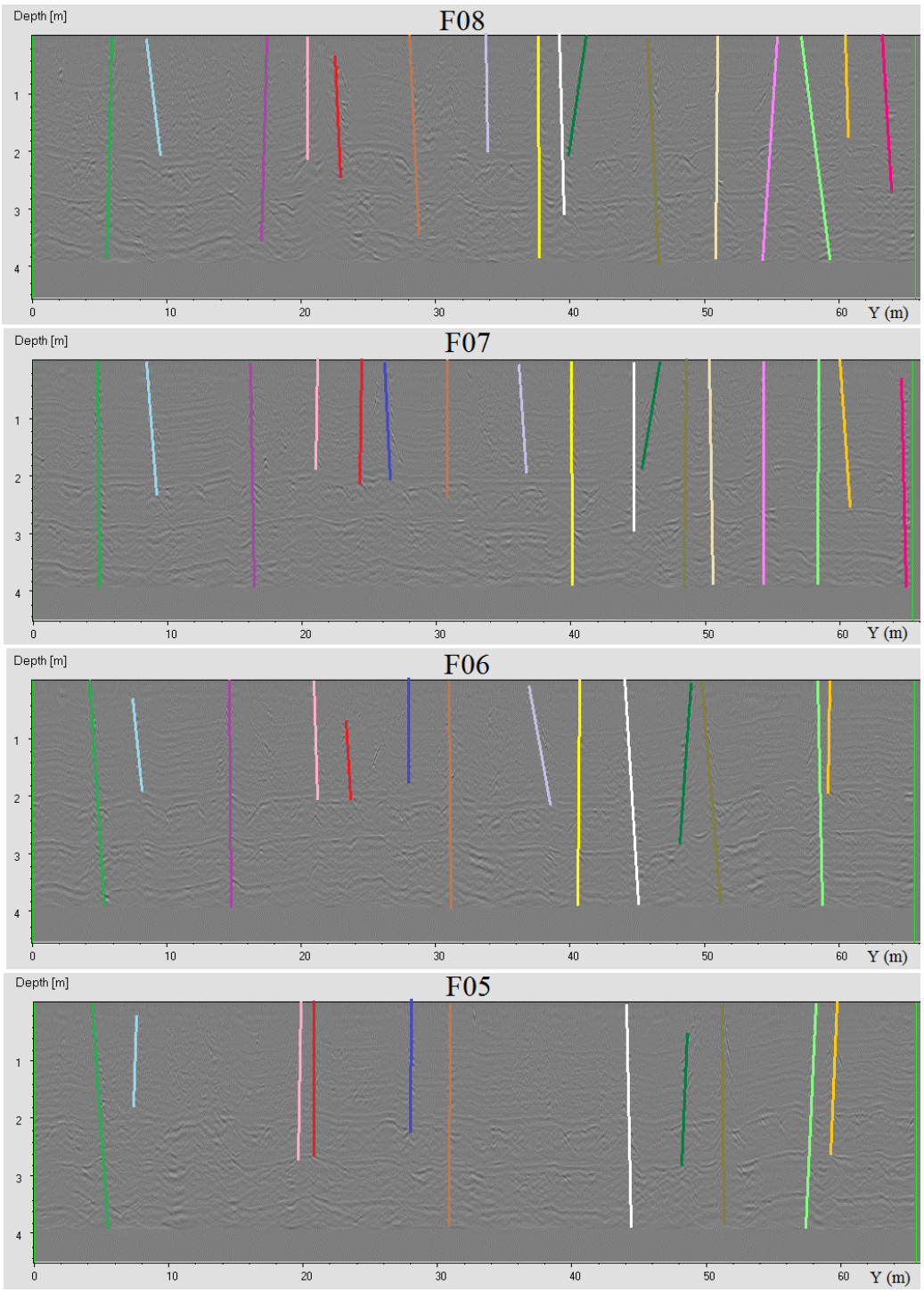

Volume 2: the interpreted radargrams F05, F06, F07, and F08.

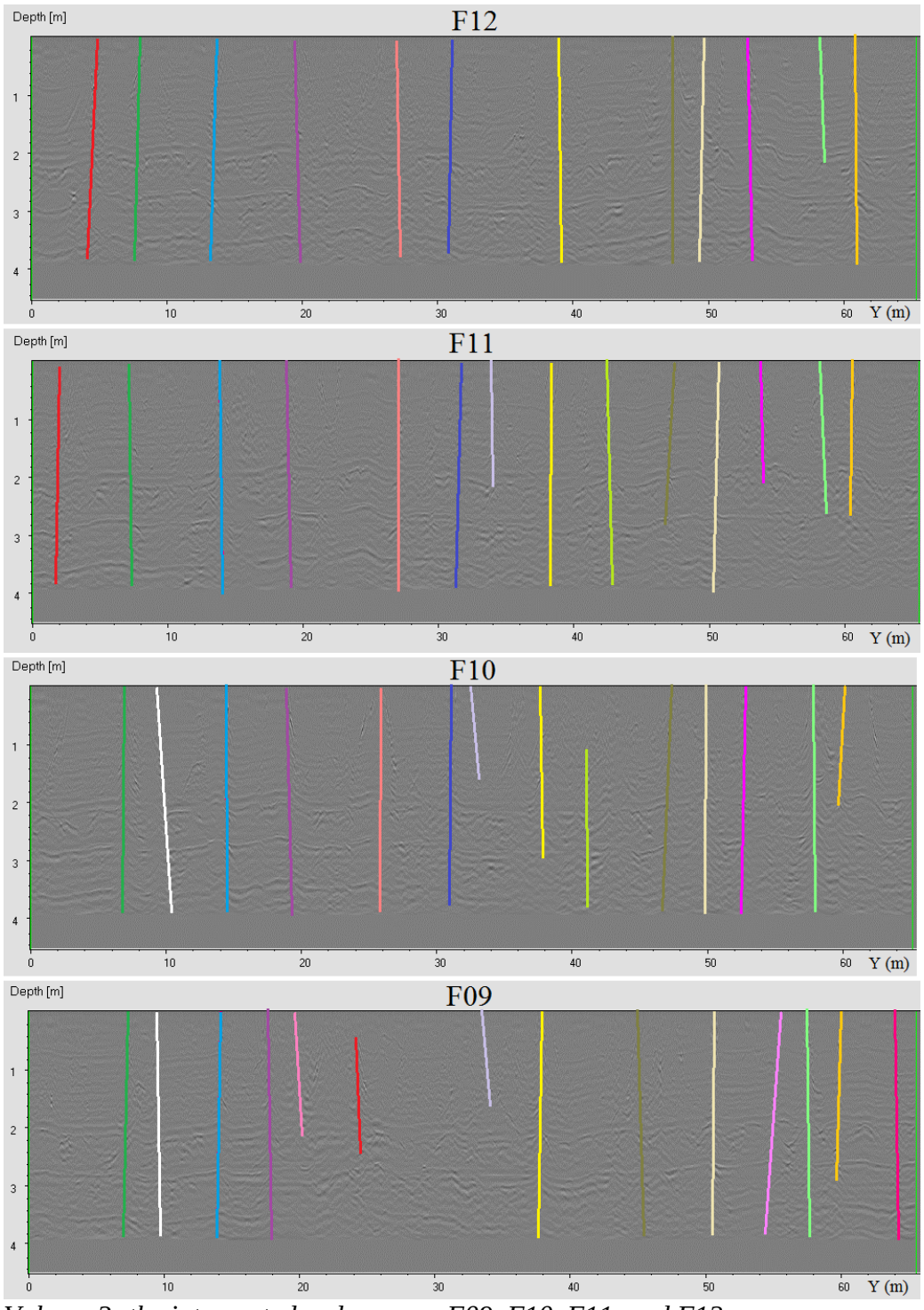

Volume 3: the interpreted radargrams F09, F10, F11, and F12.

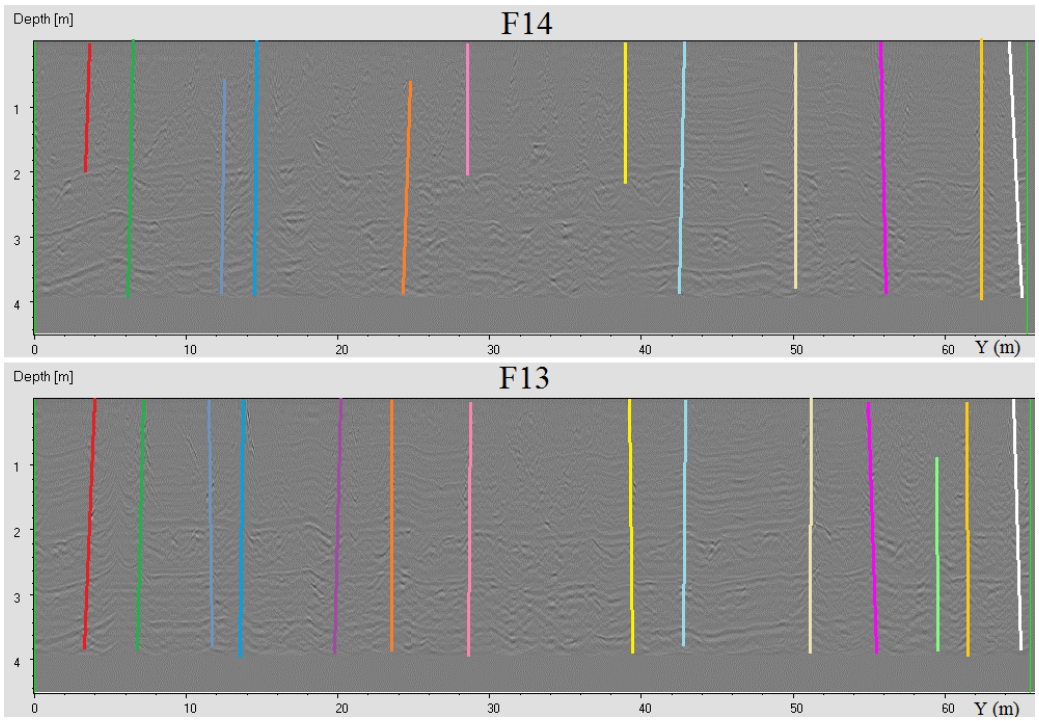

Volume 4: the interpreted radargrams F13 and F14.

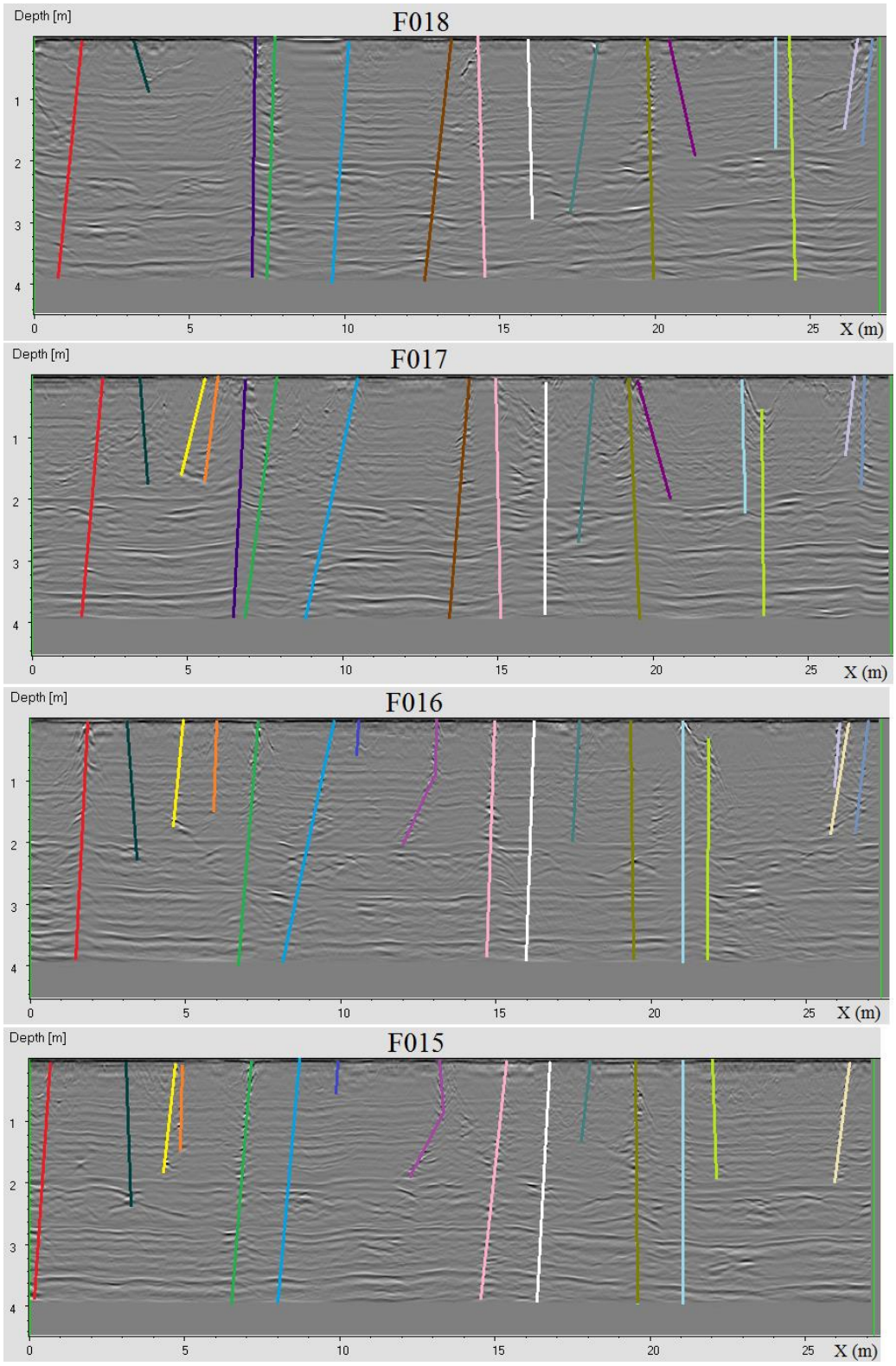

Volume 5: the interpreted radargrams F15, F16, F17, and F18.

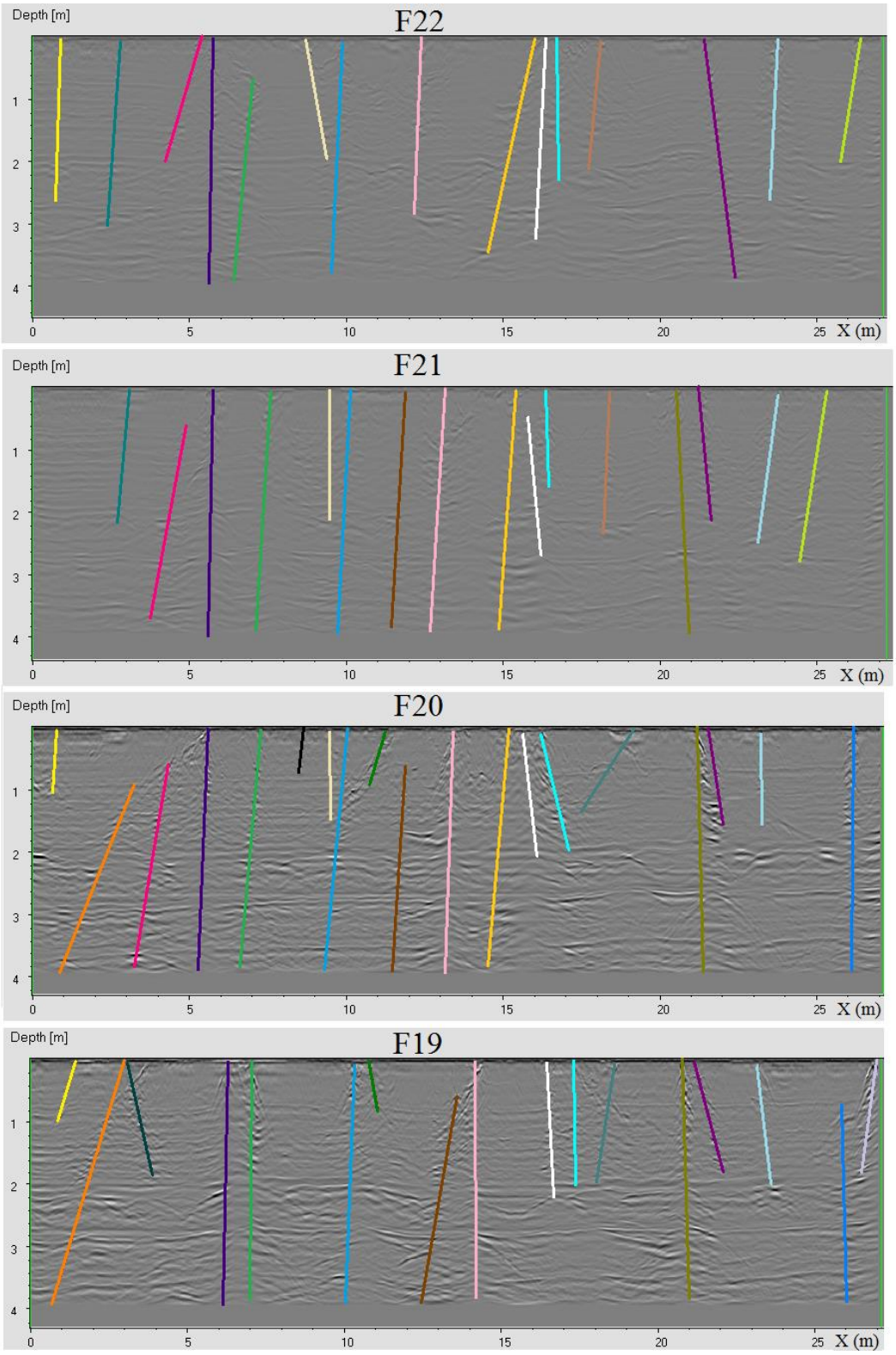

Volume 6: the interpreted radargrams F19, F20, F21, and F22.

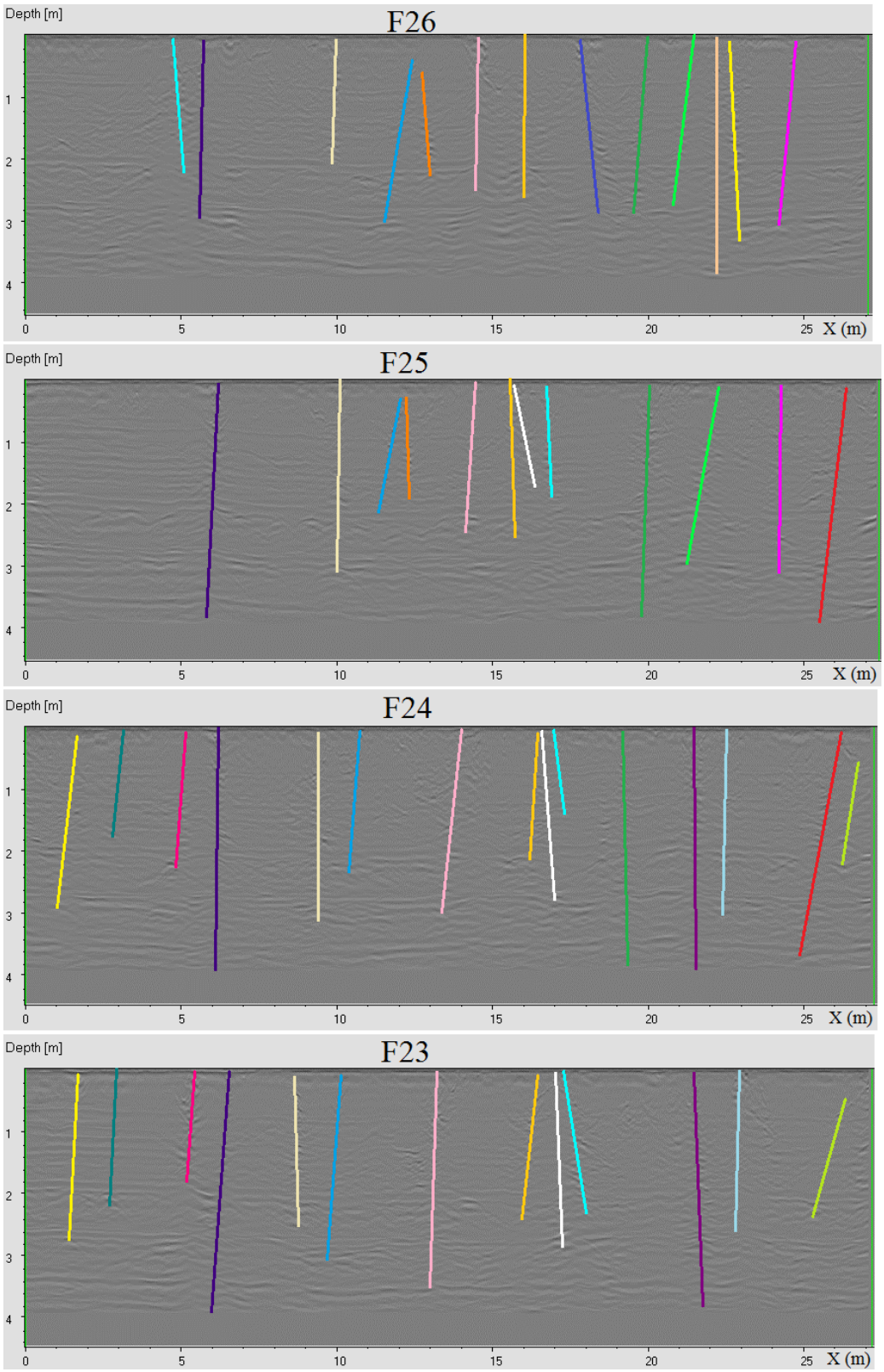

Volume 7: the interpreted radargrams F23, F24, F25, and F26.

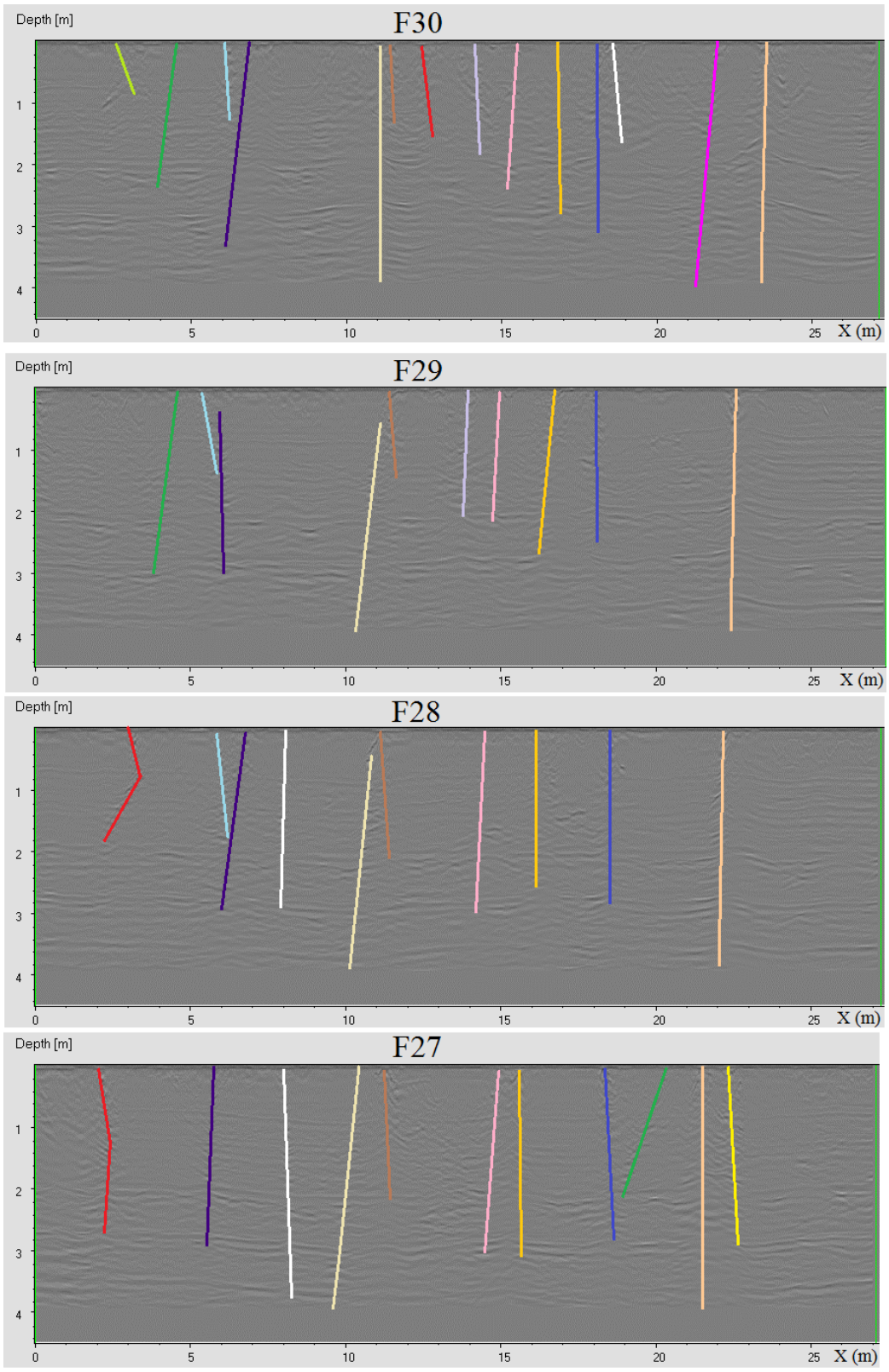

Volume 8: the interpreted radargrams F27, F28, F29, and F30.

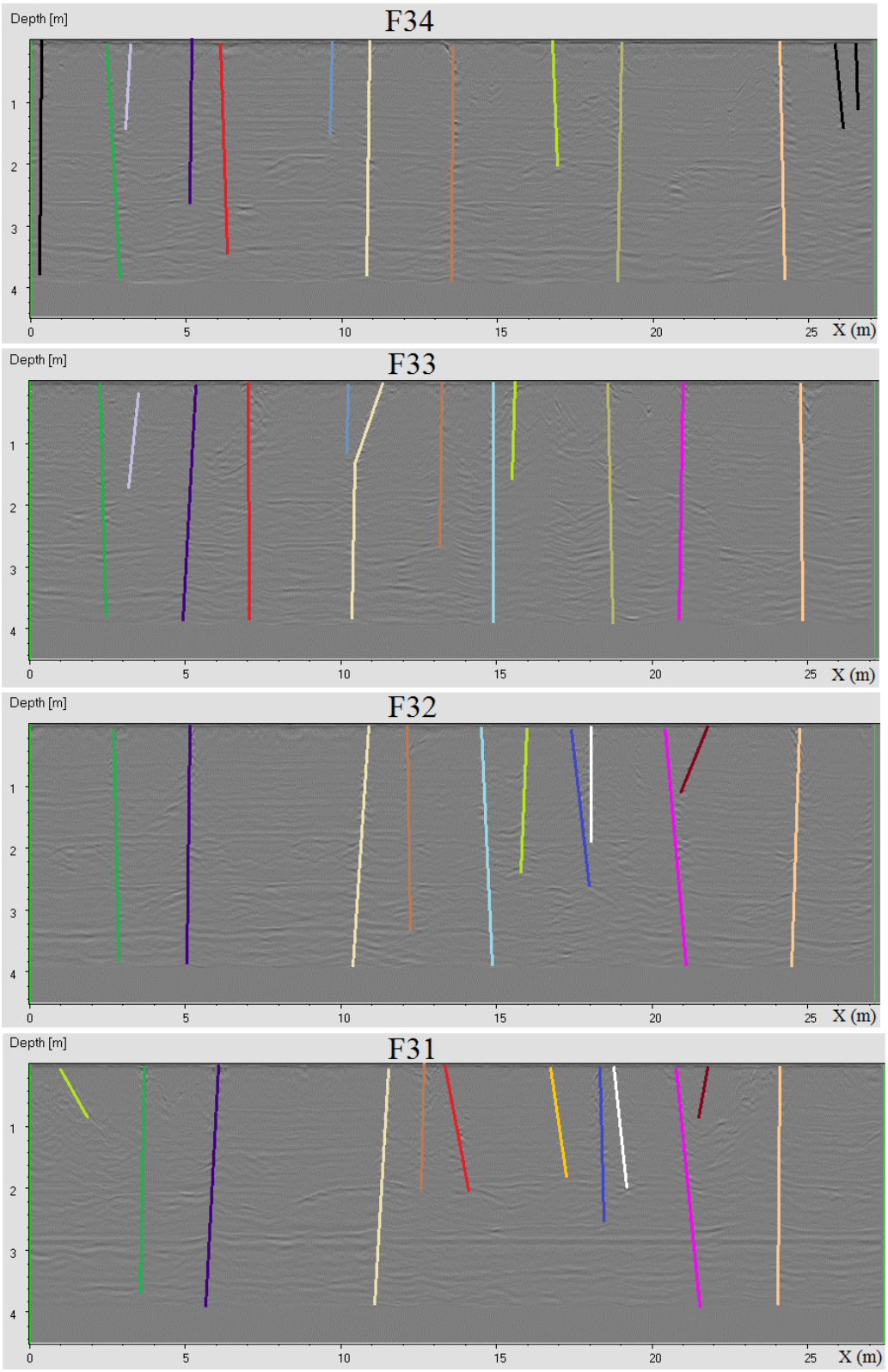

Volume 9: the interpreted radargrams F31, F32, F33, and F34.

Appendix B

The SlabCutOpt.par contains directive of the working mode, bounding domain, output options of SlabCutOpt. Keywords are briefly resumed in the given example file below.

```
#SlabCutOpt parameters file
# Block domain definition
x_max=+0.9 #
x_min=+0.0 #
y_max=+2.0 #
y_min=+0.0 #
z_max=+1.1 #
z_min=+0.0 #
#Cutting slab dimensions
dim_x=0.41 # Distance between cutting planes in the X direction
dim_y=0.21 # Distance between cutting planes in the Y direction
dim_z=0.04 # Distance between cutting planes in the Z direction
cut_saw_thickness=0.01 # Saw thickness (meter)
#Space of solutions
#angles (radiant)
theta_step=1.570796327 #
theta_max=1.570796328 #
phi_step=1.570796327 #
phi_max=1.570796328 #
psi_step=1.570796327 #
psi_max=1.570796328 #
#displacement (meters)
dx_step=0.05 #
dy_step=0.05 #
dz_step=0.05 #
#Options
read_slab_dimensions=1 #0: read only the dimensions of the single slab indicated here; 1: consider also a list of different dimensions of slabs
read_bound=0 #0: the ply file describing the faces of the block in a form of triangles
rotation_method=1 #0: Euler rotation; 1: Cartesian axis rotation
BiDimensional=0 # #0: 3D operation; 1: 2D operation
write_vtu=1 #0: no vtu file in output; #1: for each slab size within all the tested displacements, a slab.vtu file is generated; #2: only the solution of the maximum number of non-intersected slabs for each slab size
read_PLY_FileList=1 #0: Read the fracture set from “test_fractures.ply”; 1 read the PLY_FileList.dat for using several PLY files of discontinuities
end=end
```

Appendix C

The PLY file format used for SlabCutOpt is a fixed simplified version of the more general PLY file format, such as the example below. Each element must have 3 vertices (a triangle in the 3D space). The fixed characters are presented in italic font, the geometrical parameters for a fracture description are presented in bold. After the header, a number specified in [*element vertex*] indicates the coordinates of vertices, then the following [*element face*] lines define the number of vertices [*3*] and the vertices index of each triangle. It is worth mentioning that, in the more general PLY file format, the number of vertices can be higher for polygonal elements.

ply
format ascii 1.0
comment example of a fracture represented by 2 triangles
element vertex **4**
property float x
property float y
property float z
element face **2**
property list uchar int vertex_index
end_header
0.000 2.000 0.553
0.450 2.000 0.553
0.000 0.000 0.583
0.450 0.000 0.599
3 0 1 2
3 1 2 3

Appendix D

The PLY_FileList.dat input file must contain the list of the ply files of the modelled discontinuities. No header is allowed. Below is an example of PLY_FileList.dat.

```
block_fracturepink_g.ply
block_fracturepink_h.ply
block_fracturepink_k.ply
brown_frac.ply
extended_void_blue.ply
purple_frac.ply
red_frac.ply
single_void.ply
turquoise_frac.ply
yellow_frac.ply
```

Appendix E

The slab_dimensions.dat input file must contain the list of the different sizes of slabs that the algorithm must test. Below is an example of slab_dimensions.dat. The order of the columns, from left to right, is dim_x, dim_y, dim_z. The dimensions of the slabs must be increased by the cut_saw_thickness for geometrical considerations in the algorithm.

```
0.41    0.21    0.025
0.51    0.26    0.025
0.41    0.21    0.03
0.51    0.26    0.03
0.61    0.31    0.025
0.31    0.31    0.025
0.41    0.41    0.025
0.61    0.46    0.025
0.46    0.46    0.025
0.49    0.49    0.025
0.61    0.31    0.03
0.31    0.31    0.03
0.41    0.41    0.03
0.61    0.46    0.03
0.46    0.46    0.03
0.49    0.49    0.03
```

Appendix F

The results file is an ASCII file containing the results of optimization. The first part lists the dimension of tested slabs/ slab, as shown in the example below. Following this, a list of solutions for each size is given. The list consists of 12 columns, from left to right there are: the order number of iteration, dim_x, dim_y, dim_z, theta, phi, psi, total number of slabs inside the block, and number of fractured slabs.

Optimization results:

```
Number of tested dimensions of slabs: 37
[0] dim_x= 0.410000 dim_y= 0.210000 dim_z= 0.025000
[1] dim_x= 0.510000 dim_y= 0.260000 dim_z= 0.025000
..  ..  ..  .. .. .. .. .. .. .. .. ..
[n] dim_x= 0.260000 dim_y= 1.260000 dim_z= 0.040000

Results_for_slab_[0]
..  …  …  …  …  …  …  …  …  …  …  … …  …
..  …  …  …  …  …  …  …  …  …  …  … …  …
..  …  …  …  …  …  …  …  …  …  …  … …  …
Results_for_slab_[1]
..  …  …  …  …  …  …  …  …  …  …  … …  …
..  …  …  …  …  …  …  …  …  …  …  … …  …
..  …  …  …  …  …  …  …  …  …  …  … …  …
..  …  …  …  …  …  …  …  …  …  …  … …  …
764 0.510000 0.260000 0.025000 1.570796 1.570796 0.000000 -0.205000 -0.030000 -0.012500 426 121
765 0.510000 0.260000 0.025000 1.570796 1.570796 0.000000 -0.205000 0.020000 -0.012500  422  70
766 0.510000 0.260000 0.025000 1.570796 1.570796 0.000000 -0.205000 0.070000 -0.012500  422  75
767 0.510000 0.260000 0.025000 1.570796 1.570796 0.000000 -0.205000 0.120000 -0.012500  422  88
768 0.510000 0.260000 0.025000 1.570796 1.570796 0.000000 -0.155000 -0.130000 -0.012500 425 106
769 0.510000 0.260000 0.025000 1.570796 1.570796 0.000000 -0.155000 -0.080000 -0.012500 425 113
..  …  …  …  …  …  …  …  …  …  …  … …  …
..  …  …  …  …  …  …  …  …  …  …  … …  …
..  …  …  …  …  …  …  …  …  …  …  … …  …
..  …  …  …  …  …  …  …  …  …  …  … …  …
..  …  …  …  …  …  …  …  …  …  …  … …  …
 Results_for_slab_[n]
..  …  …  …  …  …  …  …  …  …  …  … …  …
..  …  …  …  …  …  …  …  …  …  …  … …  …
..  …  …  …  …  …  …  …  …  …  …  … …  …
```

Appendix G

An exhaustive description of the vtu file format can be found in the webpage of ParaView: www.paraview.com. The slab type values used for coding slabs are explained in the following table:

slab type value	description
2	intersected slabs with full size inside the block body
1	non-intersected slabs with full size inside the block body
-2	other slabs in the 3D cutting grid of slabs

Coding slab type in vtu files:

```
<?xml version="1.0"?>
<VTKFile type="UnstructuredGrid" version="0.1" byte_order="LittleEndian" compressor="vtkZLibDataCompressor">
  <UnstructuredGrid>
    <Piece NumberOfPoints="30464" NumberOfCells="3808">
      <PointData>
      </PointData>
      <CellData Scalars="myTYPES">
        <DataArray type="Float32" Name="SlabTypes" format="ascii" RangeMin="0" RangeMax="2">
        -2 -2 -2 -2
...
        </DataArray>
      </CellData>
      <Points>
        <DataArray type="Float32" Name="Points" NumberOfComponents="3" format="ascii" RangeMin="0" RangeMax="3.483490">
         -0.445000 -0.495000 -0.225000
...
</DataArray>
      </Points>
      <Cells>
        <DataArray type="Int32" Name="connectivity" format="ascii" RangeMin="0" RangeMax="30464">
         0 1 2 3 4 5
...
<DataArray type="Int32" Name="offsets" format="ascii" RangeMin="8" RangeMax="30464">
         8 16 24 32 40 48
...
```

```
      </DataArray>
      <DataArray type="UInt8" Name="types" format="ascii" RangeMin="42"
RangeMax="42">
        42 42 42 42 42 42
...
      </DataArray>
      <DataArray type="Int32" Name="faces" format="ascii" RangeMin="0"
RangeMax="30463">
        6
        4 0 3 2 1
        4 2 6 5 1
        4 4 5 6 7
        4 0 4 7 3
        4 2 3 7 6
        4 0 1 5 4
…
      </DataArray>
      <DataArray type="Int32" Name="faceoffsets" format="ascii" RangeMin="31"
RangeMax="118048">
        31 62 93 124 155 186
...
      </DataArray>
    </Cells>
  </Piece>
 </UnstructuredGrid>
</VTKFile>
```

Appendix H

An example of the input parameter file (BlockCutOpt.par) for stratum a in BlockCutOpt program.

```
#BlockCutOpt parameters file
x_max=+27.00 #
x_min=+0.0 #
y_max=+65.00 #comment
y_min=+0.0 #comment
z_max=0.8 #
z_min=0.0 #comment
psi_max=3.1416 #
psi_step=0.0523598775598299 #
dx_step=0.5 #
dy_step=0.5 #
dim_block_x=3.05 #
dim_block_y=2.05 #
dim_block_z=0.85 #
mx=1
my=1
read_bound=0 #
BiDimensional=0 #
material-lost-by-quarrying =0.05 #
read_block_dimension=1 #
write_vtu=2 #
rotation_method=1 #
read_PLY_FileList=1 #
end=end
```

Appendix I

An example of an input parameter file (BlockCutOpt.par) in BlockCutOpt program for the case study of the large scale granite quarrying area.

```
#BlockCutOpt parameters file
x_max=+31070.80449 #
x_min=+25397.77196 #
y_max=+10723.88741 #comment
y_min=+5007.604247 #comment
z_max=6.00 #
z_min=0.0 #comment
psi_max=3.1416 #
psi_step=0.0523598775598299 #
dx_step=7.0 #
dy_step=5.0 #
dim_block_x=21.025 #
dim_block_y=9.025 #
dim_block_z=6.025 #
mx=3
my=2
read_bound=0 #
BiDimensional=1 #
material-lost-by-quarrying=0.05 #
read_block_dimension=1 #
write_vtu=2 #
rotation_method=1 #
read_PLY_FileList=1 #
end=end
```